# Multiscale modeling of rubber hysteretic friction on rough rigid surfaces

Der
Fakultät Architektur, Bauingenieurwesen und Umweltwissenschaften
der Technischen Universität Carolo-Wilhelmina
zu Braunschweig

zur Erlangung des Grades eines
**Doktoringenieurs (Dr.-Ing.)**
genehmigte

**Dissertation**

von
**Ahmad, Al-Qudsi**
geboren am 29.06.1986
in Kuwait Stadt, Kuwait

2019

# Multiscale modeling of rubber hysteretic friction on rough rigid surfaces

Von der
Fakultät Architektur, Bauingenieurwesen und Umweltwissenschaften
der Technischen Universität Carolo-Wilhelmina
zu Braunschweig

zur Erlangung des Grades eines
**Doktoringenieurs (Dr.-Ing.)**
genehmigte

**Dissertation**

von
**Ahmad Al-Qudsi**
geboren am 29.06.1986
in Kuwait Stadt, Kuwait

| | |
|---|---|
| Eingereicht am: | 22 Mai 2019 |
| Disputation am: | 04 September 2019 |
| | |
| Berichterstatter: | Prof. Dr. Laura De Lorenzis<br>Prof. Dr. Michele Scaraggi |

2019

# Mehrskalige Modellierung von Gummi-Hysteresereibung auf rauen Oberflächen

Von der
Fakultät Architektur, Bauingenieurwesen und Umweltwissenschaften
der Technischen Universität Carolo-Wilhelmina
zu Braunschweig

zur Erlangung des Grades eines
**Doktoringenieurs (Dr.-Ing.)**
genehmigte

**Dissertation**

von
**Ahmad Al-Qudsi**
geboren am 29.06.1986
in Kuwait Stadt, Kuwait

Eingereicht am: 22 Mai 2019
Disputation am: 04 September 2019

Berichterstatter: Prof. Dr. Laura De Lorenzis
Prof. Dr. Michele Scaraggi

2019

# Kurzfassung

Das Verhalten von Pkw-Reifen auf Straßenoberflächen wird stark von hysteretischer Reibung beeinflusst. Um die Fahreigenschaften zu optimieren, beispielsweise zur Reduktion des Kraftstoffverbrauchs, der Verbesserung der Griffigkeit, der Erhöhung der Reifenhaltbarkeit und der Verbesserung der Kontrolle während des Lenkens und Bremsens, sollte die hysteretische Reibung richtig vorhergesagt werden.

Die genaue und effiziente Vorhersage von hysteretischer Reibung, sowohl von theoretischer wie numerischer Seite, ist eine Herausforderung. Im letzten Jahrzehnt haben zwei verschiedene Modellierungsverfahren an Aufmerksamkeit gewonnen. Sie sind: das viskoelastische Halbraummodell, das auf einer linearen Kinematik basiert und mit der Randelemente-Methode implementiert wurde, sowie das viskoelastische Kontaktmodell im Rahmen finiter Deformationen, das mit der Finite-Elemente-Methode implementiert wurde. Mit der ersten Methode können alle beteiligten Längenskalen gleichzeitig und mit reduziertem Berechnungsaufwand simuliert werden, wobei eine flache Geometrie der rauen Oberfläche und lineare Verformungen angenommen werden. Die zweite Methode hat diese Einschränkungen nicht und kann den Reibkoeffizienten genau vorhersagen, jedoch bei weitaus höherer Berechnungszeit. Hierbei können jedoch nicht alle beteiligten Längenskalen gleichzeitig untersucht werden, da ein sehr feines Netz benötigt würde, was zu inakzeptabel langen Simulationen führt.

Diese Arbeit hat zwei Hauptziele. Das erste Ziel besteht darin, die Auswirkungen geometrischer und rheologischer Linearitätsannahmen bei der Berechnung des Reibkoeffizienten zu untersuchen. Dies erfolgt durch Vergleich der Simulationsergebnisse eines Reifenprofilblocks in Kontakt mit einer sinusförmigen Oberfläche, unter Verwendung des linearen viskoelastischen Halbraummodells, das mit der Randelemente-Methode implementiert wurde, und des viskoelastischen Kontaktmodells im Rahmen finiter Deformationen und der Finite-Elemente-Methode. Betrachtet wurden Reibkoeffizient, Kontaktfläche und Druckverteilung. Es wurde festgestellt, dass mit dem viskoelastischen Halbraum Modell innerhalb der Linearitätsannahmen genaue Vorhersagen der Reibung für kleine Werte der lokaler Oberflächen-Steigung erhalten werden können, wohingegen für große Steigungen finite Deformationen berücksichtigt werden sollten.

Das zweite Ziel dieser Arbeit ist die Etablierung einer neuen, hybriden (nichtlinearer Finiten-Elemente / linearer Randelemente) -Multiskalenmethode, die die Vorteile beider Verfahren kombiniert. Die vorgestellte Hybrid-Multiskalen-Methode hat sich als geeignetes Werkzeug erwiesen, um den Reibkoeffizienten mit einem angemessenen Genauigkeitsgrad für niedrige Gleitgeschwindigkeiten zu untersuchen; Sie ermöglicht eine schnellere Berechnung des Reibkoeffizienten als das nichtlineare FE-Modell.

**Stichworte**: Kontaktmechanik, Multiskalenmethode, Gummireibung, Reifen-Fahrbahn-Kontakt, Rauigkeit.

# Abstract

The performance of car tires on road tracks is strongly affected by hysteretic friction. In order to optimize driving characteristics, like minimizing fuel consumption, improving skid resistance, increasing tire durability, and increasing vehicle controllability during steering and braking, the rolling friction coefficient should be predicted properly.

The accurate and efficient modeling and prediction of the hysteretic friction is still a challenge. In the past decade, two different modeling frameworks have attracted significant attention. They are the viscoelastic half-space (VHS)-based contact mechanics model, based on linear kinematics and implemented with the boundary element method (BEM), and the viscoelastic contact model in the finite deformation framework implemented with the finite element method (FEM). The first one has the ability to model all involved length scales at once with a reduced computational cost under the assumption of a flat geometry of the rough surface and small deformations. The second one does not have these limitations and is able to predict the friction coefficient accurately in the finite deformation framework, but at much higher computational cost. It is not able to investigate all involved length scales at once since it needs an extremely fine mesh refinement, which leads to an impractically slow simulation.

This work has two major aims. The first goal is to study the accuracy of geometrical and rheological linearity assumptions in evaluation of rolling friction coefficient. This is done by comparing the simulation results of tire tread block in contact with a sinusoidal road track surface using the linear VHS-based model and the finite deformation model in terms of rolling friction coefficient, contact area, and pressure distributions. It has been found that accurate rolling friction predictions can be obtained through the linear VHS-based model within Reynolds assumption for moderate values of root mean square slopes, whereas finite deformation computations should be adopted for large root mean square slopes. The contact area is much more sensitive to the geometrical and rheological nonlinearities than the rolling friction coefficient.

The second goal of the thesis is to establish a new hybrid (nonlinear FEM/linear BEM) multiscale method which combines the advantages of both methods. The presented hybrid multiscale approach has proven to be a suitable tool to study rolling-friction coefficient within a plausible degree of accuracy for relative large contact area and low sliding velocities. It allows a more faster calculation of friction coefficient than the finite deformation model.

**Keywords**: Contact Mechanics, Multiscale Methods, Rubber Friction, Tire Road Interaction, Roughness.

# Acknowledgements

This research was carried out during my time as research assistant from 2013 until 2017 at the Institute of Applied Mechanics (IAM) in Braunschweig University of Technology. Many people helped me during these years and without them, this thesis would never have seen the light.

First of all, I would like to express my deepest gratitude to Prof. Dr. Laura De Lorenzis, for her all unequivocal guidance, confidence and support throughout my research work for which my thanks does not suffice. I am grateful for her insightful suggestions, her time whenever I need her advice and guidance and her patience. Furhermore, I am also grateful to her for the excellent working atmosphere and freedom I have experienced during my research.

I am very grateful to have Dr. Michele Scaraggi as my second advisor and I deeply thank him for his guidance in this work and for all fruitful and inspiring discussions . His suggestions and feedbacks are gratefully appreciated.

Furthermore, I would like to address my thanks to Prof. Dr. Dieter Dinkler for acting as the external examiner of this thesis. His interest in my work is gratefully appreciated. Special thank to Prof. Dr. Manfred Krafczyk for accepting the presidency of the examination board.

I am also indebted to my colleague Dr. Roland Kruse for his assistance in solving difficulties tackled me in this project. I am appreciated to his helping hand in all stages of this research.

My sincere thanks also go to my colleague Frederik Fahrendorf for helping me to deal with supercomputing. Furthermore, I would like to thank our institute system administrator Mrs. Andrea Deutschmann and Mr. Michael Kos for backing up my data from damaged harddesk. I am very thankful to Braunschweig Pavement Engineering Centre (ISBS) for providing me asphalt specimens.

The research was financially supported by the European Research Council (ERC starting researcher grant 'INTERFACES', No. 279439). This funding is gratefully acknowledged.

I would like to acknowledge the North-German Supercomputing Alliance (HLRN) for providing high performance computing resources that have contributed to the research results reported in this dissertation.

A particular acknowledgement goes to my colleagues at Institute of Applied Mechanics for the friendly coopeation and the pleasant time that I had working with them.

Finally, my parents and my family deserve thanks from my bottom of heart for their continuous supports and encouragement.

Braunschweig, May 2019 Ahmad Al-Qudsi

# Contents

**Abstract** i

**Preface** v

**1 Introduction** 1
- 1.1 Motivation 1
- 1.2 Mechanisms of rubber friction 1
  - 1.2.1 Hysteresis 2
  - 1.2.2 Adhesion 2
  - 1.2.3 Further physical effects 3
- 1.3 State of the art 4
  - 1.3.1 Experimental investigations 4
  - 1.3.2 Linear analytical models 5
  - 1.3.3 Non-linear numerical models 8
- 1.4 Objectives of the thesis 11
- 1.5 Assumptions of the work 12
- 1.6 Outline of the thesis 12

**2 Theoretical background** 15
- 2.1 Basics of continuum mechanics 15
  - 2.1.1 Kinematics 15
  - 2.1.2 Stress measures and equilibrium equations 18
  - 2.1.3 Hyperelastic constitutive laws 21
- 2.2 Material model 22
  - 2.2.1 Rubber characteristics 22
  - 2.2.2 Isotropic hyperelastic material models 25
  - 2.2.3 Viscoelastic material models 26
  - 2.2.4 Weak form of equilibrium 30
  - 2.2.5 Linearization of the weak form of equilibrium 31
  - 2.2.6 Finite element discretization of the continuum 32
- 2.3 Basics of contact mechanics 34
  - 2.3.1 Contact kinematics 34
  - 2.3.2 Balance equations for contact 37
  - 2.3.3 Contact constraints 38
  - 2.3.4 Boundary value problem and variational form 40

- 2.3.5 Methods for enforcement of contact constraints . . . 43
- 2.3.6 Linearization and Uzawa algorithm . . . 46
- 2.3.7 Contact discretization . . . 47
- 2.4 Fourier transform . . . 49
  - 2.4.1 Fourier transform properties . . . 50
- 2.5 Hertz theory . . . 51

**3 Analysis of asphalt specimens 53**
- 3.1 Profilometry . . . 53
- 3.2 Surface roughness parameters . . . 56
- 3.3 Surface description . . . 58
  - 3.3.1 Height difference correlation function . . . 58
  - 3.3.2 Power spectral density . . . 59
  - 3.3.3 Superposition of sinusoidal functions . . . 61
- 3.4 Surface approximation . . . 63

**4 The influence of geometrical and rheological non-linearity on the calculation of rubber friction 67**
- 4.1 Introduction . . . 67
- 4.2 Linear viscoelastic model . . . 68
  - 4.2.1 VHS-based formulation . . . 68
  - 4.2.2 Numerical scheme . . . 71
  - 4.2.3 Model validation against existing results . . . 72
- 4.3 Finite deformation model . . . 77
  - 4.3.1 Problem statement . . . 77
  - 4.3.2 Boundary conditions . . . 78
  - 4.3.3 Material model . . . 80
  - 4.3.4 Implementaion in ABAQUS . . . 80
  - 4.3.5 Time averaging . . . 81
- 4.4 Comparison between approaches . . . 82
  - 4.4.1 Influence of geometrical non-linearity on calculation of the friction coefficient . . . 83
  - 4.4.2 Influence of geometrical non-linearity on calculation of contact area . . . 83
  - 4.4.3 Influence of geometrical non-linearity on estimation of contact pressure and separation fields . . . 87
- 4.5 Conclusions . . . 87

**5 Hybrid multiscale approach to rubber friction 93**
- 5.1 Principle of the hybrid multiscale approach . . . 93
- 5.2 Sensitivity to the number of superimposed sinusoidal waves . . . 96
- 5.3 Results of the hybrid multiscale approach . . . 101
  - 5.3.1 Results on microscale . . . 101
  - 5.3.2 Macroscopic results . . . 102
- 5.4 Numerical verification of the hybrid multiscale approach . . . 107

5.5 Conclusions . . . . . . . . . . . . . . . . . . . . . . . . . . . . . . . . 110

**6 Summary and outlook 111**

6.1 Summary and conclusions . . . . . . . . . . . . . . . . . . . . . . . 111

6.2 Future work . . . . . . . . . . . . . . . . . . . . . . . . . . . . . . . . 113

**A Averaging tables 115**

**Bibliography 123**

# Chapter 1

# Introduction

## 1.1 Motivation

Frictional contact of rubber-like materials with rough surfaces appears in various technological applications, including car tires on road tracks, seals, wiper blades, conveyer belts, and seismic isolators. In some applications, like seals and wiper blades, the frictional contact occurs with smooth surfaces on a macroscopic length scale, whereas car tires get into contact with asphalt surfaces that have rough character over different length scales.

A major application of the study of rubber friction is for car tires on road tracks. The frictional interaction between tire and pavement surface has an important influence on the tire performance. It also plays a major role on the durability and the safety of the tires and the controllability of the vehicle during maneuvers like steering, braking, and accelerating. Recent studies [54] show a strong relationship between rolling friction and fuel consumption.

The grip behavior of tires depends also on multiple physical phenomena inside rubber. In order to improve the braking performance and to reduce the braking distance, a deeper understanding of the rubber friction process at braking velocities is important. This will help to reduce the number of traffic fatalities. Therefore, an accurate prediction of the tire-road friction coefficient is crucial for a better understanding of tire behavior in design and simulation.

## 1.2 Mechanisms of rubber friction

Rubber friction is an intricate phenomenon that has not been totally understood. There are several mechanisms occurring during rubber friction, see Figure 1.1. These mechanisms include hysteresis [40, 68], adhesion [24, 76, 91, 96], wear [71], flash temperature effects [70, 75], and rain water films [90]. All this makes it complicated to capture the total friction coefficient experimentally as well as to predict it theoretically.

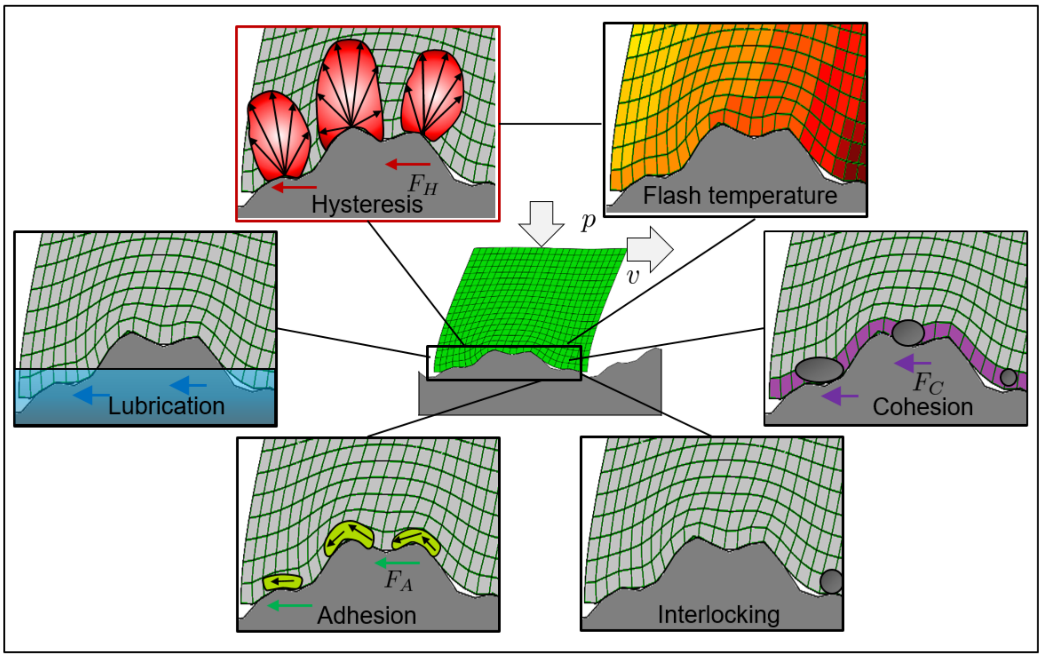

**Figure 1.1:** Mechanisms of rubber friction.

### 1.2.1 Hysteresis

For low sliding velocities ranging from [mm/s] to [cm/s], the main contribution to rubber friction on rough surfaces is the hysteresis loss. Hysteresis is a phenomenon that originates from the excitation of the viscoelastic rubber by the pulsating cyclic forces resulting from the cyclic loading and unloading and the varying surface asperities, that in turn causes a viscoelastic energy dissipation in the bulk of the material. Hysteresis was observed first by Schallamach [94] and then confirmed and explained by Grosch [26] in his pioneering experiments. They found that hysteresis is strongly related to the velocity since the rubber material is excited with different frequencies for different sliding velocities.

For high sliding velocities larger than 100 [mm/s], the dissipated energy is transferred into heat which will rise up the rubber temperature during the sliding. Since the viscoelastic rubber properties are temperature-dependent, the temperature rise leads to significant changes in the viscoelastic properties of the elastomer, which in turn influence the frictional response. This effect is called flash temperature effect and it is related directly to the hysteresis at sliding velocities higher than 100 [mm/s]. Flash temperature effect is the most important contribution for high velocities.

### 1.2.2 Adhesion

The second most important contribution to rubber friction is adhesion. Adhesive friction is a surface phenomenon induced by intermolecular forces and bonding/debonding mechanisms acting in the contact layer between rubber material and the road surface on a nanometer length scale. It can be combined with hysteresis simulation by the estimation of the relative contact area and introduction of a macroscopic shear stress law [24, 76, 91, 96].

There exist different explanations for the origin of adhesion like van-der-Waals dispersive forces or the interaction between rubber atoms and rough surface molecules.

While adhesion has a considerable effect in dry friction, its influence reduces in wet friction. This is due to the fact that adhesion is activated on dry surfaces and suppressed on rough surfaces covered with a water film.

Each of these mechanisms is related to a particular length scale. Hysteresis is dominated by length scales of few micrometers, while the adhesion is related to smaller length scales of a few hundred nanometers.

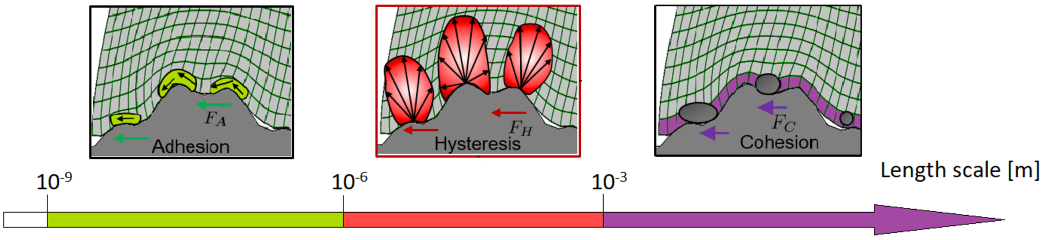

**Figure 1.2:** Rubber friction mechanisms influence regions on different length scales.

## 1.2.3 Further physical effects

### Wear (Cohesion)

Wear occurs when the rubber material interacts with sharp asperities of the rough road substrate. When the sliding velocity increases, the local stress at the contact point between the rubber and road surface also increases near to sharp asperities. This high stress at the contact point reduces the linkage between the rubber molecules and causes some rubber material to be detached. The worn surface may influence adhesion [52]. Wear is described on length scales of several millimeters.

### Wet friction (Lubrication and viscous forces)

In wet friction, small road cavities are filled with water, limit the generation of contact pressures that do not contribute anymore to hysteretic friction. For high sliding velocities, the viscosity behavior of water requires high shearing forces to be drained out of the contact area. This gives an additional contribution caused by shearing of the waterfilm, whose amplitude depends on the viscosity of the fluid and the nature of contact.

### Interlocking

Interlocking effects take place when the rubber block hits with its edges asperities of the rough road track causing a horizontal resistance force. This effect is especially expected at the leading edge of the rubber block and increases with surface roughness.

### Other phenomena

Apart from all aforementioned mechanisms there are also minor effects like contamination, and tribocharging [77].

Figure 1.3 shows the share of each mechanism to the overall friction coefficient.

**Figure 1.3:** Contribution of different mechanisms to the total friction coefficient for low sliding velocities ranging from mm/s to cm/s [112].

It should be noted that only for high sliding velocities, viscous forces (lubrication), wear (cohesion) and temperature effects play a major role. They are negligible for low macroscopic velocities [114]. They are out of scope of the present work and will be left for future investigations.

## 1.3 State of the art

A lot of experimental and modelling studies were performed in order to understand the process of rubber friction. They are summarized as follows.

### 1.3.1 Experimental investigations

The early experiments of Schallamach [93, 94] observe that rubber friction depends strongly on the applied macroscopic pressure, velocity, and temperature. His first experiment [93] reveals pressure dependency of rubber friction coefficient. In the other experiment [94], a non-linear velocity and temperature dependency of rubber friction is reported. Grosch [26, 27] found within his experiments that there exists a strong connection between the loss modulus and the frictional behavior of rubber material. He also found that the velocity dependency of the frictional behavior can be linked and correlated to the viscoelastic material properties of elastomers.

Starting from the friction test results reported by Schallamach [93, 94] and Grosch [26, 27], several experiments with increased complexity were developed over decades. Friction experiments are often performed on test rigs with a linear motion of the rubber block or the counter surface. Some details of the linear friction test rigs can be found in [32, 33, 37]. A test rig named High-Speed Linear Test Rig (HiLiTe) is developed at the Institute of Dynamics and Vibrations Research (IDS) in Hanover. It has an operating range for pressures between 0.1 and 0.5 [MPa] and a velocity range from 0.1 to 3 [m/s]. Further descriptions and developments of HiLiTe can be found in [83, 115]. Rotational test rigs [22] are used for wear studies since larger sliding distances can be captured with such setups. Important quantities like the temperature of the rubber specimen and the temperature of the road track can be measured using modern test rigs, see [42, 46, 47]. Zeng [126] reports a large review of experimental investigations of rubber friction.

However, experimental rigs often have limitations concerning the applied pressure or the sliding velocity. Some data can hardly be gathered in experiments, like local pressures, dissipated energies, or contact area. The rerun of experiments often takes place under different boundary conditions. Material properties of rubber are sensitive to outdoor environmental conditions like ambient temperature, air humidity and road environment. Furthermore, the prior history of the tire could produce local heating and leads to a pronounced effect on rubber friction [115]. Sometimes, rubber may suffer from micro cracks. Moreover, the surface characteristics could be changed because of dust and lubrication. It is also difficult to separate the various effects that influence the frictional behavior. Recently, Wagner [114] reported that one can ensure a constant ambient temperature by placing the test setup in a climate box.

### 1.3.2 Linear analytical models

There are two well known analytical theories for the mechanics of rubber friction to fractal surfaces. The first is the one proposed by Heinrich and Klüppel [40]. The other one is Persson's theory [68].

#### Heinrich and Klüppel's theory

In their model, the hysteretic component of the macroscopic friction coefficient is calculated by assuming a uniaxial viscoelastic element sliding over a rough surface and then estimating the resulting energy dissipation. The energy dissipation inside the rubber volume $V_r$ during a certain time $\Delta t$ can be calculated by the product of stress $\boldsymbol{\sigma}$ and the time derivative of strain $\dot{\boldsymbol{\varepsilon}}$:

$$\Delta E_{diss} = \int\limits_{0}^{\Delta t} \int\limits_{0}^{V_r} \boldsymbol{\sigma} : \dot{\boldsymbol{\varepsilon}} \, dV \; dt. \tag{1.3.1}$$

The dissipated energy during the sliding interval $T$ has to be equal to the product of the hysteretic friction force $F_H$ and the applied velocity $v$.

$$\frac{\Delta E_{diss}}{T} = F_H \cdot v \tag{1.3.2}$$

The roughness profile is taken as a self-affine track that is described by its height difference correlation function in the form of a power law.

$$C_{HDC}\left(\lambda\right) = \xi_{\perp}^{2} \left(\frac{\lambda}{\xi_{\parallel}}\right)^{2H} \quad , \quad \lambda \leq \xi_{\parallel} \tag{1.3.3}$$

$$C_{HDC}\left(\lambda\right) = \xi_{\perp}^{2} \qquad\qquad , \quad \lambda > \xi_{\parallel} \tag{1.3.4}$$

$H$ is Hurst exponent, which is a measure of surface irregularity, $\lambda$ is the horizontal length scale. The cutoff point is defined by the values $\xi_{\perp}^{2}$ and $\xi_{\parallel}$. It should be noted that the power spectral density (PSD) function and the height difference correlation (HDC) function can be both used to describe the characteristics of a self-affine rough surface and can be transformed to each other. For further explanation to height difference correlation function, power spectral density, and self-affine tracks, the reader is directed to Section 3.3 in Chapter 3.

The uniaxial element is characterized by a small deformation viscoelastic model such as the Kelvin-Voigt, Maxwell, or Zener model, through the corresponding expressions of the storage and loss moduli of the rubber. The model assumes that the surface asperities on all length scales are completely filled by the rubber, which only holds for sufficiently large normal pressures. This restriction is expressed by introducing a mean penetration depth of the rubber $\langle z_p \rangle$, which is determined from an extension of the well-known Greenwood and Williamson theory [25] for self-affine surfaces.

Heinrich and Klüppel [40] derived an equation that calculates the hysterestic friction coefficient by using equation (1.3.2) and integrating over all excitation wavelengths as follows

$$\mu_H = \frac{1}{2(2\pi)^2} \frac{\langle z_p \rangle}{pv} \int E''\left(\omega\right) \;\cdot\; S\left(\omega\right) \omega \, d\omega \, , \tag{1.3.5}$$

where $p$ is the applied macroscopic pressure and $\omega$ is the excitation frequency. $S\left(\omega\right)$ is a frequency-dependent description of the power spectral density based on the quantities $\left(\xi_{\parallel}, \xi_{\perp}^{2}, H\right)$ of the height difference correlation function. $E''\left(\omega\right)$ is the loss modulus, see Chapter 2.

In a later publication of Klüppel and Le Gal [44], the model was slightly modified by taking into account the ratio of the thickness of the excited layer to the mean penetration depth as a calibration parameter. Le Gal [44] further developed this model by decomposing the height difference correlation function into two distinct scaling regions. The first region represents the largest length scales while the second one expresses the smallest ones.

### Persson's theory

Another important analytical theory is Persson's theory [68], which differs from Heinrich and Klüppel's theory in two aspects: it is fully three-dimensional, and it takes into consideration to what extent the rubber follows the profile of the rigid substrate at each length scale.

Persson's theory assumes two contacting surfaces squeezed together by nominal pressure $p_0$ so that the probability density function of the interfacial pressure is expressed as a Dirac delta function centered at $p_0$. The pressure distribution corresponds as a Gaussian distribution. Therefore, a relation between the statistical properties of the height distribution and the interfacial pressure distribution can be established. The relation states that the variance of the contact pressure is proportional to the variance of the surface gradient and squared effective elastic modulus. Based on these considerations, a diffusion-type equation was formulated for the contact pressure distribution. Persson [68] introduced a boundary condition stating that the probability density function of the contact pressures vanishes at zero pressure. Persson's theory predicts that the contact area evolves as an error function, from zero to full contact, which is reached for infinite nominal pressure.

In contrast to theory of Heinrich and Klüppel [40], Persson [68] uses a function $P(\mathbf{q})$ that describes the interaction between the rubber block and the road track. The formulation of friction coefficient reads [68]

$$\mu_H = \frac{1}{2} \int_{q_{\min}}^{q_{\max}} C_{PSD}(q)\, S(q)\; P(q)\; q^3\, dq \int_0^{2\pi} \cos(\phi)\, \frac{E^*(qv\cos(\phi))}{(1-\nu^2)\, p}\, d\phi. \tag{1.3.6}$$

where $q$ is the magnitude of the wave vector, $S(q)$ is a reduction factor, $E^*$ is the complex viscoelastic rubber modulus, $\nu$ is the Poisson ratio, $\phi$ is the surface angle, and $C_{PSD}(q)$ is the power spectral density that describes the rough surface. It is introduced by Persson [76] as:

$$C_{PSD}(q) = \frac{1}{(2\pi)^2} \int \langle z(\mathrm{x})\, z(0) \rangle\, e^{-i\mathrm{q}\cdot\mathrm{x}} d\mathrm{x}, \tag{1.3.7}$$

where $z(0)$ is the mean height of the profile.

Persson's theory is more accurate than Heinrich and Klüppel's model since it takes into account to what extent the rubber follows the profile of the rigid substrate at each length scale. This is done via the function $P\left(\mathrm{q}\right)$ instead of introduction of $\langle z_p \rangle$, which serves the same purpose but in an average way [17]. Another advantage of Persson's approach is that it can incorporate any small deformation viscoelastic model by defining storage and loss moduli of the rubber material.

Despite of very fast computation times, these analytical approaches have limitations since they are utilized within the framework of linear viscoelasticity with infinitesimal deformations [11, 13, 14, 68, 72, 88, 91]. The analytical models also have restrictions related to geometrical effects (Reynolds roughness assumption), i.e. they assume that the roughness square slope is less than one. The aforementioned assumptions allow for the use of the viscoelastic half-space (VHS) theory [38] in modeling the deformation response of generic contacting surfaces. The VHS method can be applied to multiscale [68] as well as multi-asperity [40, 44] viscoelastic contact theories and in boundary element numerical formulations. On the other hand, kinematically non-linear continuum mechanics formulations, implemented numerically through finite element approaches, do not have these limitations and are able to provide predictions of rubber friction in a finite deformation framework, but at much higher computational cost.

### 1.3.3 Non-linear numerical models

The road track is rough on many different length scales and each of these scales influences the hysteretic friction by excitation of material damping modes. The micro asperities contribute considerably to the overall macroscopic response of the system [68, 78]. Moreover, the friction process includes finite deformations and large strains on different scales. Since each friction mechanism is dominant at different length scales and each of the scales gives its own contribution to the friction coefficient, a multiscale approach is required in order to capture all surface details down to a certain cutoff size. On the other hand, an explicit modeling of the surface roughness with all asperities details using finite elements would be numerically expensive because of the wide spectrum of length scales ranging from millimeters to micrometers. For this reason multiscale methods are used to reduce the computational cost.

There are several categories of numerical multiscale approaches of rubber friction. They are summarized as follows.

#### Multiscale projection method

This approach was proposed by Nitsche [59]. Nitsche computes the frictional behavior of a rubber block with a coupling between the scales. A frictionless contact is assumed on all scales and the coupling is carried out by transferring displacement and traction boundary conditions from one scale to the following. For each macroscopic contact point, a micro calculation is done by applying the current macroscopic displacement on the micro scale as a boundary condition. In the following step, the microscopic contact forces and stresses are projected back to the macroscopic contact boundary. This procedure is repeated until a defined convergence criterion is reached. This approach has an advantage that no information is lost since all quantities are transferred between the scales. However, there are two main drawbacks of this method: the first is its complicated data structure, and the second is the instabilities resulting from the projection which affects the convergence rate for the macroscopic simulation. Another criticism is that implementation of viscoelastic effects, which is a basic element for studying the rubber friction, was not done by Nitsche [59].

### Multiscale contact homogenization techniques

Temizer and Wriggers [103] developed a contact homogenization technique to calculate the macroscopic friction coefficient of granular interfaces, i.e. interfaces between an elastic solid and a rigid surface with rigid particles embbeded as third bodies. The scales are splitted into a macroscopic scale without microscopic details and a microscopic scale including the micro particles. The macroscopic contact pressure and the local velocity are inserted as spatially constant boundary conditions on the microscopic scale.

In order to allow for an application of this approach the macroscopic length scale $L$ must be significantly larger than the microscopic length scale $l$, i.e. $L \gg l$. Otherwise, the assumed constant boundary conditions would become inadequate. A periodic representative microscopic setup is constructed since the microscopic structure has repetitive properties. Thus, the microscopic simulation setup is often called representative volume element or representative contact element (RVE/RCE). The resulting total reaction forces on top of the rubber block in horizontal and vertical directions are calculated. The resulting friction coefficient is averaged over time in a homogenization step.

$$\mu\left(t\right)=\frac{\left|F_x\left(t\right)\right|}{\left|F_z\left(t\right)\right|}, \qquad \mu_{avg}=\frac{1}{t_1-t_0}\int\limits_{t_0}^{t_1}\mu\left(t\right)\,dt. \tag{1.3.8}$$

The resulting friction coefficient is incorporated in the macroscopic scale, hence enhancing the contact calculation with the microscopic result. This procedure is repeated in each contact integration point with different microscopic velocity and pressure input data for every time step. This results in a large computation time, which makes the approach quite expensive from a computational point of view. Another criticism to this approach is that only two scales are taken into account. The approach was further extended to include the viscoelastic effects by Temizer and Wriggers [104]. Extensions to thermal interactions can be found in [105, 106, 107, 108].

Starting from the contact homogenization approach suggested by Temizer and Wriggers [103], a new multiscale approach for viscoelastic rubber friction on a rough rigid surface was proposed by Wriggers and Reinelt [118]. They approximated the rough fractal surface by superposition of a finite number of sinusoidal waves. This was done based on an approximation of the rough surface HDC function (see Section 3.3) by a sum of single HDC functions of each scale. At the smallest length scale, a frictionless behavior is assumed. A computation on each scale, where a finite deformation viscoelastic model describes the rubber material, leads through homogenization to a friction law that is locally applied to the next larger scale. The procedure is recursively applied until the largest significant scale is reached. The results obtained with a three-scale or four-scale approximation of the rough surface are compared. They found that adding a very small length scale gives a large difference for the resulting friction coefficient. The main criticism to this approach is that it does not take into account the role of the smallest-scale roughness, which has a signficant role on the friction coefficient [86]. Another criticism is that this approach uses node to sigment contact elements which are less stable for large deformations in the contact zone and result in less accurately calculated contact pressure values. The derived friction law is very sensitive to the selected pressures and velocities. Another disadvantage of this approach is that it is restricted to a limited number of sine waves, which gives a poor approximation of the measured surface, which in turn influences the simulation results. Another drawback is that it is computationally expensive to homogenize the friction coefficient. Also, this multiscale approach assumes a constant pressure on each scale. This is obviously incorrect due to the viscoelastic material behavior.

A multiscale approach was recently suggested by Wagner and Wriggers [113]. They take into account the PSD function of the measured rough surface. Then, the rough surface is reconstructed by a sum over a large number of sinusoidal functions N

$$\mathrm{z}\left(\mathrm{x}\right)=\sum_{\mathrm{i}=1}^{\mathrm{N}}2\sqrt{\frac{2\pi}{\mathrm{L}_0}\mathrm{C}_{\mathrm{PSD}}\left(\mathrm{q}_\mathrm{i}\right)}\sin\left(\mathrm{q}_\mathrm{i}\mathrm{x}+\phi_\mathrm{i}\right) \tag{1.3.9}$$

with a random shift phase $\phi_i$ and the largest wavelength $L_0$. Wagner [113] used the derived equation in [76] to reconstruct a real rough road surface. Then, the reconstructed surface can be split into macroscopic and microscopic parts by dividing the introduced sum at a certain split frequency.

A mortar discretization method was used to ensure a robust and stable contact simulation in a large pressure range. A micro friction law was derived from homogenized micro calculations with different pressures and velocities. At the following step, the values are fitted with splines to extract a continuous micro friction law for a certain pressure and velocity range.

It has been demonstrated that the results of a whole surface calculation can be reproduced with the multiscale method by the comparison between the calculations of the superimposed full surface with the calculations of the split-homogenized scales. However, a quantitative gap was observed. The chosen cut-off frequencies might be one source for the observed gap. Another point could be the senstivity of the friction law to the selected values used in homogenization. The main issue of Wagner's approach is the lack of clear criteria for the selection of macroscopic, microscopic and splitting frequencies.

An important factor that affects the results of homogenization procedures is the appropriate selection of parameters like microscopic block size, boundary conditions or block discretization.

Temizer and Wriggers [103] investigated the influence of microscopic block height, block width, and the number of the involved particles since these quantities represent free parameters. In another study [104], they investigated the difference between displacement boundary conditions and traction boundary conditions applied on the microscopic block.

A comprehensive study was done by De Lorenzis and Wriggers [17] on several parameters that influence the homogenization results including block height, block discretization, dragging distance, applied pressures and velocities, and the compression time. They identify the compression time for applying the pressure on top of a microscopic RCE as an important parameter, since it influences the oscillations of the resulting friction coefficient. They justified the importance of the compression time that the contact area is adjusted in the compression phase and a large difference to the stationary contact area during the dragging phase leads to large oscillations. Therefore, the compression time must be adopted for different velocities such that the contact area of the compression phase is close to the contact area of the dragging phase. They found that the height of the oscillations depends on several parameters, such as the total time duration of compression phase, the height of the specimen, the applied pressure and the dragging velocity. They conclude that a ratio of height to width of the RCE of 0.75 is sufficient to incorporate the mostly stressed material region, so that the ensuing macroscopic friction coefficient considers the whole amount of energy dissipation taking place at the micro-level. They also found that finer mesh resolution leads to a notable decrease in the size of the micro-oscillations and thus to a better iterative convergence behavior. Another conclusion states that a dragging distance of 12 times the width of the RCE is satisfactory to ensure that the steady-state conditions are matched during the dragging phase. These conclusions will be used later in Section 4.3 in Chapter 4.

## 1.4 Objectives of the thesis

There are two major goals of this thesis. The first goal is to investigate the role of geometric linearity (small square slope roughness, linear kinematics) and viscoelasticity description on the resulting friction coefficient and contact area formation. To this aim, predictions of a novel VHS-based contact mechanics model, based on linear kinematics and implemented with boundary element method (BEM) in the Fourier space, are compared with those of a formulation of the viscoelastic contact problem in the finite deformation framework implemented with the finite element method (FEM). In both models, a realistic rubber rheology, involving multiple relaxation times, is adopted in order to accurately describe the rubber relaxation process. The comparison allows us to shed light on the accuracy of the widely used assumption of geometric and rheological linearity in the evaluation of rubber friction and contact area, see Chapter 4.

The second goal of this thesis is to establish a new hybrid multiscale approach that combines both the kinematically linear and the kinematically non-linear models to derive the macroscopic friction coefficient. The reason for this combination is that the kinematically linear model implemented with the BEM is very fast, whereas the kinematically non-linear model implemented using the FEM is more accurate. For this purpose, the roughness will be decomposed into a finite number of scales. The scales that have large root mean square slopes (sharp asperities) are correlated using the difference between the kinematically linear model and the nonlinear model. The suggested approach allows to speed up the multiscale approach and to reduce the computational cost of FEM simulations while still maintaining a good degree of accuracy, see Chapter 5.

## 1.5 Assumptions of the work

The rubber components always undergo large deformations whereas the track profiles remain nearly undeformed. Therefore, the assumption of rubber contact to a rigid surface is acceptable in this work [17].

The effects of temperature, wear, and lubrication are visible only for large sliding velocities higher than 100 [mm/s] and are negligible for low macroscopic velocities [114]. Therefore, the established multiscale approach will consider only hysteresis as the main effect contributing to the overall friction force. The adhesion can be estimated by introducing a macroscopic shear law coupled to the hysteretic part by evaluation of contact area and will be left for future work. Thus, the multiscale approach is limited for low macroscopic sliding velocities less than 100 [mm/s]. Other sources of rubber friction will be left for future work.

In summary, this study will focus on dry friction with a quasi-static isothermal sliding contact of a rough rigid surface composed of a finite number of sinusoidal functions.

## 1.6 Outline of the thesis

Chapter 2 gives an introduction to continuum mechanics fundamentals and the basic equations for the solution of contact mechanics problems. Fourier transform is also discussed in this chapter. The major goal of this chapter is to build up a uniform notation and to establish a basis for the following chapters.

In Chapter 3, a realistic road track is measured using profilometry. A brief introduction about profilometry is given. An overview of fractal nature of road tracks and their approximation is presented also in this chapter.

Chapter 4 investigates the influence of geometrical and material non-linearities on the calculation of rubber friction. This chapter consists of three parts. In the first part of this chapter, a linear viscoelastic halfspace-based contact model is formulated and implemented using BEM. The second part of this chapter deals with the essential features of the finite deformation model implemented with the FEM. This includes the material model, the testing phases, the boundary conditions, the computational contact treatment and the time averaging. The last section of this chapter compares and discusses the results from both kinematically linear small deformations BEM and non-linear finite deformations FEM approaches in terms of friction coefficient and contact area.

In Chapter 5, a novel hybrid multiscale approach is established. Implementation details are provided and certain important aspects are examined with numerical studies. The results of the hybrid multiscale method are validated numerically with the results of the full non-linear FEM results at the end of this chapter.

The main results and conclusions are summarized briefly in Chapter 6. An outlook is given on how to improve the proposed approach in further work.

# Chapter 2

# Theoretical background

This chapter provides a brief summary of continuum mechanics, contact mechanics, finite element (FE) discretization and Fourier transform. The major goal of this chapter is to build up a basis for the following chapters and to establish a uniform notation. The first section gives a short introduction to basics of continuum mechanics since they are important to understand the used material model, which is also introduced in this chapter. The second section deals with the basic equations of contact mechanics concerning normal and tangential contact of a deformable body on a rigid surface. The last section explains the principle of Fourier transform, which will be used later in Chapter 4.

## 2.1 Basics of continuum mechanics

Continuum mechanics is a branch of mechanics that deals with the analysis of kinematics, equilibrium and the mechanical behavior of materials modeled as a continuous mass rather than as discrete particles. Detailed information concerning the treatment of continuum mechanics can be found, for example, in the books by Holzapfel [34], Belytschko [6], Bonet and Wood [9], Wriggers [119], Altenbach [3], Chadwick [15], Ogden [60], and Truesdell [110].

### 2.1.1 Kinematics

This subsection deals with the geometric relations, motion and strains of a single body. Since large deformations are treated in this dissertation, a differentiation between reference and current configurations is essential.

In general, all indices and quantities for components of tensors and vectors in the current configuration are denoted by small letters, while terms referring to the reference configuration will be written in capital letters. Furthermore, the gradient and the divergence operators are denoted as

$$\begin{aligned} \operatorname{Grad}(\cdot) &= \nabla_{,\boldsymbol{X}}(\cdot) = \frac{\partial(\cdot)}{\partial \boldsymbol{X}}\,, \quad \operatorname{Div}(\cdot) = \operatorname{Grad}\cdot(\cdot) \\ \operatorname{grad}(\cdot) &= \nabla_{,\mathbf{x}}(\cdot) = \frac{\partial(\cdot)}{\partial \mathbf{x}}\,, \quad \operatorname{div}(\cdot) = \operatorname{grad}\cdot(\cdot)\ . \end{aligned}$$

Any deformation or motion of a body can be mathematically written as a mapping $\boldsymbol{\varphi}$ between reference and deformed configurations as

$$\mathbf{x} = \boldsymbol{\varphi}(\boldsymbol{X}, t)\,, \tag{2.1.1}$$

Figure 2.1 illustrates a material body in its undeformed and deformed states, where $\mathbf{X} = X_I\ \mathbf{E}_I$ is the position of a point in the initial configuration $\Omega_0$ at the initial time $t_0$, while $\mathbf{x} = x_i\ \mathbf{e}_i$ is the location of the same point in the deformed configuration $\Omega$ at time t. Here $\mathbf{E}_{I=1,2,3}$ and $\mathbf{e}_{i=1,2,3}$ are the global cartesian unit vectors in the reference and the current configuration, respectively. They are denoted using the Einstein summation convention for both configurations. $d\boldsymbol{X}$ is a differential line element of a material line emanating from position $\boldsymbol{X}$ in the reference configuration that transforms under the deformation to the differential line element $d\mathbf{x}$ of the same material line at a point $\mathbf{x}$ in the current configuration.

The boundary in the reference configuration $\Gamma$ consists of three parts: $\Gamma_t$ with imposed surface tractions, $\Gamma_u$ with prescribed displacements and $\Gamma_c$ where the contact potentially occurs. Their counterparts in the current configuration are, respectively, $\gamma_t$, $\gamma_u$ and $\gamma_c$.

When the motion (or any field value) is described in terms of material coordinates $\mathbf{X}$, this is called Lagrangian description. It is also referred to as material or referential description. Conversely, in the Eulerian or spatial description, the motion (or any field value) is characterized in terms of spatial coordinate $\mathbf{x}$. The Lagrangian description describes the motion of a fixed material point through the space, whereas the Eulerian description considers a fixed spatial point and observes the movement of the material through this point.

Taking the differential of (2.1.1), one obtains the following equation:

$$d\mathbf{x} = \boldsymbol{F}\ d\boldsymbol{X}\ , \quad d\boldsymbol{X} = \boldsymbol{F}^{-1}\ d\mathbf{x}\,, \quad \boldsymbol{F} = \frac{\partial \boldsymbol{\varphi}(\boldsymbol{X}, t)}{\partial \boldsymbol{X}} = \frac{\partial \mathbf{x}(\boldsymbol{X}, t)}{\partial \boldsymbol{X}}\,, \tag{2.1.2}$$

where $\boldsymbol{F}$ is the deformation gradient, a second order tensor which maps elements in the reference configuration into elements in the current configuration.

The displacement vector $\boldsymbol{u} = [u_1\ u_2\ u_3]^{\mathrm{T}}$ at a point with the coordinate $\boldsymbol{X}$ is defined as the difference between its deformed and undeformed positions.

$$\boldsymbol{u}(\boldsymbol{X}, t) = \boldsymbol{\varphi}(\boldsymbol{X}, t) - \boldsymbol{X} = \mathbf{x}(\boldsymbol{X}, t) - \boldsymbol{X}\ . \tag{2.1.3}$$

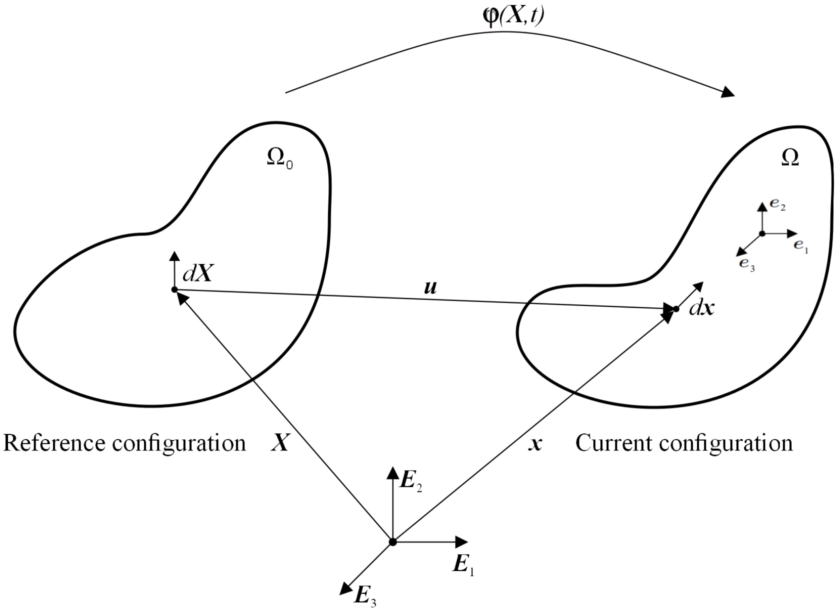

**Figure 2.1:** Schematic representation of configuration and motion of the material body.

From eqs. (2.1.2) and (2.1.3), the deformation gradient $\boldsymbol{F}$ can be expressed as

$$\boldsymbol{F} = \frac{\partial \boldsymbol{u}}{\partial \boldsymbol{X}} + \mathbf{I}\,, \tag{2.1.4}$$

Thus, the deformation gradient consists of two terms, the first term is defined as the displacement gradient Grad $\boldsymbol{u}$ with respect to the undeformed position, while the second term $\mathbf{I}$ is the second-order unit tensor, whose components are given by the Kronecker delta $\delta_{IJ}$,

$$\mathrm{I}_{IJ} = \delta_{IJ} = \begin{cases} 1 & I = J \\ 0 & I \neq J\,. \end{cases}$$

The relationship between the deformed $(dv)$ and undeformed $(dV)$ volume elements can be obtained as

$$dv = J\;dV\,, \quad J = \det\left(\boldsymbol{F}\right)\,, \tag{2.1.5}$$

in which $J$ is the Jacobian or determinant of the deformation gradient.

Nanson's formula is an important relation that can be used to transform areas in the current configuration into areas in the reference configuration and vice versa. This formula states that

$$\boldsymbol{n}\,da = J\boldsymbol{F}^{-\mathrm{T}}\boldsymbol{N}dA\,, \tag{2.1.6}$$

where $da$ is the area of an infinitesimal region in the current configuration, $dA$ is the same area in the reference configuration, and $\boldsymbol{n}$ is the outward normal to the area element in the current configuration while $\boldsymbol{N}$ is the outward normal in the reference configuration.

The deformation induced strains inside the body can be described using the squares of the lengths of the differential elements $d\mathbf{x}$ and $d\boldsymbol{X}$

$$
\begin{aligned}
|d\mathbf{x}|^2 &= d\boldsymbol{X} \cdot \boldsymbol{C}\, d\boldsymbol{X}\,, \\
|d\boldsymbol{X}|^2 &= d\mathbf{x} \cdot \boldsymbol{b}^{-1}\, d\mathbf{x}\,,
\end{aligned}
$$

where $\boldsymbol{C}$ is the right Cauchy-Green deformation tensor and $\boldsymbol{b}$ is the left Cauchy-Green deformation tensor defined as

$$
\boldsymbol{C} = \boldsymbol{F}^{\mathrm{T}}\boldsymbol{F}\,, \quad \boldsymbol{b} = \boldsymbol{F}\boldsymbol{F}^{\mathrm{T}}\,. \tag{2.1.7}
$$

The relationships between Cauchy-Green deformation tensors are

$$
\boldsymbol{C} = \boldsymbol{F}^{-1}\,\boldsymbol{b}\,\boldsymbol{F}\,, \quad \boldsymbol{b} = \boldsymbol{F}\,\boldsymbol{C}\,\boldsymbol{F}^{-1}\,. \tag{2.1.8}
$$

Another important strain measure is obtained by introducing the difference in the squares of the undeformed and deformed lengths as

$$
\begin{aligned}
\frac{|d\mathbf{x}|^2 - |d\boldsymbol{X}|^2}{2} &= d\boldsymbol{X} \cdot \boldsymbol{E}\, d\boldsymbol{X}\,, \\
\frac{|d\mathbf{x}|^2 - |d\boldsymbol{X}|^2}{2} &= d\mathbf{x} \cdot \mathbf{e}\, d\mathbf{x}\,,
\end{aligned}
$$

where $\boldsymbol{E}$ is the Green-Lagrange strain tensor and $\mathbf{e}$ is the Euler-Almansi strain tensor, defined as

$$
\boldsymbol{E} = \frac{1}{2}\left(\boldsymbol{C} - \mathbf{I}\right)\,, \quad \mathbf{e} = \frac{1}{2}\left(\mathbf{I} - \boldsymbol{b}^{-1}\right)\,. \tag{2.1.9}
$$

These tensors are defined respectively in the reference ($\boldsymbol{E}$) or the current ($\boldsymbol{e}$) configuration. It is crucial to know the transformation properties between both configurations. The tensors in the two configurations can be related through operations called push-forward and pull-back. These operations play an important role in many theoretical derivations [9, 34, 119]. A push-forward operation transforms the reference configuration quantities into the current configuration ones. For example, push-forward of the Green-Lagrange strain tensor $\boldsymbol{E}$ is

$$
\mathbf{e} = \boldsymbol{F}^{-\mathrm{T}}\boldsymbol{E}\boldsymbol{F}^{-1}\,. \tag{2.1.10}
$$

A pull-back is the inverse operation, which transforms the current configuration quantities into the reference configuration ones. The pull-back of $\mathbf{e}$ is

$$
\boldsymbol{E} = \boldsymbol{F}^{\mathrm{T}}\mathbf{e}\boldsymbol{F}\,. \tag{2.1.11}
$$

### 2.1.2 Stress measures and equilibrium equations

Three stress measures are widely used in continuum mechanics. They are:

- The Cauchy stress tensor $\boldsymbol{\sigma}$ or true stress; it expresses the stress state in current configuration.
- The first Piola-Kirchhoff stress $\boldsymbol{P}$.
- The second Piola-Kirchhoff stress $\boldsymbol{S}$.

The equations that govern the mechanics of a solid include the balance laws for mass, linear momentum, and angular momentum.

### Conservation of mass

The law of conservation of mass states that the mass of a body does not change in time and can neither be created nor destroyed during a deformation process. It can be formulated in the reference (material) configuration $\Omega_0$ as:

$$J = \frac{\rho_0}{\rho}\,, \tag{2.1.12}$$

where $\rho_0$ is the reference density, $\rho$ is the density in the current configuration. The local form of conservation of mass with respect to the current (spatial) configuration $\Omega$ is written as:

$$\dot{\rho} + \rho \cdot \operatorname{div}(\dot{\mathbf{x}}) = 0\,. \tag{2.1.13}$$

where a superposed dot denotes the time derivative.

### Balance of linear momentum

The law of balance of linear momentum postulates that the change of the linear momentum is equal to the sum of all applied external surface and volume loads acting on the body. By ignoring the inertial term, the balance of linear momentum is described in the reference (material) configuration as

$$\operatorname{Div}(\boldsymbol{P}) + \rho_0\, \bar{\boldsymbol{B}} = \operatorname{Div}(\boldsymbol{F}\,\boldsymbol{S}) + \rho_0\, \bar{\boldsymbol{B}} = \boldsymbol{0}\,, \tag{2.1.14}$$

where $\bar{\boldsymbol{B}}$ is the vector of the reference body forces. The standard Neumann and Dirichlet boundary conditions apply

$$\begin{aligned} \boldsymbol{u} &= \bar{\boldsymbol{u}} \quad \text{on} \quad \Gamma_u\,, \\ \boldsymbol{P}\boldsymbol{N} &= \bar{\boldsymbol{T}} \quad \text{on} \quad \Gamma_t\,, \end{aligned} \tag{2.1.15}$$

where Dirichlet boundary conditions prescribe the displacement $\bar{\boldsymbol{u}}$ on $\Gamma_u$ and Neumann boundary conditions are used to apply reference boundary traction $\bar{\boldsymbol{T}}$ on $\Gamma_t$ at $t_0$.
The linear momentum balance equation can be equivalently expressed in the current (spatial) configuration $\Omega$ in terms of the Cauchy stress tensor as

$$\operatorname{div}(\boldsymbol{\sigma}) + \rho\, \bar{\boldsymbol{b}} = \boldsymbol{0}\,, \tag{2.1.16}$$

where $\rho$ and $\bar{\boldsymbol{b}}$ are, respectively, the density and the body forces in the current configuration and the following Neumann and Dirichlet boundary conditions apply

$$\begin{aligned} \boldsymbol{u} = \bar{\boldsymbol{u}} \quad &\text{on} \quad \gamma_u \,, \\ \boldsymbol{\sigma}\boldsymbol{n} = \bar{\boldsymbol{t}} \quad &\text{on} \quad \gamma_t \,, \end{aligned} \tag{2.1.17}$$

where $\bar{\boldsymbol{u}}$ and $\bar{\boldsymbol{t}}$ are prescribed on $\gamma_u$ and $\gamma_t$, respectively, at current $t$. In the infinitesimal deformation case the reference and current configurations are identical and the above momentum balance equation can be expressed in terms of Cauchy stress tensor of the infinitesimal theory.

### Balance of angular momentum

The law of balance of angular momentum postulates that the change of the angular momentum with respect to a point is equal to the sum of all applied external moments with respect to this point. From the balance of angular momentum, the following relation that connects the first Piola-Kirchhoff stress tensor $\boldsymbol{P}$ and the deformation gradient $\boldsymbol{F}$ is derived with respect to the reference (material) configuration

$$\boldsymbol{P}\boldsymbol{F}^{\mathrm{T}} = \boldsymbol{F}\boldsymbol{P}^{\mathrm{T}} \,. \tag{2.1.18}$$

Application of angular momentum balance law with respect to the current (spatial) configuration gives the symmetry property of the Cauchy stress tensor

$$\boldsymbol{\sigma} = \boldsymbol{\sigma}^{\mathrm{T}} \,. \tag{2.1.19}$$

### Transformation of stresses

Cauchy stress tensor and Piola-Kirchhoff stress tensors are related by Cauchy theorem, which is based on Newton's second and third laws. The theorem establishes a linear mapping between the traction vector ($\boldsymbol{T}$ or $\boldsymbol{t}$) and the normal vector ($\boldsymbol{N}$ or $\boldsymbol{n}$) of a differential surface element with a second-order tensor field ($\boldsymbol{P}$ or $\boldsymbol{\sigma}$) as:

$$\begin{aligned} \boldsymbol{P}\,\boldsymbol{N} &= \boldsymbol{T} \,, \\ \boldsymbol{\sigma}\,\boldsymbol{n} &= \boldsymbol{t} \,. \end{aligned} \tag{2.1.20}$$

Here, the vector $\boldsymbol{T}$ represents the first Piola-Kirchhoff traction vector and the vector $\boldsymbol{t}$ represents the Cauchy traction vector.

By using Nanson's formula (equation (2.1.6)), the relation between the Cauchy stress tensor $\boldsymbol{\sigma}$ and the first Piola-Kirchhoff stress tensor $\boldsymbol{P}$ is given by

$$\boldsymbol{\sigma} = J^{-1}\boldsymbol{P}\boldsymbol{F}^{\mathrm{T}} = \boldsymbol{\sigma}^{\mathrm{T}} \,, \tag{2.1.21}$$

which implies $\boldsymbol{P}\boldsymbol{F}^{\mathrm{T}} = \boldsymbol{F}\boldsymbol{P}^{\mathrm{T}}$. Therefore, the first Piola-Kirchhoff tensor $\boldsymbol{P}$ is, in general, an asymmetric tensor.

Instead of using the asymmetric first Piola-Kirchhoff stress tensor $\boldsymbol{P}$, a symmetric stress tensor called the second Piola-Kirchhoff stress tensor can be introduced. This is denoted as $\boldsymbol{S}$, and it is obtained from a complete pull back transformation of the Cauchy stress tensor and solely defined in the reference initial configuration

$$\boldsymbol{S} = J\boldsymbol{F}^{-1}\boldsymbol{\sigma}\boldsymbol{F}^{-\mathrm{T}} = \boldsymbol{F}^{-1}\boldsymbol{P} = \boldsymbol{S}^{\mathrm{T}} \,. \tag{2.1.22}$$

In contrast to the first Piola-Kirchhoff and Cauchy stress tensors, $\boldsymbol{S}$ does not have any physical interpretation in terms of surface tractions and cannot be measured experimentally. Another useful stress measure in the formulation of viscoelastic constitutive equations at finite strains is Kirchhoff stress tensor $\boldsymbol{\tau}$, which results from the push forward operation of the second Piola-Kirchhoff stress tensor $\boldsymbol{S}$ to the current configuration

$$\boldsymbol{\tau} = \boldsymbol{F}\boldsymbol{S}\boldsymbol{F}^{\mathrm{T}} \,, \quad \boldsymbol{\tau} = J\boldsymbol{\sigma} \,. \tag{2.1.23}$$

### 2.1.3 Hyperelastic constitutive laws

A material is considered to be hyperelastic, if its deformation process is described by a strain energy density function $\Psi$ which depends only on the deformation itself. The general set of hyperelastic constitutive equations in the reference and current configurations is given by

$$\begin{aligned} \boldsymbol{S} &= 2\frac{\partial\Psi(\boldsymbol{C})}{\partial\boldsymbol{C}} \,, \\ \boldsymbol{\sigma} &= \frac{2}{J}\boldsymbol{b}\frac{\partial\Psi(\boldsymbol{b})}{\partial\boldsymbol{b}} \,, \end{aligned} \tag{2.1.24}$$

where $\Psi$ is referred to as the strain energy density function. The so-called fourth order material tensor $\mathbb{C}$ in the reference configuration and $\mathbb{c}$ in the current configuration are given by

$$\begin{aligned} \mathbb{C} &= 4\frac{\partial^2\Psi(\boldsymbol{C})}{\partial\boldsymbol{C}\partial\boldsymbol{C}} \,, \\ \mathbb{c} &= \frac{4}{J}\boldsymbol{b}\frac{\partial^2\Psi(\boldsymbol{b})}{\partial\boldsymbol{b}\partial\boldsymbol{b}}\boldsymbol{b} \,, \end{aligned} \tag{2.1.25}$$

Using the push-forward and pull-back operations, the conversion between Lagrangian $\mathbb{C}$ and Eulerian $\mathbb{c}$ material tensors can be obtained as

$$\begin{aligned} \mathbb{c}_{ijkl} &= J^{-1}F_{iI}F_{jJ}F_{kK}F_{lL}\mathbb{C}_{IJKL} \,, \\ \mathbb{C}_{IJKL} &= JF^{-1}_{Ii}F^{-1}_{Jj}F^{-1}_{Kk}F^{-1}_{Ll}\mathbb{c}_{ijkl} \,. \end{aligned} \tag{2.1.26}$$

In case of infinitesimal strain, $\boldsymbol{E}$ is replaced by the infinitesimal strain tensor, $\boldsymbol{\varepsilon}$, and the second Piola-Kirchhoff stress $\boldsymbol{S}$ is replaced by the Cauchy stress tensor $\boldsymbol{\sigma}$ of the infinitesimal theory. Then the constitutive law is written as:

$$\boldsymbol{\sigma} = \frac{\Psi(\boldsymbol{\varepsilon})}{\partial\boldsymbol{\varepsilon}} \,, \tag{2.1.27}$$

with

$$\mathbb{c} = \frac{\partial^2\Psi(\boldsymbol{\varepsilon})}{\partial\boldsymbol{\varepsilon}\partial\boldsymbol{\varepsilon}} \,, \tag{2.1.28}$$

where $\mathbb{c}$ is the fourth order material tensor of the infinitesimal theory.

## 2.2 Material model

This section consists of two parts. In the first part, some material characteristics of rubber are described in order to select the appropriate material model. The second part introduces the constitutive equations for hyperelasticity and viscoelasticity in Subsections 2.2.2 and 2.2.3.

### 2.2.1 Rubber characteristics

This section illustrates and describes than main physical properties of elastomers. For an overview of rubber characteristics, see [23, 84].

#### Rubber hyperelasticity

One of the best known properties of elastomers is their ability to undergo large deformations without material failure. They return to their undeformed shape when the load is released. This reversible non-linear stress-strain behavior is called hyperelasticity.

#### Rubber incompressibility

The resistance of elastomers to the volume-changing deformation is enormous. Rubber is considered as a nearly incompressible material due to the fact that no changes in density can be remarked on uniaxial loading. A Poisson ratio of $\nu= 0.49$ is adopted in this work to model nearly incompressible material.

#### Viscoelastic properties of rubber

The material behavior of elastomers shows a time dependency, where the stress is dependent on the strain rate. This time dependency is called viscoelasticity and is attributed to a mixture of solid- and fluid-like properties. In experiments, phenomena like relaxation or creep of elastomers are usually observed. Relaxation stands for the decrease of stress under constant strain, while creep represents the increase of strain under constant stress. Elastomer materials used for tires usually undergo deformations in a large frequency range, showing different stress-strain relations at different frequencies. When a rubber tire slides on a rough rigid substrate, surface asperities induce pulsating forces. The cyclic loading and unloading causes a viscoelastic energy dissipation taking place in the bulk of the material, which is the main cause of hysteresis loss inside rubber.

For an accurate characterization and modelling of elastomers, a dynamic mechanical analysis is conducted. A periodic sinusoidal time-dependent strain is applied at an angular frequency $\omega$ and the resulting force is measured. Then, a strain-stress response including a time delay between both quantities is obtained. The phase lag $\delta\left(\omega\right)$ between stress $\sigma\left(t\right)$ and strain $\varepsilon\left(t\right)$ is a measure of the viscosity of the elastomer at a certain frequency.

$$\varepsilon\left(t\right)=\hat{\varepsilon}\cdot\sin\left(\omega t\right)\ ,\qquad\qquad \sigma\left(t\right)=\hat{\sigma}\cdot\sin\left(\omega t+\delta\left(\omega\right)\right)\ . \tag{2.2.1}$$

The phase lag is used to determine the dynamic complex modulus, which defines the ratio of stress to strain under oscillatory loading by using the applied stress amplitude $\hat{\varepsilon}$ and the measured phase lag and stress amplitude $\hat{\sigma}\left(\omega\right)$. This complex modulus consists of a real part and an imaginary part.

$$E\left(\omega\right)=E'\left(\omega\right)+i\cdot E''\left(\omega\right) \tag{2.2.2}$$

The real part $E'\left(\omega\right)$ is referred to as ”storage modulus”. It is a measure for the elastic response of the material and represents the stored energy inside the material.

$$E'\left(\omega\right)=\frac{\hat{\sigma}\left(\omega\right)}{\hat{\varepsilon}}\cdot\cos\left(\delta\left(\omega\right)\right) \tag{2.2.3}$$

The imaginary part is called ”loss modulus”, it denotes the amount of viscous energy dissipation in the material and represents the viscous response of the material.

$$E''\left(\omega\right)=\frac{\hat{\sigma}\left(\omega\right)}{\hat{\varepsilon}}\cdot\sin\left(\delta\left(\omega\right)\right) \tag{2.2.4}$$

In order to describe the viscoelastic material response, the generalized Maxwell model is used in this work, see Figure 2.2. The rheological model consists of a parallel connection of a spring and a number of spring-damper (Maxwell) elements. Each Maxwell element contains a linear spring and a damper. For each Maxwell element k, a Young's modulus $E_k$ and a relaxation time $\tau_k$ is determined. Six Maxwell elements are selected. This number is sufficient to cover a wide spectrum of excitation frequencies resulting from track roughness and it allows also simulating a broad distribution of viscous effects. The spring in front of the Maxwell elements is used to model the pure elastic equilibrium part of the viscoelastic response, whereas the Maxwell elements capture the non-equilibrium (time-dependent) part. In order to determine the Young's modulus of the equilibrium part, a tensile test has been carried out. The estimated parameters are listed in Table 2.1.

The storage modulus and the loss modulus of the generalized Maxwell model are approximated [113, 118] respectively as:

$$E'\left(\omega\right)=E_{\infty}+\sum_{k=1}^{N}\frac{E_k\tau_k^2\omega^2}{1+\tau_k^2\omega^2} \tag{2.2.5}$$

$$E''\left(\omega\right)=\sum_{k=1}^{N}\frac{E_k\tau_k\omega}{1+\tau_k^2\omega^2} \tag{2.2.6}$$

with $E_{\infty}$ is the long-term modulus. It is defined

$$E_{\infty}=E\left(\omega\rightarrow 0,\, t\rightarrow\infty\right) \tag{2.2.7}$$

**Table 2.1:** Generalized Maxwell model fitted for the styrene-butadiene rubber viscoelastic material [118].

| **Element** | **E** [**N**/$mm^2$] | $\tau$ [**s**] |
|---|---|---|
| **EQ** | 4.17 | - |
| **MW1** | 1.72 | 1.134e-02 |
| **MW2** | 7.36 | 2.628e-04 |
| **MW3** | 70.98 | 1.316e-05 |
| **MW4** | 505.87 | 1.295e-06 |
| **MW5** | 1125.85 | 7.708e-08 |
| **MW6** | 1185.94 | 4.200e-10 |

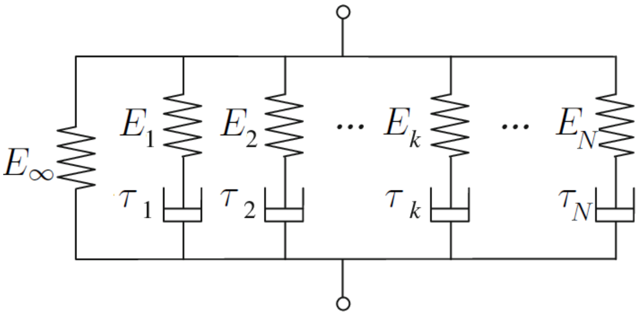

**Figure 2.2:** Schematic of a generalized Maxwell model consisting of N Maxwell elements

The instantaneous modulus $E_0$ is defined as

$$E_0 = E\left(\omega \rightarrow \infty, \, t \rightarrow 0\right) = E_\infty + \sum_{k=1}^{N} E_k \tag{2.2.8}$$

The discrete creep function is expressed as

$$H_r\left(\tau_k\right) = E_\infty + \sum_{k=1}^{N} E_k \cdot e^{-\frac{t}{\tau_k}} \tag{2.2.9}$$

The loss tangent is defined as

$$\tan\left(\delta\right) = \frac{E''\left(\omega\right)}{E'\left(\omega\right)} \tag{2.2.10}$$

### Mullins effect

In tire industry, sulfur and fillers are added to the raw material to adjust the final material properties. Furthermore, carbon black or silica is often used to increase the strength of the filled elastomer. Filled elastomers show a recognizable material hysteresis during different loading and unloading paths. The first loading of an elastomer leads to a stiffer response than the following cycles. This stress softening is called Mullins effect [58]. Mullins effect is attributed to the micromechanical breakage of hard filler clusters. Mullins effect investigation can be excluded by preconditioning the rubber samples before investigations. Since Mullins effect occurs only at initial loading, the following cycles are approximately identical. The energy loss because of material hysteresis under quasistatic loading is assumed to be small compared to the viscoelastic effects. Therefore, Mullins effect will be neglected in this work.

### Payne effect

For filled elastomers, another effect on the stress-strain behavior is called Payne effect [66, 67]. This effect states that under cyclic loading conditions, the storage modulus decreases rapidly with increasing amplitude within a range between 0.1 and 20 % strain. Payne effect increases by increasing the filler content and vanishes for unfilled elastomers. It can be excluded by using also preconditioned test samples for the dynamic mechanical analysis. Payne effect is not considered in this study.

### Thermal effects

In rubber, a strong coupling between thermal and mechanical properties exists for large sliding velocities and can be neglected for low macroscopic velocities [114]. Thus, this work is limited for low macroscopis sliding velocities. Thermal effects will be left for future work.

## 2.2.2 Isotropic hyperelastic material models

This subsection describes the hyperelastic material behavior of rubber. For an isotropic material with the same response in all directions, the strain energy density function can be described as a function of the three independent principal invariants $I_1$, $I_2$ and $I_3$ of $\boldsymbol{C}$

$$\Psi = \Psi\left(I_1, I_2, I_3\right) \ , \tag{2.2.11}$$

with

$$\begin{aligned} I_1 &= \operatorname{tr}\left(\boldsymbol{C}\right) \\ I_2 &= \tfrac{1}{2}\left[\operatorname{tr}^2\left(\boldsymbol{C}\right) - \operatorname{tr}\left(\boldsymbol{C}^2\right)\right] \ , \\ I_3 &= \det\left(\boldsymbol{C}\right) \end{aligned} \tag{2.2.12}$$

The derivatives of the invariants can be computed as follows

$$\frac{\partial I_1}{\partial \mathbf{C}} = \mathbf{1}; \qquad \frac{\partial I_2}{\partial \mathbf{C}} = I_1 \mathbf{1} - \mathbf{C}; \qquad \frac{\partial I_3}{\partial \mathbf{C}} = I_3 \mathbf{C}^{-1} \tag{2.2.13}$$

The 2nd Piola-Kirchhoff stress $\boldsymbol{S}$ is extracted by applying the chain rule as follows

$$\boldsymbol{S} = 2\frac{\partial \Psi}{\partial \boldsymbol{C}} = 2\left[\left(\frac{\partial \Psi}{\partial I_1} + I_1 \frac{\partial \Psi}{\partial I_2}\right) \cdot \mathbf{1} - \frac{\partial \Psi}{\partial I_2} \cdot \boldsymbol{C} + I_3 \frac{\partial \Psi}{\partial I_3} \cdot \boldsymbol{C}^{-1}\right] \tag{2.2.14}$$

For the purpose of describing the hyperelastic response of the rubber, a neo-Hookean constitutive law is used. The neo-Hookean model is one of the simplest isotropic hyperelastic material models. A specific representation of the neo-Hookean strain energy function [16] with material parameters $\Lambda$ and $\mu$ is used to describe hyperelastic response

$$\Psi = \frac{\mu}{2}\left(I_1 - 3 - 2\ln J\right) + \frac{\Lambda}{4}\left(J^2 - 1 - 2\ln J\right) , \tag{2.2.15}$$

where the Jacobian $J = \det(\boldsymbol{F})$ is the determinant of the deformation gradient, $\Lambda$ and $\mu$ are the Lamé constants. Their relation to the elastic modulus E and the Poisson's ratio $\nu$ is

$$\mu = \frac{E}{2\left(1+\nu\right)} \qquad \Lambda = \frac{E\nu}{\left(1+\nu\right)\left(1-2\nu\right)} . \tag{2.2.16}$$

The derivatives of the neo-Hookean strain energy density function with respect to the invariants are as follows

$$\frac{\partial \Psi}{\partial I_1} = \frac{\mu}{2}; \qquad \frac{\partial \Psi}{\partial I_2} = 0; \qquad \frac{\partial \Psi}{\partial I_3} = \frac{\partial \Psi}{\partial J} \cdot \frac{\partial J}{\partial I_3} = \left(\frac{\Lambda}{2}\left(J - \frac{1}{J}\right) - \frac{\mu}{J}\right)\left(\frac{1}{2J}\right) . \tag{2.2.17}$$

Introducing equation (2.2.17) into equation (2.2.14) gives the 2nd Piola-Kirchhoff stress tensor.

$$\mathbf{S} = \mu\left(\mathbf{1} - \mathbf{C}^{-1}\right) + \frac{\Lambda}{2}\left(J^2 - 1\right)\mathbf{C}^{-1} . \tag{2.2.18}$$

The Cauchy stress is obtained via a push-forward transformation according to equation (2.1.10) as

$$\boldsymbol{\sigma} = \frac{1}{J}\mathbf{F} \cdot \mathbf{S} \cdot \mathbf{F}^T = \frac{\mu}{J}\left(\mathbf{b} - \mathbf{1}\right) + \frac{\Lambda}{2J}\left(J^2 - 1\right)\mathbf{1} . \tag{2.2.19}$$

## 2.2.3 Viscoelastic material models

One of the main goals of this work is to study the influence of the rheological linearity on the calculation of rubber friction. For this purpose, the results of a linear viscoelastic model within the small deformation framework will be compared to the results of a linear viscoelastic model within the finite deformation framework.

### Linear viscoelasticity

In linear viscoelasticity one has small deformations and small deformation rates. The analytical approach of Persson, see Section 4.2, is utilized within the framework of linear viscoelasticity with small deformations. The goal of this subsection is the presentation of a compact and efficient linear viscoelastic formulation based on the generalized Maxwell model, i.e. a finite number of separate Maxwell elements are arranged in parallel with an elastic Hooke-element, see Figure 2.2. Due to its simplicity the creep function is determined directly using Prony series by rewriting equation (2.2.9) as:

$$H_r\left(\tau_k\right) = E_0\left[1 - \sum_{k=1}^{N}\frac{E_k}{E_0}\left(1 - e^{-\frac{t}{\tau_k}}\right)\right] \tag{2.2.20}$$

### Finite linear viscoelasticity

In finite linear viscoelasticity, finite deformations are allowed. However, the evolution equation of the model is linear [48, 49]. This model was suggested by Reese and Govindjee [82] in order to model the dissipative physics of hysteresis friction within the finite deformation framework. It is able to capture the large deformations arising in the contact zone of the rubber sliding over a rough surface.

The strain energy function is split into a time-independent equilibrium part (EQ) and a time-dependent dissipative non-equilibrium part (NEQ). The equilibrium part is defined by a hyperelastic spring, see Figure 2.2. The non-equilibrium part is modelled by N Maxwell elements connected in parallel to the equilibrium spring.

For many materials it is convenient to decompose the deformation gradient into a volumetric part and a distortional part. This is particularly useful when there is no volume change in the material when it deforms as in case of rubber. The idea of multiplicative split in rubber was first suggested by Lubliner [55] and then adopted by many researchers [48, 49, 81, 82]. The model assumes that the deformation gradient **F** of the viscoelastic material is multiplicatively decomposed into an elastic (e) and an inelastic (i) viscous part

$$\mathbf{F} = \mathbf{F}_e \cdot \mathbf{F}_i \tag{2.2.21}$$

The right Cauchy-Green tensor for the inelastic part associated with the reference configuration is defined for each Maxwell element as:

$$\mathbf{C}_i^k = \left(\mathbf{F}_i^k\right)^T \cdot \mathbf{F}_i^k \tag{2.2.22}$$

Since only the elastic part of deformation has an influence on the stresses, the left Cauchy-Green tensor can be written for each Maxwell element as:

$$\mathbf{b}_e^k = \mathbf{F}_e^k \cdot \left(\mathbf{F}_e^k\right)^T = \mathbf{F}^k \cdot \left(\mathbf{C}_i^k\right)^{-1} \cdot \left(\mathbf{F}^k\right)^T \tag{2.2.23}$$

The inelastic viscous variables are computed using the following evolution equation [82]:

$$\dot{\mathbf{C}}_i^k = \frac{1}{\tau^k}(\mathbf{C} - \mathbf{C}_i^k) \tag{2.2.24}$$

This evolution equation has the same structure form as the evolution equation of linear viscoelasticity. It can be integrated in time using the trapezoidal rule [51] as follows:

$$\left(\mathbf{C}_i^k\right)^{n+1} = \frac{\Delta t}{2\tau^k + \Delta t}(\mathbf{C}^n + \mathbf{C}^{n+1} - \left(\mathbf{C}_i^k\right)^n) + \frac{2\tau^k}{2\tau^k + \Delta t}\left(\mathbf{C}_i^k\right)^n \tag{2.2.25}$$

The initial value for $\mathbf{C}_i^0$ is determined as the identity tensor.

The total Cauchy stress is the sum of an equilibrium and a non-equilibrium part.

$$\boldsymbol{\sigma} = \boldsymbol{\sigma}_{EQ} + \sum_{k=1}^{N} \boldsymbol{\sigma}_{NEQ}^k \tag{2.2.26}$$

The equilibrium part follows from equation (2.2.19)

$$\boldsymbol{\sigma}_{EQ} = \frac{\mu_{EQ}}{J}\left(\mathbf{b} - \mathbf{1}\right) + \frac{\Lambda_{EQ}}{2J}\left(J^2 - 1\right)\mathbf{1} \tag{2.2.27}$$

while the non-equilibrium contribution of the kth Maxwell element is formulated using the elastic left Cauchy-Green tensor $\mathbf{b}_e^k$ and its third invariant $J_e^k$ as

$$\boldsymbol{\sigma}_{NEQ}^k = \frac{\mu^k}{J}\left(\mathbf{b}_e^k - \mathbf{1}\right) + \frac{\Lambda^k}{2J}\left(\left(J_e^k\right)^2 - 1\right)\mathbf{1} \tag{2.2.28}$$

The elastic (equilibrium) part of the material tangent in the initial configuration is derived as follows

$$\mathbb{C}_{EQ} = 2\frac{\partial \boldsymbol{S}_{EQ}}{\partial \boldsymbol{C}} = \frac{\Lambda_{EQ}}{J}\boldsymbol{C}^{-1}\cdot\boldsymbol{C}^{-1} + \left(\frac{\Lambda_{EQ}}{J}\left(J^2 - 1\right) - \frac{2\mu_{EQ}}{J}\right)\frac{\partial \boldsymbol{C}^{-1}}{\partial \boldsymbol{C}} \tag{2.2.29}$$

The derivative $\frac{\partial \boldsymbol{C}^{-1}}{\partial \boldsymbol{C}}$ is given as [34]

$$\frac{\partial \boldsymbol{C}^{-1}}{\partial \boldsymbol{C}} = -\boldsymbol{C}^{-1}\otimes\boldsymbol{C}^{-1} \tag{2.2.30}$$

or in the index notation as

$$\frac{\partial C_{IJ}^{-1}}{\partial C_{KL}} = -C_{IK}^{-1}\otimes C_{JL}^{-1} = \frac{-1}{2}\left(C_{IK}^{-1}C_{JL}^{-1} + C_{IL}^{-1}C_{KJ}^{-1}\right) \tag{2.2.31}$$

Thus, the material tangent in the initial configuration is written as follows

$$\mathbb{C}_{EQ} = \frac{\Lambda_{EQ}}{J}\boldsymbol{C}^{-1}\cdot\boldsymbol{C}^{-1} - \left(\frac{\Lambda_{EQ}}{J}\left(J^2 - 1\right) - \frac{2\mu_{EQ}}{J}\right)\boldsymbol{C}^{-1}\otimes\boldsymbol{C}^{-1} \tag{2.2.32}$$

The spatial elasticity tensor is calculated with a push-forward to the current configuration according to equation (2.1.26), so the elastic part of the total material tangent has the following structure

$$\mathbb{c}_{EQ} = \frac{2}{J}\left(\frac{\Lambda_{EQ}}{2}\left(1 - J^2\right) + \mu_{EQ}\right)\mathcal{I}^{sym} + \left(\Lambda_{EQ}J\right)\mathbf{1}\otimes\mathbf{1} \tag{2.2.33}$$

where $\mathcal{I}^{sym}$ is a fourth order unit tensor.
In order to derive the viscous part of the material tangent, $\boldsymbol{\sigma}_{NEQ}^k$ written in equation (2.2.28) will be rearranged as

$$\boldsymbol{\sigma}_{NEQ}^k = \left(\frac{\Lambda^k}{2J}\left(\left(J_e^k\right)^2 - 1\right) - \frac{\mu^k}{J}\right)\mathbf{1} + \left(\frac{\mu^k}{J}\right)\boldsymbol{b}_e^k \tag{2.2.34}$$

In the general isotropic case, the Cauchy stress tensor can be written as [34]

$$\boldsymbol{\sigma}_{NEQ}^k = \alpha_0\mathbf{1} + \alpha_1\mathbf{b}_e^k + \alpha_2\mathbf{b}_e^k\cdot\mathbf{b}_e^k \tag{2.2.35}$$

Comparing the aforementioned equations to each other, one can find that:

$$\alpha_0 = \frac{\Lambda^k}{2J}\left(\left(J_e^k\right)^2 - 1\right) - \frac{\mu^k}{J}; \qquad \alpha_1 = \frac{\mu^k}{J}; \qquad \alpha_2 = 0 \tag{2.2.36}$$

Löhnert [51] derives the following expression for the current configuration

$$\begin{aligned}\boldsymbol{\sigma}^k_{NEQ} = \tfrac{1}{J}\,\mathbf{F}\cdot\mathbf{S}^k_{NEQ}\cdot\mathbf{F}^T = [&\mathbf{1}\otimes\mathbf{B}_0 + \left(\mathbf{1}\otimes\mathbf{B}_{(i)0}\right):\mathcal{M}\\ &+\mathbf{b}_e^k\otimes\mathbf{B}_1 + \left(\mathbf{b}_e^k\otimes\mathbf{B}_{(i)1}\right):\mathcal{M}\\ &+\left(\mathbf{b}_e^k\cdot\mathbf{b}_e^k\right)\otimes\mathbf{B}_2 + \left(\left(\mathbf{b}_e^k\cdot\mathbf{b}_e^k\right)\otimes\mathbf{B}_{(i)2}\right):\mathcal{M}\\ &-\alpha_1\mathcal{X}\left(\mathbf{b}_e^k,\mathbf{b}_e^k\right):\mathcal{M} - \alpha_2\mathcal{X}\left(\mathbf{b}_e^k,\mathbf{b}_e^k\cdot\mathbf{b}_e^k\right):\mathcal{M} - \alpha_2\mathcal{X}\left(\mathbf{b}_e^k\cdot\mathbf{b}_e^k,\mathbf{b}_e^k\right):\mathcal{M}\\ &-\alpha_0\mathcal{I} + \alpha_2\mathcal{X}\left(\mathbf{b}_e^k,\mathbf{b}_e^k\right)]:\mathbf{A}\end{aligned} \tag{2.2.37}$$

where $\mathcal{X}$ is a fourth order tensor which is described in the index notation by the following equation

$$\mathcal{X}_{ijkl} = \frac{1}{2}\left(Y_{ik}Z_{lj} + Y_{il}Z_{kj}\right) \tag{2.2.38}$$

$\mathcal{M}$ is a fourth order tensor which can be determined as a result of the integration of the evolution equation. It depends strongly on the used integration algorithm. For the trapezoidal rule, it is given by Löhnert [51]:

$$\mathcal{M} = \frac{\Delta t}{2\tau^k + \Delta t}\mathcal{I} \tag{2.2.39}$$

where $\mathcal{I}$ is the fourth order unit tensor.
$\mathbf{B}_j$ and $\mathbf{B}_{(i)j}$ can be determined using the derivatives of all $\alpha_j$ with respect to $\mathbf{C}$ and $\mathbf{C}_i$ respectively

$$\mathbf{B}_j = \mathbf{F}\cdot\frac{\partial\alpha_j}{\partial\mathbf{C}}\cdot\mathbf{F}^T \qquad ; \qquad \mathbf{B}_{(i)j} = \mathbf{F}\cdot\frac{\partial\alpha_j}{\partial\mathbf{C}_i}\cdot\mathbf{F}^T \tag{2.2.40}$$

$$\mathbf{B}_0 = \frac{\Lambda^k}{2J}\left(J_e^k\right)^2\mathbf{1} \qquad \mathbf{B}_1 = \mathbf{0} \qquad \mathbf{B}_2 = \mathbf{0} \tag{2.2.41}$$

$$\mathbf{B}_{(i)0} = -\frac{\Lambda^k}{2J}\left(J_e^k\right)^2\mathbf{b}_e^k \qquad \mathbf{B}_{(i)1} = \mathbf{0} \qquad \mathbf{B}_{(i)2} = \mathbf{0} \tag{2.2.42}$$

Substituting and matching with the following equation

$$\Delta\boldsymbol{\sigma}^k_{NEQ} = \frac{1}{J}\mathbf{F}\cdot\Delta\mathbf{S}^k_{NEQ}\cdot\mathbf{F}^T = \mathbb{C}^k_{NEQ} : \left(\frac{1}{2}\underbrace{\mathbf{F}^{-T}\cdot\Delta\mathbf{C}\cdot\mathbf{F}^{-1}}_{:=\mathbf{A}}\right) \tag{2.2.43}$$

yields the viscous part of the material tangent that is related to $\boldsymbol{\sigma}^k_{NEQ}$

$$\begin{aligned}\mathbb{C}^k_{NEQ} = &\tfrac{\Lambda^k}{J}\left(J_e^k\right)^2\mathbf{1}\otimes\mathbf{1} - \tfrac{\Lambda^k}{J}\left(J_e^k\right)^2\tfrac{\Delta t}{2\tau^k+\Delta t}\mathbf{1}\otimes\mathbf{b}_e^k - \tfrac{2\mu^k}{J}\tfrac{\Delta t}{2\tau^k+\Delta t}\mathcal{X}\left(\mathbf{b}_e^k,\mathbf{b}_e^k\right)\\ &+\tfrac{2\mu^k}{J}\mathcal{I} - \tfrac{\Lambda^k}{J}\left(\left(J_e^k\right)^2 - 1\right)\mathcal{I}\end{aligned} \tag{2.2.44}$$

### 2.2.4 Weak form of equilibrium

In order to solve the partial differential equation resulting from the balance of linear momentum in Subsection 2.1.2, weak forms are derived for the later introduced finite element method in Subsection 2.2.6. The weak form of equilibrium G is divided into a continuum or bulk contribution (b) and a contact contribution (c). This subsection deals only with the continuum mechanical part $G_b$ and must be extended with the contact contribution $G_c$, which is discussed separately later.

A weak form of a differential equation G is derived by multiplying the differential equation with a test function and integrating over the domain. The test function is a virtual displacement function that equals zero at the Dirichlet boundary. The continuum contribution to the strong form of the balance of the linear momentum described in the initial (equation 2.1.14) or the current configuration (equation 2.1.16) is multiplied with the test function $\delta \boldsymbol{u}$. The detailed development can be found in [9, 34, 121]. The continuum bulk contribution to the weak form of equilibrium in the initial (reference) configuration is written as

$$G_b\left(\boldsymbol{u}, \delta \boldsymbol{u}\right) = \int_{\Omega_0} \boldsymbol{S} : \delta \boldsymbol{E} \, dV - \int_{\Omega_0} \bar{\boldsymbol{B}} \, \rho_0 \cdot \delta \boldsymbol{u} \, dV - \int_{\Gamma_t} \bar{\boldsymbol{T}} \cdot \delta \boldsymbol{u} \, dA \tag{2.2.45}$$

where $\delta \boldsymbol{u}$ is the virtual displacement field and $\delta \boldsymbol{E}$ is the virtual variation of the Green-Lagrange strain tensor. It is written as:

$$\delta \boldsymbol{E} = \frac{1}{2} \left( \boldsymbol{F}^T \mathrm{Grad}\ (\delta \boldsymbol{u}) + \mathrm{Grad}^T\ (\delta \boldsymbol{u})\ \boldsymbol{F} \right) \tag{2.2.46}$$

The terms

$$\begin{aligned} \delta W_{\mathrm{ext}}^{\mathrm{u}} &= \int_{\Omega_0} \bar{\boldsymbol{B}} \, \rho_0 \cdot \delta \boldsymbol{u} \, dV + \int_{\Gamma_t} \bar{\boldsymbol{T}} \cdot \delta \boldsymbol{u} \, dA \,, \\ \delta W_{\mathrm{int}}^{\mathrm{u}} &= \int_{\Omega_0} \boldsymbol{S} : \delta \boldsymbol{E} \, dV \,. \end{aligned} \tag{2.2.47}$$

are known as external virtual work ($\delta W_{\mathrm{ext}}^{\mathrm{u}}$) and internal virtual work ($\delta W_{\mathrm{int}}^{\mathrm{u}}$).

Similarly, the continuum bulk contribution to the weak form of equilibirum in the current (spatial) configuration can be expressed as

$$G_b\left(\boldsymbol{u}, \delta \boldsymbol{u}\right) = \int_{\Omega} \left( \mathrm{div}\left(\boldsymbol{\sigma}\right) + \rho \, \bar{\boldsymbol{b}} \right) \cdot \delta \boldsymbol{u} \, dv - \int_{\gamma_t} \bar{\boldsymbol{t}} \cdot \delta \boldsymbol{u} \, da \,, \tag{2.2.48}$$

With the use of the divergence theorem

$$\mathrm{div}\left(\boldsymbol{\sigma} \cdot \delta \boldsymbol{u}\right) = \mathrm{div}\left(\boldsymbol{\sigma}\right) \cdot \delta \boldsymbol{u} + \boldsymbol{\sigma} : \mathrm{grad}\left(\delta \boldsymbol{u}\right) \tag{2.2.49}$$

the equation is transferred to

$$G_b\left(\boldsymbol{u}, \delta \boldsymbol{u}\right) = \int_{\Omega} \left( \mathrm{div}\left(\boldsymbol{\sigma} \cdot \delta \boldsymbol{u}\right) - \boldsymbol{\sigma} : \mathrm{grad}\left(\delta \boldsymbol{u}\right) + \rho \, \bar{\boldsymbol{b}} \right) \cdot \delta \boldsymbol{u} \, dv - \int_{\gamma_t} \bar{\boldsymbol{t}} \cdot \delta \boldsymbol{u} \, da \,. \tag{2.2.50}$$

Further simplification can be done using the Gauss theorem, leading to

$$G_b(\boldsymbol{u},\delta\boldsymbol{u}) = \int_\Omega \boldsymbol{\sigma} : \operatorname{grad}^s(\delta\boldsymbol{u})\, dv - \int_\Omega \bar{\boldsymbol{b}}\,\rho\cdot\delta\boldsymbol{u}\, dv - \int_{\gamma_t} \bar{\boldsymbol{t}}\cdot\delta\boldsymbol{u}\, da. \tag{2.2.51}$$

The external and the internal virtual works are

$$\begin{aligned} \delta W^{\mathrm{u}}_{\mathrm{ext}} &= \int_\Omega \bar{\boldsymbol{b}}\,\rho\cdot\delta\boldsymbol{u}\, dv + \int_{\gamma_t} \bar{\boldsymbol{t}}\cdot\delta\boldsymbol{u}\, da\,, \\ \delta W^{\mathrm{u}}_{\mathrm{int}} &= \int_\Omega \boldsymbol{\sigma} : \operatorname{grad}^s(\delta\boldsymbol{u})\, dv\,. \end{aligned} \tag{2.2.52}$$

where grad $^s$ is the symmetric part of the gradient. It is written as:

$$\operatorname{grad}^s(\delta\boldsymbol{u}) := \frac{1}{2}\left[\operatorname{grad}(\delta\boldsymbol{u}) + \operatorname{grad}^T(\delta\boldsymbol{u})\right]. \tag{2.2.53}$$

### 2.2.5 Linearization of the weak form of equilibrium

The continuum bulk contribution to the weak form of equilibrium in the forms (2.2.45) or (2.2.51) is generally non-linear. The tangent stiffness matrix for each step can be obtained by linearization of those contributions to the weak form of equilibrium with respect to the displacements $\boldsymbol{u}$. In the bulk contribution to the weak form equation, only the internal virtual work depends on the deformation. All other terms are independent of the deformation and hence of the displacements.

The continuum bulk contribution to the weak form is linearized with respect to the displacements $\boldsymbol{u}$ in the the material (reference) description as [34]

$$\Delta G^u_b = \int_{\Omega_0} \left[\operatorname{Grad}^s(\delta\boldsymbol{u}) : \operatorname{Grad}^s(\Delta\boldsymbol{u})\,\boldsymbol{S} + \boldsymbol{F}^T\operatorname{Grad}^s(\delta\boldsymbol{u}) : \mathbb{C} : \boldsymbol{F}^T\operatorname{Grad}^s(\Delta\boldsymbol{u})\right] dV, \tag{2.2.54}$$

or in index notation as

$$\Delta G^u_b = \int_{\Omega_0} \frac{\partial\delta u_a}{\partial X_B}\left(\delta_{ab}S_{BD} + F_{aA}F_{bC}\mathbb{C}_{ABCD}\right)\frac{\partial\Delta u_b}{\partial X_D} dV, \tag{2.2.55}$$

where $\Delta(\cdot)$ denotes the linearization operator. The detailed derivations can be found in [9, 34, 121].

The linearization of the bulk contribution to the weak form in the current configuration can be stated as [121]

$$\Delta G^u_b = \int_\Omega \left[(\operatorname{grad}^s(\delta\boldsymbol{u})\cdot\boldsymbol{\sigma}) : \operatorname{grad}^s(\Delta\boldsymbol{u}) + \operatorname{grad}^s(\delta\boldsymbol{u}) : \mathbb{c} : \operatorname{grad}^s(\Delta\boldsymbol{u})\right] dv. \tag{2.2.56}$$

It can also be formulated in index notation as

$$\Delta G^u_b = \int_\Omega \frac{\partial\delta u_a}{\partial x_b}\left(\delta_{ac}\sigma_{bd} + \mathbb{c}_{abcd}\right)\frac{\partial\Delta u_c}{\partial x_d} dv. \tag{2.2.57}$$

### 2.2.6 Finite element discretization of the continuum

The idea of the finite element method (FEM) depends on a subdivision of a domain in a defined, finite number of elements approximating the solution [119, 127]. Applying the methodology to solid mechanics means that a body $\Omega$ is approximated by a number $\mathrm{n_e}$ of elements $\Omega_e$.

$$\Omega \approx \Omega^{\mathrm{h}} = \bigcup_{\mathrm{e}=1}^{\mathrm{n_e}} \Omega_{\mathrm{e}} \tag{2.2.58}$$

where $\Omega_{\mathrm{e}} \subset \Omega_{\mathrm{h}}$ is the domain occupied by element e in the current configuration. The superscript $h$ is used to denote an approximation. The solution field (displacement $\boldsymbol{u}(\mathbf{x})$) is approximated element-wise.

The displacement solution field can be expressed by the nodal values $\boldsymbol{u_I}$ using the shape functions $N_I$ to interpolate the solution for the whole element. This is done by summation of all $n_p$ nodal contributions as

$$\boldsymbol{u}(\mathbf{x}) \approx \boldsymbol{u}^{\mathrm{h}}(\mathbf{x}) = \sum_{I=1}^{n_p} N_I(\mathbf{x})\, \boldsymbol{u}_I\,. \tag{2.2.59}$$

In order to simplify the construction of shape functions for arbitrary finite elements, the isoparametric concept is often used in the finite element framework. The classical isoparametric concept uses the same shape functions for the geometry and the solution field on a reference element with the reference coordinates $\boldsymbol{\xi}$

$$\mathbf{x}(\boldsymbol{\xi}) \approx \mathbf{x}^{\mathrm{h}}(\boldsymbol{\xi}) = \sum_{I=1}^{n_p} N_I(\boldsymbol{\xi})\, \mathbf{x}_I\,, \quad \boldsymbol{u}(\boldsymbol{\xi}) \approx \boldsymbol{u}^{\mathrm{h}}(\boldsymbol{\xi}) = \sum_{I=1}^{n_p} N_I(\boldsymbol{\xi})\, \boldsymbol{u}_I\,. \tag{2.2.60}$$

Furthermore, the virtual displacement $\delta\boldsymbol{u}$ is discretized using the same shape functions $N_I$ (Bubnov-Galerkin-Approach)

$$\delta\boldsymbol{u}(\boldsymbol{\xi}) \approx \delta\boldsymbol{u}^{\mathrm{h}}(\boldsymbol{\xi}) = \sum_{I=1}^{n_p} N_I(\boldsymbol{\xi})\, \delta\boldsymbol{u}_I\,. \tag{2.2.61}$$

The shape functions $N_I$ are constructed in a way that they equal one at node I and are zero at all other nodes J (Kronecker-delta property). Furthermore, the partition of unity ensures that the sum of all shape functions in one element equals one at each position:

$$N_I(\boldsymbol{\xi}_J) = \delta_{IJ}\,, \quad \sum_{I=1}^{n_p} N_I(\boldsymbol{\xi}) = 1. \tag{2.2.62}$$

The trilinear shape functions for a three-dimensional hexahedral eight node element read

$$N_I^{3D}(\boldsymbol{\xi}) = \frac{1}{8}(1+\xi_I\xi)(1+\eta_I\eta)(1+\zeta_I\zeta) \tag{2.2.63}$$

Similarly, the bilinear shape functions for a two-dimensional quadrilateral 4-node element are obtained as follows

$$N_I^{2D}(\boldsymbol{\xi}) = \frac{1}{4}(1+\xi_I\xi)(1+\eta_I\eta) \tag{2.2.64}$$

Mappings between the reference configuration $\Omega_r$, the initial configuration, and the current configuration are derived as

$$\boldsymbol{J}(\boldsymbol{\xi}) = \frac{\partial \mathbf{X}(\boldsymbol{\xi})}{\partial \boldsymbol{\xi}} = \sum_I \mathbf{X}_I \otimes \frac{\partial N_I(\boldsymbol{\xi})}{\partial \boldsymbol{\xi}}\ , \quad \boldsymbol{j}(\boldsymbol{\xi}) = \frac{\partial \mathbf{x}(\boldsymbol{\xi})}{\partial \boldsymbol{\xi}} = \sum_I \mathbf{x}_I \otimes \frac{\partial N_I(\boldsymbol{\xi})}{\partial \boldsymbol{\xi}}\ . \tag{2.2.65}$$

$\boldsymbol{J}$ and $\boldsymbol{j}$ are called the jacobian matrix in the initial and the current configuration, respectively.

Using the aforementioned mapping scheme, integrals can be transferred to the reference element. These integrals are usually solved using Gaussian integration scheme, which solves the integral approximately. This is performed by introducing a summation over the function evaluated at a certain number of integration points $n_g$ multiplied with the corresponding weight function $\omega_g$ for each integration point. The integration is given in the following form:

$$\int_{\Omega_e} \boldsymbol{f}(\mathbf{x})\, dv = \int_{\Omega_r} \boldsymbol{f}(\mathbf{x}(\boldsymbol{\xi}))\det \boldsymbol{j}(\boldsymbol{\xi})\ dv \approx \sum_{g=1}^{n_g} \boldsymbol{f}(\mathbf{x}(\boldsymbol{\xi}_g))\,\omega_g \det \boldsymbol{j}(\boldsymbol{\xi}_g) \tag{2.2.66}$$

where $\boldsymbol{f}(\mathbf{x})$ is a function which depends on the current coordinate vector $\mathbf{x}$. The coordinates of the integration points ($\boldsymbol{\xi}_g$) are listed in many books, for example [119]. The inner part of the bulk contribution to the weak form based on the balance of linear momentum $G_b^{u,int}$ is determined by the first terms of the equation (2.2.51) containing the Cauchy stress and the gradient of the virtual displacement

$$\int_{\Omega} \boldsymbol{\sigma} : \operatorname{grad}^s \delta\boldsymbol{u}\ dv \approx \bigcup_{\mathrm{e}=1}^{\mathrm{n_e}} \sum_{I=1}^{n_p} \delta\boldsymbol{u}_I^T \int_{\Omega_e} (\operatorname{grad} N_I)^T \cdot \boldsymbol{\sigma}\, dv = \delta\tilde{\boldsymbol{u}}^T \boldsymbol{R}_{int}(\boldsymbol{u})\,. \tag{2.2.67}$$

The finite element formulation is introduced using the assembling operator $\bigcup$ over all elements $n_e$. Thus, the volume integral over the whole domain is transferred to an integral over the element domain and a summation over all nodes. The same shape functions like for the displacement are used for the virtual displacement. The derived element contributions in equation (2.2.67) are integrated over the volume of the finite element, using the introduced Gaussian integration scheme in equation (2.2.66). In the following step, the assembled virtual displacement $\tilde{\boldsymbol{u}}$ is multiplied with the assembled vector of internal nodal forces $R(\boldsymbol{u})$ using the aforementioned Gaussian integration scheme. The reader is referred to the books of Wriggers [119] and Zienkiewicz [127] for further details regarding the assembly process.

In addition to the internal forces, external forces are applied as boundary conditions by body forces and tractions at the body surface. Since body forces $\bar{\boldsymbol{b}}$ are neglected in this work, only surface tractions $\bar{\boldsymbol{t}}$ are transferred in the same way as the internal nodal forces

$$\int_{\gamma_t} \bar{\boldsymbol{t}} \cdot \delta \boldsymbol{u} \, da \approx \bigcup_{\mathrm{e}=1}^{\mathrm{n_e}} \sum_{I=1}^{n_p} \delta \boldsymbol{u}_I^T \int_{\gamma_e} N_I \, \bar{\boldsymbol{t}} \, da = \delta \tilde{\boldsymbol{u}}^T \boldsymbol{P}. \tag{2.2.68}$$

with the difference that a surface integral has to be evaluated and the resulting assembled vector of traction forces is named $\boldsymbol{P}$ assuming an independence of the displacement.

## 2.3 Basics of contact mechanics

In order to model a rubber block sliding on a rough surface, a close look on contact mechanics is essential. This section deals with the basic formulations concerning normal and tangential contact of two deformable bodies. The start will be with the kinematic description of contact in normal and tangential directions of the contact interface followed by the formulation of the contact interface constraints. Then, the most common solution methods for contact problems are presented, introducing the weak form. The derived weak forms provide the basis for the discretization of the contact problem with finite elements.

For further details regarding derivations of contact terms and their implementation in the FEM, the reader is referred to, for example, Wriggers [121], Laursen [43], De Lorenzis [18] and Willner [116].

### 2.3.1 Contact kinematics

Contact kinematics defines pairing of two contact points and the gap between them in normal and tangential directions. In order to express the contact constraints, the traditional master-slave concept is used, in which one of the bodies is defined as master and denoted with the superscript 1, and the other as slave and denoted with the superscript 2. The master surface will be parameterized through the convective coordinates.

**Kinematics in normal direction**

In order to define the normal gap between two contacting bodies, the following steps should be performed:

1) Finding the closest-point projection of a given slave point onto the master surface. This is done by formulation of a function that describes the distance between a given slave point at location $\mathbf{x}^2$ and a point positioned on the master surface at $\mathbf{x}^1 = \hat{\mathbf{x}}^1(\boldsymbol{\xi})$ :

   $$d\left(\mathbf{x}^2, \boldsymbol{\xi}\right) = \left\| \mathbf{x}^2 - \hat{\mathbf{x}}^1(\boldsymbol{\xi}) \right\| \tag{2.3.1}$$

   where $\boldsymbol{\xi}$ is the convective coordinate of the master surface.
   Assuming that the master surface is convex, one can relate the slave points to

master surface points via the minimum distance (closest point projection) problem:

$$\overline{\boldsymbol{\xi}}\left(\mathbf{x}^2\right) = \arg_{\boldsymbol{\xi}\in D}\ \min\ d\left(\mathbf{x}^2, \boldsymbol{\xi}\right) \tag{2.3.2}$$

where D is the domain of definition of the convective coordinates. The necessary condition for the minimum distance is

$$\frac{d}{d\xi^\alpha} d\left(\mathbf{x}^2, \boldsymbol{\xi}\right) = \frac{\hat{\mathbf{x}}^1\left(\boldsymbol{\xi}\right)}{\left\|\mathbf{x}^2 - \hat{\mathbf{x}}^1\left(\boldsymbol{\xi}\right)\right\|} \cdot \hat{\mathbf{x}}^1_{,\alpha}\left(\boldsymbol{\xi}\right) = 0 \tag{2.3.3}$$

with $\alpha$= 1,2.
Solution of equation (2.3.3) requires orthogonality between the distance vector $\left[\mathbf{x}^2 - \hat{\mathbf{x}}^1\left(\boldsymbol{\xi}\right)\right]$ and the tangent vectors $\overline{\boldsymbol{a}}_\alpha = \hat{\mathbf{x}}^1_{,\alpha}\left(\boldsymbol{\xi}\right)$ at the projection point, which in turn can be interpreted as the normal projection of a given slave point to the master surface. The orthogonality condition is expressed as:

$$\left(\mathbf{x}^2 - \overline{\mathbf{x}}^1\right) \cdot \overline{\boldsymbol{a}}_\alpha = 0 \tag{2.3.4}$$

It should be noted that quantities related to the master surface and calculated at the projection point will be denoted with a bar above the symbol.

Since the rubber tire undergoes large deformations, while the contacting surface remains nearly undeformed, the road surface can be considered as rigid. This assumption simplifies the contact detection since the rigid master surface of the road is fixed in space and can be described by an analytical function. The rigid master surface is defined as:

$$z\left(x, y\right) = \Delta \cdot \sin\left(qx\right) \cdot \sin\left(qy\right) \tag{2.3.5}$$

In this case, the tangential vectors $\overline{\boldsymbol{a}}_1$, $\overline{\boldsymbol{a}}_2$ and the normal vector to the rigid master surface at the projection point $\overline{\boldsymbol{n}}$ can be calculated analytically for each point as:

$$\overline{\boldsymbol{a}}_1 = \begin{bmatrix} 1 \\ 0 \\ z_{,x} \end{bmatrix} \qquad \overline{\boldsymbol{a}}_2 = \begin{bmatrix} 0 \\ 1 \\ z_{,y} \end{bmatrix} \tag{2.3.6}$$

$$\overline{\boldsymbol{n}} = \frac{\overline{\boldsymbol{a}}_1 \times \overline{\boldsymbol{a}}_2}{\left\|\overline{\boldsymbol{a}}_1 \times \overline{\boldsymbol{a}}_2\right\|} = \frac{1}{\sqrt{z_{,x}^2 + z_{,y}^2 + 1}} \begin{bmatrix} -z_{,x} \\ -z_{,y} \\ 1 \end{bmatrix} \tag{2.3.7}$$

For the 2D case in x-z plane, one must substitute $z_{,y} = 0$. Thus

$$\overline{\boldsymbol{a}}_1 = \begin{bmatrix} 1 \\ z_{,x} \end{bmatrix} \qquad \overline{\boldsymbol{n}} = \frac{1}{\sqrt{z_{,x}^2 + 1}} \begin{bmatrix} -z_{,x} \\ 1 \end{bmatrix} \tag{2.3.8}$$

2) Calculating the normal gap: The normal gap between the two bodies $g_N$, which is negative when penetration of the bodies occurs, is defined as:

$$g_N = \left(\mathbf{x}^2 - \overline{\mathbf{x}}^1\right) \cdot \overline{\boldsymbol{n}} \tag{2.3.9}$$

The virtual variation of the normal gap, which is needed for the weak form of the contact problem, is expressed as [18, 121]

$$\delta g_N = \left(\delta\mathbf{x}^2 - \delta\overline{\mathbf{x}}^1\right) \cdot \overline{\boldsymbol{n}} \tag{2.3.10}$$

### Kinematics in tangential direction

The tangential gap describes the movement of a slave point tangential to the master surface. In the tangential direction, one should distinguish between two cases:

1) The stick state, in which two bodies stick together and no relative movement in the tangential direction occurs between them, i.e. the gap is zero.

   The mathematical condition for stick is derived from the fact that, if a slave point and its master projection undergo no relative motion in the tangential direction, the convective coordinates of the normal projection point do not change with time. It is formulated as:

   $$\dot{\bar{\xi}}^{\alpha} = \frac{\partial \bar{\xi}^{\alpha}}{\partial t} = 0 \tag{2.3.11}$$

   This condition is formulated within a large deformation framework in the current configuration. It imposes a nonlinear constraint equation on the motion in the contact interface.

2) The slip (or sliding) state, where the tangential force exchanged between the slave point and its projection point onto the master surface leads to the relative motion of the two points in the tangential direction along the contact interface.

   In order to describe sliding, the current geometry is insufficient and it is important to set up an incremental expression and to calculate its evolution with time. The incremental relationship of the tangential relative displacement vector can be defined along the convective coordinates of the master surface as:

   $$d\boldsymbol{g_T} = \bar{\boldsymbol{a}}_{\alpha} d\bar{\xi}^{\alpha} = \bar{\mathbf{x}}^{1}_{,\alpha} d\bar{\xi}^{\alpha} = \bar{\mathbf{x}}^{1}_{,\alpha} \dot{\bar{\xi}}^{\alpha} dt \tag{2.3.12}$$

   The incremental length of the sliding path is calculated as $dg_T = \|d\boldsymbol{g_T}\|$. Its finite length between time $t_0$ and t is calculated as

   $$g_T = \int_{t_0}^{t} \left\| \bar{\mathbf{x}}^{1}_{,\alpha} \dot{\bar{\xi}}^{\alpha} \right\| dt \tag{2.3.13}$$

   For the special case of a 2D rigid master surface, equation (2.3.13) is written as

   $$g_T = \int_{t_0}^{t} \sqrt{\dot{x}^2 \left(1 + z_{,x}^2\right)}\, dt \tag{2.3.14}$$

In order to calculate the derivative $\dot{\bar{\xi}}^{\alpha}$ in equation (2.3.13), one should carry out the material time derivative of equation (2.3.4), which gives

$$\left(\mathbf{v}^2 - \bar{\mathbf{v}}^1 - \bar{\boldsymbol{a}}_{,\beta} \dot{\bar{\xi}}^{\beta}\right) \cdot \bar{\boldsymbol{a}}_{\alpha} + \left(\mathbf{x}^2 - \bar{\mathbf{x}}^1\right) \cdot \left(\bar{\mathbf{v}}^{1}_{,\alpha} + \bar{\mathbf{x}}^{1}_{,\alpha\beta} \dot{\bar{\xi}}^{\beta}\right) = 0 \tag{2.3.15}$$

where $\mathbf{v}^\alpha = \frac{\partial \mathbf{x}^\alpha}{\partial t}$. Solving for $\dot{\overline{\xi}}^\alpha$ gives

$$\dot{\overline{\xi}}^\alpha = \bar{H}^{\alpha\beta} \left[ \left( \mathbf{v}^2 - \overline{\mathbf{v}}^1 \right) \cdot \overline{\boldsymbol{a}}_\beta + g_N \overline{\boldsymbol{n}} \cdot \overline{\mathbf{v}}^1_{,\beta} \right] \tag{2.3.16}$$

with

$$\bar{H}^{\alpha\beta} = H^{-1}_{\alpha\beta} \qquad H_{\alpha\beta} = \overline{a}_{\alpha\beta} - g_N \overline{k}_{\alpha\beta} \tag{2.3.17}$$

In case of contact $g_N = 0$, so that the above formulation can be simplified as

$$\dot{\overline{\xi}}^\alpha = \bar{a}^{\alpha\beta} \left( \mathbf{v}^2 - \overline{\mathbf{v}}^1 \right) \cdot \overline{\boldsymbol{a}}_\beta = \left( \mathbf{v}^2 - \overline{\mathbf{v}}^1 \right) \cdot \overline{\boldsymbol{a}}^\alpha \tag{2.3.18}$$

Finally, the tangential relative velocity $\dot{\boldsymbol{g}}_T$, which is an objective rate measure of the tangential relative displacement $\boldsymbol{g}_{\boldsymbol{T}}$, is derived from equation (2.3.12) as

$$\dot{\boldsymbol{g}}_T := \overline{\mathbf{x}}^1_{,\alpha} \dot{\overline{\xi}}^\alpha \tag{2.3.19}$$

The virtual variation of the tangential slip can be calculated similarly to its increment in equation (2.3.12)

$$\delta \boldsymbol{g}_{\boldsymbol{T}} = \overline{\boldsymbol{a}}_\alpha \delta \overline{\xi}^\alpha \tag{2.3.20}$$

$\delta \overline{\xi}^\alpha$ can be evaluated directly from equation (2.3.16)

$$\delta \overline{\xi}^\alpha = \bar{H}^{\alpha\beta} \left[ \left( \delta \mathbf{x}^2 - \delta \overline{\mathbf{x}}^1 \right) \cdot \overline{\boldsymbol{a}}_\beta + g_N \overline{\boldsymbol{n}} \cdot \delta \overline{\mathbf{x}}^1_{,\beta} \right] \tag{2.3.21}$$

In case of contact $g_N = 0$ and the aforementioned equation is written as

$$\delta \overline{\xi}^\alpha = \bar{a}^{\alpha\beta} \left( \delta \mathbf{x}^2 - \delta \overline{\mathbf{x}}^1 \right) \cdot \overline{\boldsymbol{a}}_\beta = \left( \delta \mathbf{x}^2 - \delta \overline{\mathbf{x}}^1 \right) \cdot \overline{\boldsymbol{a}}^\alpha \tag{2.3.22}$$

### 2.3.2 Balance equations for contact

Contact takes place when $g_N = 0$, where a contact traction vector is exchanged between the slave and the master bodies at the contacting points $\mathbf{x}^2$ and $\overline{\mathbf{x}}^1$. This Cauchy traction vector acts on both surfaces obeying the action-reaction principle: $\boldsymbol{t}^1 \left( \overline{\boldsymbol{\xi}} \right) = -\boldsymbol{t}^2$ (acting on the same elementary area $da$ on both surfaces) and can be decomposed along the directions of the normal and the tangent vectors at the master projection point as follows:

$$\boldsymbol{t}^1 = \boldsymbol{t}_N + \boldsymbol{t}_T \qquad \boldsymbol{t}_N = t_N \bar{\boldsymbol{n}} \qquad \boldsymbol{t}_T = t^\alpha_T \, \bar{\boldsymbol{a}}_\alpha \, = \, t_{T\alpha} \bar{\boldsymbol{a}}^\alpha \tag{2.3.23}$$

with

$$t_N = \boldsymbol{t}^1 \cdot \bar{\boldsymbol{n}} \qquad t^\alpha_T = \boldsymbol{t}^1 \cdot \bar{\boldsymbol{a}}^\alpha \qquad t_{T\alpha} = \boldsymbol{t}^1 \cdot \bar{\boldsymbol{a}}_\alpha \tag{2.3.24}$$

Note that $\boldsymbol{t}_T$, besides along the directions of the tangent vector $\bar{\boldsymbol{a}}_\alpha$ (covariant basis), has been equivalently expressed in the contravariant basis $\bar{\boldsymbol{a}}^\alpha$ at the projection point. The normal component $t_N < 0$ corresponds to compression in the normal direction (in the standard case where no adhesive stresses are allowed at the contact interface), whereas the tangential components (expressed in the covariant or contravariant bases $t^\alpha_T$ or $t_{T\alpha}$, respectively) can have arbitrary sign but vanish in the case of frictionless contact.

In a Lagrangian description, the decomposition in equation (2.3.23) can be written as

$$\boldsymbol{T}^1 = \boldsymbol{T}_N + \boldsymbol{T}_T \qquad \boldsymbol{T}_N = T_N \bar{\boldsymbol{n}} \qquad \boldsymbol{T}_T = T_T^{\alpha}\, \bar{\boldsymbol{a}}_{\alpha} \;=\; T_{T\alpha} \bar{\boldsymbol{a}}^{\alpha} \tag{2.3.25}$$

where

$$T_N = \boldsymbol{T}^1 \cdot \bar{\boldsymbol{n}} \qquad T_T^{\alpha} = \boldsymbol{T}^1 \cdot \bar{\boldsymbol{a}}^{\alpha} \qquad T_{T\alpha} = \boldsymbol{T}^1 \cdot \bar{\boldsymbol{a}}_{\alpha} \tag{2.3.26}$$

are the normal, contravariant, and covariant components of the Piola contact traction vector $\boldsymbol{T}^1$ on the master surface.

### 2.3.3 Contact constraints

In order to describe the physical behavior in the contact zone, it is crucial to extend the description of the kinematic relations by specifying interfacial contact constraints. If contact is detected, the active contact zones should satisfy geometrical constraints in normal and tangential directions.

#### Contact constraints in normal direction

The geometrical constraint in the normal direction is the non-penetration condition, which does not account for any physical interaction mechanism at the contact surface.

Considering adhesionless unilateral contact, the relationship between the normal contact pressure and the normal gap is deduced from the following mathematical conditions for the contact interface

- penetration is not allowed: $g_N \geq 0$;
- contact normal stresses can only be compressive: $t_N \leq 0$;
- the contact normal stress vanishes when the gap is open, and is negative when the gap is closed: if $g_N > 0$, then $t_N = 0$; if $g_N = 0$, then $t_N \leq 0$.

The aforementioned relations are summarized by the following statements:

$$g_N \geq 0 \qquad t_N \leq 0 \qquad t_N g_N = 0 \qquad \text{on} \quad \gamma_c \tag{2.3.27}$$

which are called Hertz-Signorini-Moreau conditions in the context of contact mechanics and correspond to the Karush-Kuhn-Tucker (KKT) complementarity conditions used in constrained optimization theories. These inequalities are expressed in the current configuration, similar inequalities can be formulated in the reference configuration by replacing $t_N$ with $T_N$. These conditions lead to a non-smooth relationship between the contact pressure and the normal gap, see Figure 2.3.
The extension of these inequalities if adhesion effects are included is treated in [80] or [118].

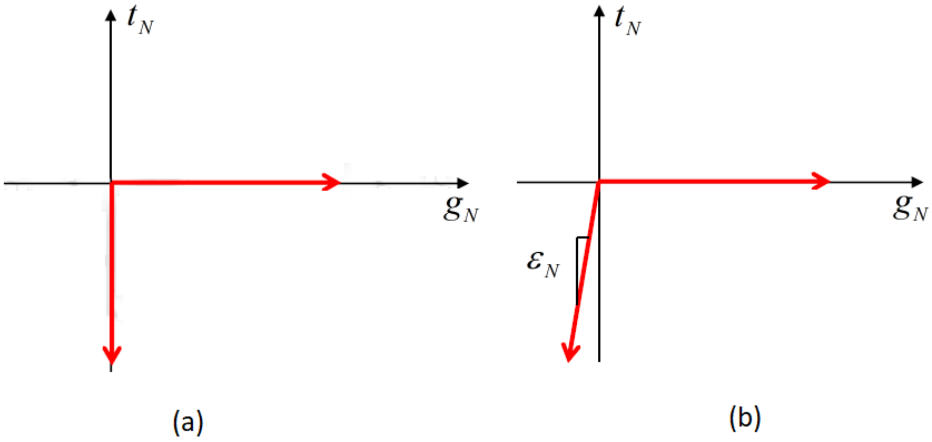

**Figure 2.3:** Contact constraint in the normal direction. (a) using geometric enforcement of the non-penetration constraint (b) using the penalty method.

### Contact constraints in tangential direction

In the tangential direction, a stick condition can be enforced either as a geometric constraint or as a constitutive law relating the tangential traction component to the tangential relative displacement between the bodies. Coulomb's law is still widely applied to solve contact problems. According to Coulomb's law, only a certain amount of tangential stress can be transmitted. Up to this stress level, the bodies stick together without any relative tangential velocity. In other words, any point in contact undergoes slip or stick conditions depending on the magnitude of the tangential traction vector $\boldsymbol{t}_T$. Stick is expressed by the following conditions:

$$\|\boldsymbol{t}_T\| < \mu\,|t_N| \qquad \dot{\boldsymbol{g}}_{\boldsymbol{T}} = \boldsymbol{0} \tag{2.3.28}$$

where $\mu$ is the static friction coefficient.

In sliding conditions, a constitutive law for friction is needed. It is expressed in form of an evolution equation that may involve several parameters such as relative tangential velocity, contact pressure, total slip distance and temperature. The mathematical condition for slip according to Coulomb's law is given by

$$\boldsymbol{t}_T = \mu\,|t_N|\,\frac{\dot{\boldsymbol{g}}_T}{\|\dot{\boldsymbol{g}}_T\|} \qquad \dot{\boldsymbol{g}}_T \neq \boldsymbol{0} \tag{2.3.29}$$

Equations (2.3.28) and (2.3.29) are illustrated in Figure 2.4(a).
The transition from stick to slip is described by the stick-slip condition, which is expressed for Coulomb's friction law as

$$\Phi\left(\boldsymbol{t}_T, t_N\right) = \|\boldsymbol{t}_T\| - \mu\,|t_N| \leq 0 \tag{2.3.30}$$

The evolution equation of the frictional slip can be obtained from the maximum dissipation principle as

$$\dot{\boldsymbol{g}}_T = \dot{\gamma}\frac{\partial\Phi}{\partial\boldsymbol{t}_T} = \dot{\gamma}\frac{\boldsymbol{t}_T}{\|\boldsymbol{t}_T\|} \tag{2.3.31}$$

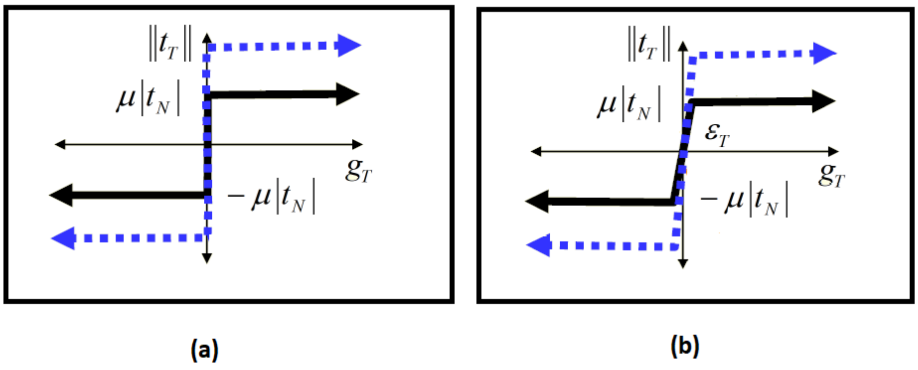

**Figure 2.4:** Contact constraint in the tangential direction. (a) using geometric enforcement of the stick constraint (b) using the penalty method. Black line refers to Coulomb's law and the blue dashed line refers to a friction law dependent on contact pressure.

with $\|\boldsymbol{t}_T\| = \sqrt{t_{T\alpha}\bar{a}^{\alpha\beta}t_{T\beta}}$. $\dot{\gamma}$ is the frictional slip parameter. It is related directly to the magnitude of the slip $\|\dot{\boldsymbol{g}}_T\| = |\dot{\gamma}|$.

Similar to equation (2.3.27), the loading-unloading conditions can be formulated in KKT form as

$$\dot{\gamma} \geq 0, \qquad \Phi \leq 0, \qquad \dot{\gamma}\,\Phi = 0 \qquad \text{on} \quad \gamma_c \tag{2.3.32}$$

which enable the determination of the frictional slip parameter $\dot{\gamma}$.

## 2.3.4 Boundary value problem and variational form

A contact problem can be considered as a classical mechanical problem with additional inequality constraints stemming from the contact conditions. Its formulation in strong and variational forms is addressed as follows.

### Strong form of boundary value problem

The local quasistatic momentum balance equations for two contacting bodies in Eulerian description read

$$\operatorname{div}\left(\boldsymbol{\sigma}^i\right) + \rho\,\bar{\boldsymbol{b}}^i = \boldsymbol{0} \qquad \text{in} \qquad \Omega^i \tag{2.3.33}$$

where $\boldsymbol{\sigma}^i$ are the Cauchy tensors and $\bar{\boldsymbol{b}}^i$ are the body forces in the current configuration. Dirichlet and Neumann boundary conditions in Eulerian description read

$$\begin{aligned} \boldsymbol{u}^i &= \bar{\boldsymbol{u}}^i \quad \text{on} \quad \gamma_u^i\,, \\ \boldsymbol{\sigma}^i\boldsymbol{n}^i &= \bar{\boldsymbol{t}}^i \quad \text{on} \quad \gamma_t^i\,, \end{aligned} \tag{2.3.34}$$

with $\bar{\boldsymbol{u}}^i$ as prescribed displacements, $\boldsymbol{n}^i$ as surface outward unit normal vectors, and $\bar{\boldsymbol{t}}^i$ as prescribed tractions, with the latter two pertaining to the current configuration.

On the contact portions of the boundary, the contact constraints based on the purely geometric enforcement of the non-penetration condition in the normal direction as well as on Coulomb's friction law in the tangential direction are given by equations (2.3.27) and (2.3.32), respectively.

### Weak form of boundary value problem

In order to obtain the numerical solution with the FEM, one has to derive the weak form of contact equilibrium. The weak form of the balance of momentum for each body can be written in the Eulerian description as

$$\int_{\Omega^i} \boldsymbol{\sigma}^i : \operatorname{grad}^s \delta \boldsymbol{u}^i \, dv - \int_{\Omega^i} \bar{\boldsymbol{b}}^i \, \rho \, \delta \boldsymbol{u}^i \, dv - \int_{\gamma_t^i} \bar{\boldsymbol{t}}^i \, \delta \boldsymbol{u}^i \, da - \int_{\gamma_c^i} \boldsymbol{t}^i \cdot \delta \boldsymbol{u}^i \, da. \tag{2.3.35}$$

It should be noted that in equation (2.3.35), summation over $i$ is not implemented. The last term in the equation (2.3.35) represents the virtual work due to the contact tractions on the body $\Omega^i$.

The weak form of equilibrium G is divided into a contribution associated with the internal and external virtual work on the two bodies (b) and a contact contribution to the total virtual work associated with the active constraint set (c):

$$G = G_b + G_c = 0. \tag{2.3.36}$$

with

$$G_b = \sum_{i=1}^{2} G_b^i \tag{2.3.37}$$

$$G_b^i = \int_{\Omega^i} \boldsymbol{\sigma}^i : \operatorname{grad}^s \delta \boldsymbol{u}^i \, dv - \int_{\Omega^i} \bar{\boldsymbol{b}}^i \, \rho \, \delta \boldsymbol{u}^i \, dv - \int_{\gamma_t^i} \bar{\boldsymbol{t}}^i \, \delta \boldsymbol{u}^i \, da. \tag{2.3.38}$$

$$G_c = -\sum_{i=1}^{2} \int_{\gamma_c^i} \boldsymbol{t}^i \cdot \delta \boldsymbol{u}^i \, da \tag{2.3.39}$$

The equation (2.3.39) can be simplified by recalling that $\gamma_c^1 = \gamma_c^2 = \gamma_c$ and $\boldsymbol{t}^1 = -\boldsymbol{t}^2$ if considering, for each point on the slave surface, its correspoding projection point on the master surface defined through the kinematics in Section 2.3.1. Therefore

$$\begin{aligned} G_c &= -\textstyle\int_{\gamma_c^1} \boldsymbol{t}^1 \cdot \delta \boldsymbol{u}^1 \, da - \int_{\gamma_c^2} \boldsymbol{t}^2 \cdot \delta \boldsymbol{u}^2 \, da \\ &= \textstyle\int_{\gamma_c} \boldsymbol{t}^1 \cdot (\delta \boldsymbol{u}^2 - \delta \bar{\boldsymbol{u}}^1) \, da \end{aligned} \tag{2.3.40}$$

where the bar on $\delta \bar{\boldsymbol{u}}^1$ refers to the projection point. Introducing the resolution of $\boldsymbol{t}^1$ along normal and tangential directions in equation (2.3.23), noting that $\delta \mathbf{x}^i = \delta \mathbf{u}^i$, and recalling equations (2.3.10), (2.3.22), and (2.3.20) further leads to

$$
\begin{aligned}
G_c &= \int\limits_{\gamma_c} (t_N \overline{\boldsymbol{n}} + t_{T\alpha} \overline{\boldsymbol{a}}^{\alpha}) \cdot \left(\delta \boldsymbol{u}^2 - \delta \overline{\boldsymbol{u}}^1\right) \, da \\
&= \int\limits_{\gamma_c} \left[ t_N \delta g_n + t_{T\alpha} \delta \overline{\xi}^{\alpha} \right] da \\
&= \int\limits_{\gamma_c} \left[ t_N \delta g_n + \boldsymbol{t}_T \cdot \delta \boldsymbol{g}_T \right] da
\end{aligned}
\tag{2.3.41}
$$

Equivalently, one can write the contact contriubtion to the weak form of equilibrium in the Lagrangian description as

$$
\begin{aligned}
G_c &= \int\limits_{\Gamma_c} \boldsymbol{T}^1 \cdot \left(\delta \boldsymbol{u}^2 - \delta \overline{\boldsymbol{u}}^1\right) \, dA \\
&= \int\limits_{\Gamma_c} \left[ T_N \delta g_n + T_{T\alpha} \delta \overline{\xi}^{\alpha} \right] dA \\
&= \int\limits_{\Gamma_c} \left[ T_N \delta g_n + \boldsymbol{T}_T \cdot \delta \boldsymbol{g}_T \right] dA
\end{aligned}
\tag{2.3.42}
$$

It should be noted that equation (2.3.42) requires the selection of the reference contact surface on which the integration is performed, which is carried out mostly on the slave surface.

It should be noted also that calculation of contact integral in the reference configuration of equation (2.3.42) is often preferred, since it simplifies the linearization required for the iterative solution of the nonlinear problem [18]. The contact contribution to the weak form $G_c$ is evalutated differently depending on the selected method for the enforcement of the contact constraints, which will be addressed in Subsection 2.3.5.

### Incremental minimization problem

The contact mechanical problem can be formulated as a constrained incremental minimization problem of the total potential energy function $\Pi_b$ of body, subject to the contact constraints in the normal and tangential directions, that is

$$
\Pi_b \quad \rightarrow \quad \min \qquad \text{subject to (2.3.27) and (2.3.32) on } \gamma_c \tag{2.3.43}
$$

It is assumed here that the contact constitutive laws correspond to purely geometric enforcement of the conditions in the normal direction and to Coulomb's frictional behavior in the tangential direction.

The contact problem can be expressed within the framework of constrained optimization theories, which lead to the conversion of the constrained minimization problem in equation (2.3.43) into the following problem:

$$
\Pi_b + \Pi_c \quad \rightarrow \quad \text{stat} \tag{2.3.44}
$$

where $\Pi_c$ is the contact contribution to the incremental energy functional, which can be taken as a variational representation of the contact kinematics constraints.

The specific formulation of $\Pi_c$ and the corresponding solution of the equation (2.3.44) depend on the selected solution strategy and are the subject of Subsection 2.3.5. The necessary conditions for the problem (2.3.44)

$$\delta\Pi_b + \delta\Pi_c = 0 \tag{2.3.45}$$

will lead to the variational formulation (2.3.36), so that

$$G_c = \delta\Pi_c \tag{2.3.46}$$

### 2.3.5 Methods for enforcement of contact constraints

Several techniques can be applied to enforce the contact constraints into the variational formulation and correspond to different forms of $\Pi_c$ . The most widespread methods are Lagrangian multiplier, penalty and augmented Lagrange multiplier methods. They will be outlined in the following.

All these methods should be coupled with an active set strategy, which is used to identify the portion of the boundary in active contact and to track its evolution with time.

**Lagrange multiplier method**

In this formulation, Lagrange multipliers are used to add constraints to the weak form of the solids in contact. The contact contribution in (2.3.44) is formulated as

$$\Pi_c^{LM,st}(\boldsymbol{u},\boldsymbol{\lambda}) = \int\limits_{\Gamma_c} (\lambda_N g_N + \boldsymbol{\lambda}_T \cdot \boldsymbol{g}_T)\, dA \tag{2.3.47}$$

where $\lambda_N$, $\boldsymbol{\lambda_T}$ are the components of the Lagrange multiplier vector $\boldsymbol{\lambda}$ in the normal and the tangential directions, respectively. The superscript ”st” refers to stick conditions in the tangential direction.

The problem (2.3.44) constitutes in this case an unconstrained saddle-point problem, where the solution corresponds to the minimum of $\Pi_c^{LM,st}$ with respect to $\boldsymbol{u}$ and to the maximum with respect to $\boldsymbol{\lambda}$. The necessary condition for the saddle-point problem takes the form of (2.3.45). Since the Lagrange multipliers are additional unknowns, the variation of $\Pi_c^{LM}$ should be computed with respect to $\boldsymbol{g}$ and $\boldsymbol{\lambda}$, which is written for the stick case as

$$\delta\Pi_c^{LM,st} = G_c^{LM,st} = \int\limits_{\Gamma_c} (\lambda_N \delta g_N + \boldsymbol{\lambda_T} \cdot \delta\boldsymbol{g}_T)\, dA + \int\limits_{\Gamma_c} (\delta\lambda_N g_N + \delta\boldsymbol{\lambda_T} \cdot \boldsymbol{g}_T)\, dA \tag{2.3.48}$$

The first integral represents the virtual work of the Lagrange multipliers for the variation of the gap functions in normal and tangential directions, while the second integral stems from the enforcement of the kinematic constraints and includes the virtual variations of the Lagrange multipliers $\delta\boldsymbol{\lambda}$. On comparing the first integral written in equation (2.3.48) with the one of equation (2.3.42), it can be seen that the normal and tangential Lagrange multipliers correspond to the unknown normal and tangential contact tractions ($\lambda_N{=}T_N$ and $\boldsymbol{\lambda}_{\boldsymbol{T}} = \boldsymbol{T}_T$).

For the sliding case, the tangential traction can be determined from equation (2.3.29). The variation of $\Pi_c^{LM}$ should be formulated to fulfill the condition described in equation (2.3.31) as:

$$\delta\Pi_c^{LM,sl} = G_c^{LM,sl} = \int\limits_{\Gamma_c} \left(\lambda_N \delta g_N + \boldsymbol{\lambda}_{\boldsymbol{T}} \cdot \delta \boldsymbol{g}_T\right) dA + \int\limits_{\Gamma_c} \left[\delta\lambda_N g_N + \left(\dot{\boldsymbol{g}}_T - \dot{\gamma}\frac{\boldsymbol{\lambda}_T}{\|\boldsymbol{\lambda}_T\|}\right) \cdot \boldsymbol{g}_T\right] dA \tag{2.3.49}$$

In the aforementioned equation, the sliding rate $\dot{\gamma}$ is an additional unknown at the contact node.

The main advantage of the Lagrange multiplier method is that it leads to an exact enforcement of the contact constraints. However, the method has the major drawback that it introduces additional unknowns (Lagrange multipliers). Another disadvantage of the method is that it leads to zero values on the matrix diagonal and thus sometimes requires special solvers. This leads in turn to an increased computational cost.

### Penalty method

In this method, a penalty term is used to enforce the contact constraints, so that the deviation from the exact enforcement is penalized with a functional term. The contact contribution $\Pi_c$ in (2.3.44) is formulated as

$$\Pi_c^{P,st}\left(\boldsymbol{u}\right) = \frac{1}{2}\int\limits_{\Gamma_c} \left[\varepsilon_N g_N^2 + \varepsilon_T \boldsymbol{g}_T \cdot \boldsymbol{g}_T\right] dA, \quad \varepsilon_N, \varepsilon_T > 0 \tag{2.3.50}$$

where $\varepsilon_N > 0$ and $\varepsilon_T > 0$ are the penalty parameters for normal and tangential stick contact, respectively.

The variation of equation (2.3.50) is written as

$$\delta\Pi_c^{P,st} = G_c^{P,st} = \int\limits_{\Gamma_c} \left[\varepsilon_N g_N \delta g_N + \varepsilon_T \boldsymbol{g}_T \cdot \delta\boldsymbol{g}_T\right] dA \tag{2.3.51}$$

One can notice from the comparison of this integral with the one of equation (2.3.42) that the normal and the tangential contact tractions are approximated by the penalty method as $T_N = \varepsilon_N g_N$ and $\boldsymbol{T}_T = \varepsilon_T \boldsymbol{g}_T$.

The physical meaning of the penalty method is to insert linear springs at the contact zone with a predefined spring stiffness $\varepsilon_N/\varepsilon_T$ in order to approximate the constraint enforcement avoiding additional unknowns as in Lagrange multiplier method.

In case of slip conditions, the term $\varepsilon_T \boldsymbol{g}_T$ is replaced by the term $\tilde{\boldsymbol{T}}_T$ as follows

$$\delta\Pi_c^{P,sl} = G_c^{P,sl} = \int\limits_{\Gamma_c} \left[\varepsilon_N g_N \delta g_N + \tilde{\boldsymbol{T}}_T \cdot \delta \boldsymbol{g}_T\right] dA \tag{2.3.52}$$

The penalty method has the advantage that it does not require the introduction of additional unknowns into the problem and thus it yields a reduced computational cost. However, the penalty method has a number of disadvantages. The first disadvantage is that it leads to an approximate enforcement of the contact constraints. This means that the impenetrability condition is not fulfilled exactly. Another drawback of the method is that the penalty parameters must be selected carefully. On one hand, an exact enforcement of the contact constrains is obtained in the limit as the spring stiffness tends to infinity. However, such limit would lead to ill-conditioning of the tangent stiffness matrix. On the other hand, selection of a too small penalty parameter results in a large penetration of the bodies. Therefore, the penalty stiffness must be chosen taking into account the material properties of the contacting bodies.

### Augmented Lagrange multiplier method

The augmented Lagrange multiplier method is a combination of the penalty and the Lagrange multiplier methods, where the Lagrange multipliers are not presesnt as additional unknowns but approximated through an iterative procedure known as the Uzawa algorithm.

In the augmented Lagrange multiplier method, the contact contribution $\Pi_c$ in (2.3.44) is formulated as

$$\Pi_c^{AL}(\boldsymbol{u}) = \int\limits_{\Gamma_c} \left[\ \left(\bar{\lambda}_N + \frac{\varepsilon}{2} g_N\right) g_N + \left(\bar{\boldsymbol{\lambda}}_T + \frac{\varepsilon}{2}\boldsymbol{g}_T\right) \cdot \boldsymbol{g}_T\right] dA \tag{2.3.53}$$

where $\varepsilon > 0$ is a penalty parameter. In this approach, the Lagrangian $\Pi_c^{AL}$ (Eq. (2.3.53)) is minimized at the beginning with respect to displacements at a fixed value of Lagrange multipliers. The variation of equation (2.3.53) is written as

$$\delta\Pi_c^{AL}(\boldsymbol{u}) = G_c^{AL} = \int\limits_{\Gamma_c} \left[\ \left(\bar{\lambda}_N + \varepsilon g_N\right) \delta g_N + \left(\bar{\boldsymbol{\lambda}}_T + \varepsilon \boldsymbol{g}_T\right) \cdot \delta \boldsymbol{g}_T\right] dA \tag{2.3.54}$$

Then, a first order update of the Lagrange multipliers is applied according to Uzawa algorithm, which will be explained in Subsection 2.3.6.

The augmented Lagrange multiplier methods has several advantages over the other methods. It enforces the contact constraints with a prescribed accuracy without additional degrees of freedom as in the Lagrange multiplier method. As opposed to the penalty method, the contact constraint in the augmented Lagrange multiplier method is enforced regardless of the value of the penalty parameter, which can be then kept low in order to improve the iterative convergence behavior. The only drawback of this method is that an additional augmentation loop is needed.

The augmented Lagrange multiplier method will be adopted in this work.

### 2.3.6 Linearization and Uzawa algorithm

In order to solve a discrete contact problem with the Uzawa algorithm, one should start from the variational formulation (2.3.36), with $G_b = \delta \boldsymbol{u}^T \left[\boldsymbol{R}_{\text{int}}\left(\boldsymbol{u}\right) - \boldsymbol{P}\right]$ and $G_c^{AL} = \delta \boldsymbol{u}^T \boldsymbol{C}^T\left(\boldsymbol{u}\right) \overline{\boldsymbol{\Lambda}}$. It will be written in residual form as

$$G_b + G_c^{AL} \cong \delta \boldsymbol{u}^T \left[\boldsymbol{R}_{\text{int}}\left(\boldsymbol{u}\right) + \boldsymbol{C}^T\left(\boldsymbol{u}\right) \overline{\boldsymbol{\Lambda}} - \boldsymbol{P}\right] = \delta \boldsymbol{u}^T \boldsymbol{R}^{AL} \tag{2.3.55}$$

with

$$\boldsymbol{R}^{AL} = \boldsymbol{R}_{\text{int}}\left(\boldsymbol{u}\right) + \boldsymbol{C}^T\left(\boldsymbol{u}\right) \overline{\boldsymbol{\Lambda}} - \boldsymbol{P} \tag{2.3.56}$$

as the residual vector. The Lagrange multipliers are considered as constants and are indicated as $\overline{\boldsymbol{\Lambda}}$.

$$\overline{\boldsymbol{\Lambda}} = \begin{bmatrix} \overline{\boldsymbol{\lambda}}_1 \\ \vdots \\ \overline{\boldsymbol{\lambda}}_n \end{bmatrix} \tag{2.3.57}$$

and

$$\boldsymbol{C}\left(\boldsymbol{u}\right) = \frac{\partial \boldsymbol{G}\left(\boldsymbol{u}\right)}{\partial \boldsymbol{u}} \tag{2.3.58}$$

where $\boldsymbol{G}$ is a vector containing nodal gaps in the normal direction and tangential gaps of the nodes in stick conditions. Linearization leads to

$$\Delta\left(G_b + G_c^{AL}\right) \cong \delta \boldsymbol{u}^T \left[\boldsymbol{K}_{\text{int}}\left(u\right) + \boldsymbol{K}_c^{AL}\left(\boldsymbol{u}, \overline{\boldsymbol{\Lambda}}\right)\right] \Delta \boldsymbol{u} = \delta \boldsymbol{u}^T \boldsymbol{K}^{AL}\left(\boldsymbol{u}, \overline{\boldsymbol{\Lambda}}\right) \Delta \boldsymbol{u} \tag{2.3.59}$$

where $\boldsymbol{K}_{\text{int}}\left(\boldsymbol{u}\right)$ is the continuum contribution to the tangent stiffness matrix,

$$\boldsymbol{K}_{\text{int}}\left(\boldsymbol{u}\right) = \frac{\partial \boldsymbol{R}_{\text{int}}\left(\boldsymbol{u}\right)}{\partial \boldsymbol{u}} \tag{2.3.60}$$

and $\boldsymbol{K}_c^{AL}\left(\boldsymbol{u}, \overline{\boldsymbol{\Lambda}}\right)$ is the contact contribution to the tangent stiffness matrix

$$\boldsymbol{K}_c^{AL}\left(\boldsymbol{u}, \overline{\boldsymbol{\Lambda}}\right) = \frac{\partial \boldsymbol{C}^T\left(\boldsymbol{u}\right)}{\partial \boldsymbol{u}} \overline{\boldsymbol{\Lambda}} \tag{2.3.61}$$

and

$$\boldsymbol{K}^{AL}\left(\boldsymbol{u}, \overline{\boldsymbol{\Lambda}}\right) = \boldsymbol{K}_{\text{int}}\left(\boldsymbol{u}\right) + \boldsymbol{K}_c^{AL}\left(\boldsymbol{u}, \overline{\boldsymbol{\Lambda}}\right) \tag{2.3.62}$$

is the global stiffness matrix. For a given value of $\overline{\boldsymbol{\Lambda}}$ corresponding to the J-th augmentation, $\overline{\boldsymbol{\Lambda}}^J$, the incremental update of the displacement solution is obtained from the following linearized equation:

$$\boldsymbol{K}^{AL}\left(\boldsymbol{u}^k, \overline{\boldsymbol{\Lambda}}^J\right) \Delta \boldsymbol{u}^k = -\boldsymbol{R}^{AL}\left(\boldsymbol{u}^k, \overline{\boldsymbol{\Lambda}}^J\right) \tag{2.3.63}$$

where k is the iteration step.
The iterative procedure is stopped when the norm of the residuals falls below a specified tolerance. Outside the Newton-Raphson loop, an augmentation loop is performed to update the Lagrange multipliers according to the following first-order update formula.

$$\overline{\boldsymbol{\Lambda}}^{J+1} = \overline{\boldsymbol{\Lambda}}^J + \varepsilon \boldsymbol{G}^{J+1} \tag{2.3.64}$$

where $\varepsilon > 0$ is a penalty-like parameter. This outer loop is carried out until the norm of $\boldsymbol{G}$, which quantifies the violation of contact constraints, becomes lower than a specified tolerance.

## 2.3.7 Contact discretization

Treatment of contact constraints within FEM includes two main aspects. The first aspect is the selection of the method to be used for the enforcement of the contact constraints, see Subsection 2.3.5. The second aspect is the choice of the way of the contact contribution to the weak form is expressed in the discretized form. This subsection focuses on this second aspect. In the following, a brief overview of two widely used contact discretization schemes within the FEM will be reviewed. They are:

- node-to-surface (NTS) discretization.
- surface-to-surface (STS) discretization.

Two important features of contact discretization schemes will be taken into account. They are the contact patch test performance, and the computational efficiency. The contact patch test was introduced by Taylor and Papadopoulos [102]. It ensures the decrease of the discretization error at the contacting surfaces upon mesh refinement.

### NTS discretization

The NTS discretization is an early discretization technique, which is suitable for large deformation contact problems and is still widely used in commercial finite element softwares. Early implementations are found in Hughes [35, 36] and Hallquist [28]. Further extensions to more general cases can be found in Bathe and Chaudhary [5], Hallquist [29], Wriggers and Simo [119], Benson and Hallquist [7], and Wriggers [120]. A comprehensive review of NTS discretization can be found in Zavarise and De Lorenzis [124].

NTS formulation has the advantage that it is simple and computationally inexpensive. However, it is unable to fulfill the contact patch test, which means that the contact pressures at the contact interface are calculated with a low degree of accuracy. This was explained by Zavarise and De Lorenzis [123] with the fact that the contact pressures are transferred from the slave to the master surface in form of concentrated forces at the slave nodes, which leads to violation of the balance of moments at the element level. This means that the calculated contact pressure values may be inaccurate. Furthermore, NTS is less stable in the context of large sliding distances and large deformations in the contact zone.

### STS discretization

Due to the drawbacks of NTS discretization, other formulations have been developed where the contact integral is no longer collocated at the slave nodes and contact constraints are enforced in integral manner. They are called STS approaches.

Simo [97] has first introduced integration over contact segments using a perturbed Lagrangian formulation, where a piecewise contant approximation of the contact pressure, discontinuous across contact segments, leads to the enforcement of the contact constraints in an average sense on each contact segment. Further STS approaches were proposed in Papadopoulos and Taylor [63] using quadtratic elements, in Papadopoulos and Taylor [64] using bilinear elements, and in Zavarise and Wriggers [125], El-Abbasi and Bathe [19] using 2D linear elements. These approaches employ an intermediate contact surface, over which contact quantities can be defined and discretized.

STS formulations pass the contact patch test thanks to the appropriate definition of the intermediate surface segments. STS discretization is more accurate than NTS and it is more suitable for large deformations since it reduces the likelihood of large localized penetrations and it also gives more accurate contact pressures at the contact interface. Therefore in order to ensure stable simulations, STS discretization is adopted in this work to simulate the large deformations and the contact interaction between rubber material and the rough counter surface. The major disadvantage of STS discretization is that it involves more nodes per constraint and therefore increases the computational cost.

It should be noted that the FE commercial software ABAQUS was used to model the contact interaction between rubber material and the rough counter surface. For implementation details in ABAQUS, see Section 4.3.4 in Chapter 4. In order to reduce the calculation time, the rough counter surface is modelled by linear one-dimensional rigid elements within ABAQUS.

ABAQUS documentation [99] does not provide the exact mathematical formulation of NTS or STS discretizations.

## 2.4 Fourier transform

Any domain having features at different length scales can be viewed from two different standpoints, spatial domain and frequency domain. The spatial domain shows the surface profile shape, while the frequency domain shows how much amplitude lies within each frequency band over a range of frequencies.

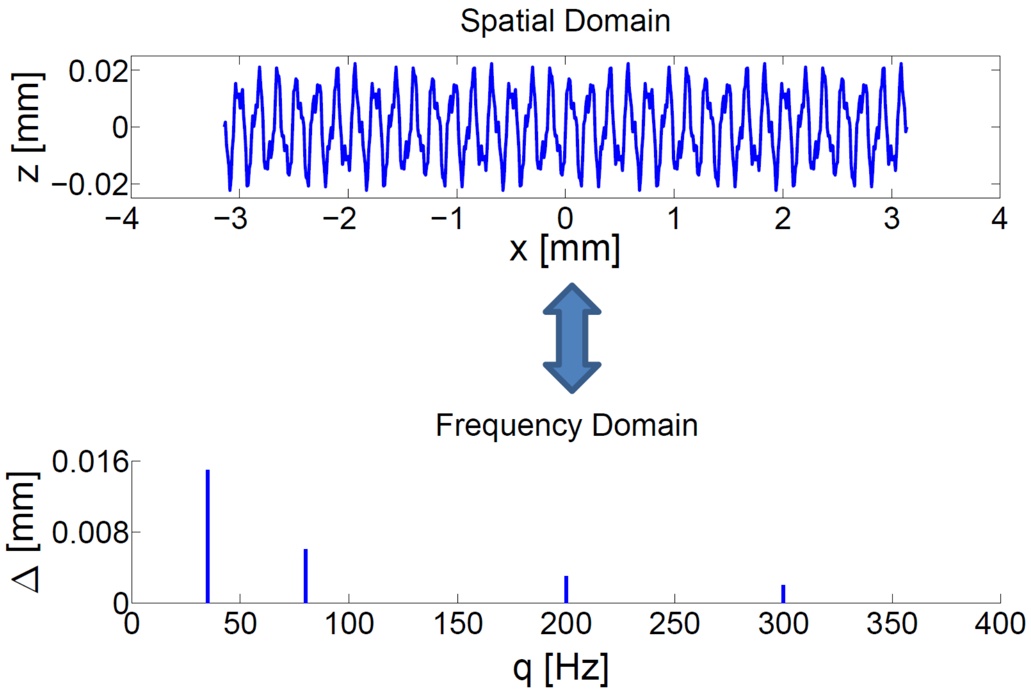

**Figure 2.5:** Fourier analysis principle.

Fourier transform is a method that converts the spatial profile surface into a spectral representation. It is defined as

$$\hat{f}\,(q) = \frac{1}{\sqrt{2\pi}} \int f\,(\mathrm{x})\; e^{-iq\mathrm{x}}\, d\mathrm{x} \tag{2.4.1}$$

The transform into the frequency domain permits to decompose the complex surface into simpler parts in order to facilitate analysis. Moreover, it converts the differential equations and convolution operations in the spatial domain into algebraic operations in the frequency domain.

The inverse Fourier transform of the function $\hat{f}\,(q)$ is

$$\tilde{f}\,(\mathrm{x}) = \frac{1}{\sqrt{2\pi}} \int \hat{f}\,(q)\; e^{iq\mathrm{x}}\, dq \tag{2.4.2}$$

For simplification, the following notation will be used:

$$\hat{f} = T\,[f] \qquad\qquad \tilde{f} = A\,[f] \tag{2.4.3}$$

### 2.4.1 Fourier transform properties

The Fourier transform has the following basic properties:

#### Linearity

Fourier and inverse Fourier transforms are linear.

$$T\left[f+g\right]=T\left[f\right]+T\left[g\right] \qquad A\left[f+g\right]=A\left[\hat{f}\right]+A\left[\hat{g}\right] \tag{2.4.4}$$

#### Translation formulas

The following translation formulas are valid (where $a$ is a real constant):

$$T\left[f\left(\mathrm{x}-a\right)\right]=e^{iqa}\,T\left[f\left(\mathrm{x}\right)\right] \tag{2.4.5}$$

$$T\left[e^{-ia\mathrm{x}}f\left(\mathrm{x}\right)\right]=\hat{f}\left(q-a\right) \tag{2.4.6}$$

#### Convolution product

In many applications it is useful to use the convolution product between two functions; this is given by

$$\left(f*g\right)\left(\mathrm{x}\right)=\frac{1}{\sqrt{2\pi}}\int f\left(\mathrm{x}-\mathrm{y}\right)\cdot g\left(\mathrm{y}\right)\;d\mathrm{y} \tag{2.4.7}$$

The convolution product is obviously commutative and associative,

$$f*g=g*f \qquad \left(f*g\right)*h=f*\left(g*h\right) \tag{2.4.8}$$

The convolution product has a particularly simple property under Fourier transform:

$$T\left[f*g\right]=T\left[f\right]\cdot T\left[g\right]=\hat{f}\left(q\right)\cdot\hat{g}\left(q\right) \tag{2.4.9}$$

#### Fourier transform of a Gaussian function

For a Gaussian function described as follows:

$$f\left(\mathrm{x}\right)=\frac{1}{\sqrt{2\pi}}e^{-\mathrm{x}^2/\left(2A^2\right)} \tag{2.4.10}$$

the Fourier transform will be

$$\hat{f}\left(q\right)=\frac{A}{\sqrt{2\pi}}e^{-A^2q^2/2} \tag{2.4.11}$$

Note that if $A=1$ then $\hat{f}=f$. This property is useful for Persson's theory, which will be discussed in detail in Section 4.2 in Chapter 4, where the contact pressure distribution is assumed to be Gaussian.

## 2.5 Hertz theory

Hertz contact theory is a classical theory of contact mechanics [31]. The Hertz solution is obtained under the assumption of a parabolic pressure distribution, which is a very good approximation for spherical, elliptical, sinusoidal or cylindrical bodies in contact. Other assumptions of Hertz theory are:

- The strains are small (small deformations).
- Each solid can be considered as an elastic half-space.
- The surfaces are frictionless.

The full derivation and the description can be found in the classical contact mechanics books [38, 109].

For very large dragging velocities, the material has no time to relax and it show a stiff response so that, the contact area ratio is expected to tend asymptotically to the value that would be obtained in small strain conditions for an elastic material with an instantaneous modulus $E_0 = E\,(\omega \to \infty,\, t \to 0)$. These asymptotic values can be calculated with the Hertz theory. They are reported in Subsection 4.4.2 in Chapter 4.

For a special case of a sinusoidal surface with an amplitude $\Delta$ and a wavelength $L_0$, the local radius of curvature R is calculated from the following expression [38]:

$$R = \frac{L_0^2}{4\pi^2\Delta} \tag{2.5.1}$$

The minimum contact radius can be estimated as a function of the maximum frequency-dependent elastic modulus of the material $E_0$, the Poisson's ratio $\nu$ and the applied pressure $\bar{p}$ as

$$a_{\min} = \sqrt{\frac{4\bar{p}L_0R\,(1-\nu^2)}{\pi E_0}} \tag{2.5.2}$$

The instantaneous elastic modulus $E_0$ is determined for generalized Maxwell material as:

$$E_0 = E_\infty + \sum_{k=1}^{N} E_k \tag{2.5.3}$$

Finally, the dimensionless asymptotic values of the minimum contact area ratio are calculated as:

$$c_{\min} = 2\frac{a_{\min}}{L_0} \tag{2.5.4}$$

# Chapter 3

# Analysis of asphalt specimens

The nature of the road surface plays an important role in car tire friction. The measured friction values on road tracks vary strongly with varying roughness scales [113, 118]. Thus, a proper description of the roughness character seems to be very important to predict the frictional behavior. Since each asperity of the road surface generates sliding friction at a different frequency, this influences the hysteretic frictional behavior. Therefore, a detailed description of the surface geometry on all relevant scales is crucial.

In this chapter, a profilometer is used to measure the roughness of a road track specimen made of asphalt. A brief introduction about profilometry and surface roughness parameters is given. An overview of the fractal nature of road tracks and their approximation is presented also in this chapter. The following step is to decompose the measured road track into a finite number of sinusoidal functions by fitting the height difference correlation function.

## 3.1 Profilometry

A profilometer is a measuring instrument used to measure a surface profile, in order to quantify its roughness. There are two types of profilometers: stylus and optical. Stylus profilometers use a probe to measure the surface [1, 45]. The probe is moved physically along the surface in order to acquire the surface height. This is done mechanically with a feedback loop that monitors the force from the sample pushing up against the probe as it scans along the surface. A feedback system is used to keep the arm with a specific amount of torque on it, known as the ”setpoint”. The changes in the vertical position of the arm holder can then be used to reconstruct the surface.

Stylus profilometry requires force feedback and physically touching the surface, so while it is extremely sensitive and provides high vertical resolution, it is less suited to soft surfaces and the probe can become contaminated by the surface. Furthermore, since a stylus profilometer involves physical movements in all directions while maintaining contact with the surface, it is slower than non-contact techniques. The stylus tip size and shape can affect the measurements and limit the lateral resolution [79].

Optical profilometry uses light instead of a physical probe. The key component of this technique is directing the light in a way that it can measure the surface.

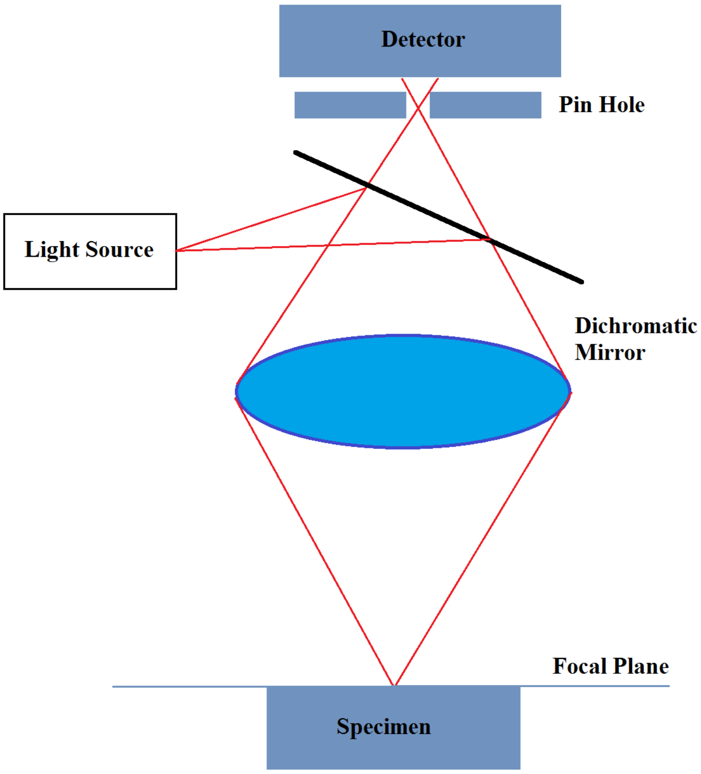

**Figure 3.1:** Principle of confocal profilometer.

Confocal profilometry is a point scanning optical technique used to image the sample surface. It works by using a small aperture, known as a confocal sensor. Highly focused light is projected through the aperture and only surfaces within the focal plane will provide a useful signal. The optics are moved above the surface until a bright spot is observed. Once a bright spot is observed the instrument calculates the distance to that point on the surface, giving it a point in the vertical direction. The optics then scan along the surface laterally while maintaining a bright spot to reconstruct the surface. Confocal profilometry can be slower than stylus profilometry, but it is less sensitive to vibrations compared to stylus [79].

A confocal optical profilometer has been used in this work to measure asphalt specimens. The profilometer consists of the following parts:

- A confocal sensor which determines the sample height at a single point on the specimen.
- Sample stage with a positioning system that holds the sample.

- Sensor controller.
- Poisitioning system controller.

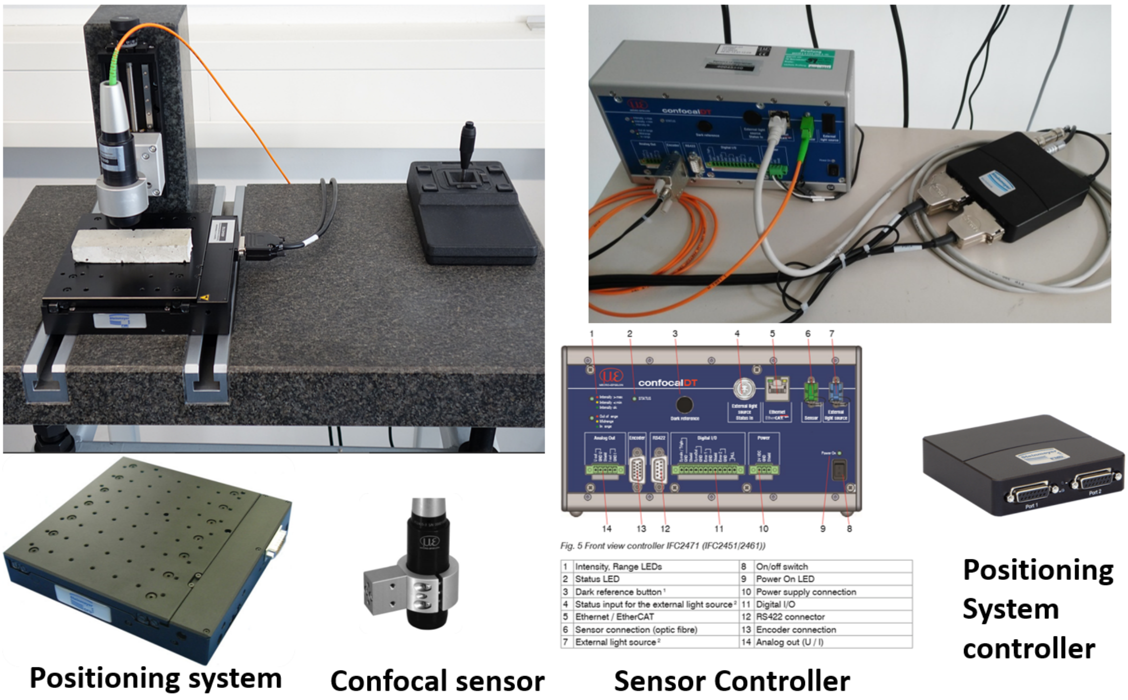

*Fig. 5 Front view controller IFC2471 (IFC2451/2461))*

| | | | |
|---|---|---|---|
| 1 | Intensity, Range LEDs | 8 | On/off switch |
| 2 | Status LED | 9 | Power On LED |
| 3 | Dark reference button [1] | 10 | Power supply connection |
| 4 | Status input for the external light source [2] | 11 | Digital I/O |
| 5 | Ethernet / EtherCAT | 12 | RS422 connector |
| 6 | Sensor connection (optic fibre) | 13 | Encoder connection |
| 7 | External light source [2] | 14 | Analog out (U / I) |

**Figure 3.2:** The used profilometer components.

According to Persson [68], the lower limit of the road track wavelengths (short-distance cut-off) must be in the range between 0.04 to 0.08 [mm] and the roughness below this scale shall be excluded, due to dust and dirt particles which fill the smaller cavities of the track in addition to trapped pockets of compressed air and the water trapped in surface cavities. The lateral resolution of the profilometer (0.05 [mm]) gives an acceptable degree of accuracy. The lower cut-off was selected as 0.0625 [mm].

The upper cut-off is selected as the typical largest grain size of asphalt. It ranges between 0.5 and 2 [cm].

The profilometer has a maximum travelling distance of 48 [mm], a maximum travelling speed of 7 [mm/s], a sampling rate range from 0.3 to 70 [kHz] and a lateral resolution of 50 [$\mu$m].

The asphalt specimen was provided by the Pavement Engineering Centre (ISBS), TU-Braunschweig. In order to get representative data for the specimen, 30 line scans at different regions of the specimen are done in different directions. Each of them has a measurement length of 16 [mm] that is consistent with the typical grain size of asphalt. The measurement speed is 0.1 [mm/s]. The measurement rate is selected as 1[kHz], which is suitable for dark specimens like asphalt. The specimen is shown in Figure 3.3.

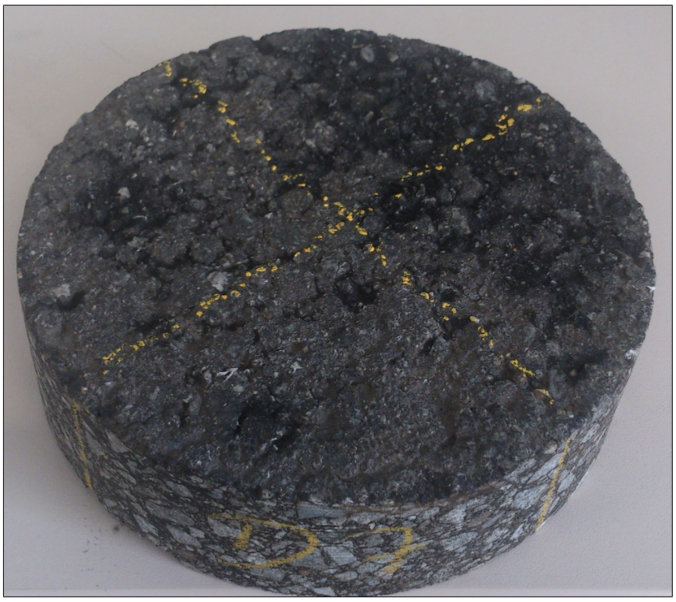

**Figure 3.3:** Asphalt specimen.

## 3.2 Surface roughness parameters

Amplitude parameters characterize the surface roughness based on the vertical deviations of the roughness profile from the mean line. These parameters (except skewness and kurtosis) are obtained directly from profilometer data. Figure 3.4 shows the definition of the surface roughness parameters introduced as follows.

$R_a$ is the average absolute deviation of the profile points from a mean line

$$R_a = \frac{1}{N} \sum_{i=1}^{N} |z_i| \tag{3.2.1}$$

where N is the number of measurement points, and $z_i$ is the vertical distance from the mean line to the i-th data point.

$R_q$ is the root mean square deviation of a profile about the mean line, also denoted as RMS.

$$R_q = \sqrt{\frac{1}{N} \sum_{i=1}^{N} z_i^2} \tag{3.2.2}$$

$R_p$ is the distance from the mean line to the highest point. It represents the maximum peak height:

$$R_p = \max(z_i) \tag{3.2.3}$$

$R_v$ is the distance from the mean line to the lowest point. It represents the maximum valley depth. It has always a negative value:

$$R_v = \min(z_i) \tag{3.2.4}$$

$R_t$ is the highest difference between the highest and the lowest point within the sampling length of a profile. It represents the maximum height of the profile.

$$R_t = R_p - R_v \tag{3.2.5}$$

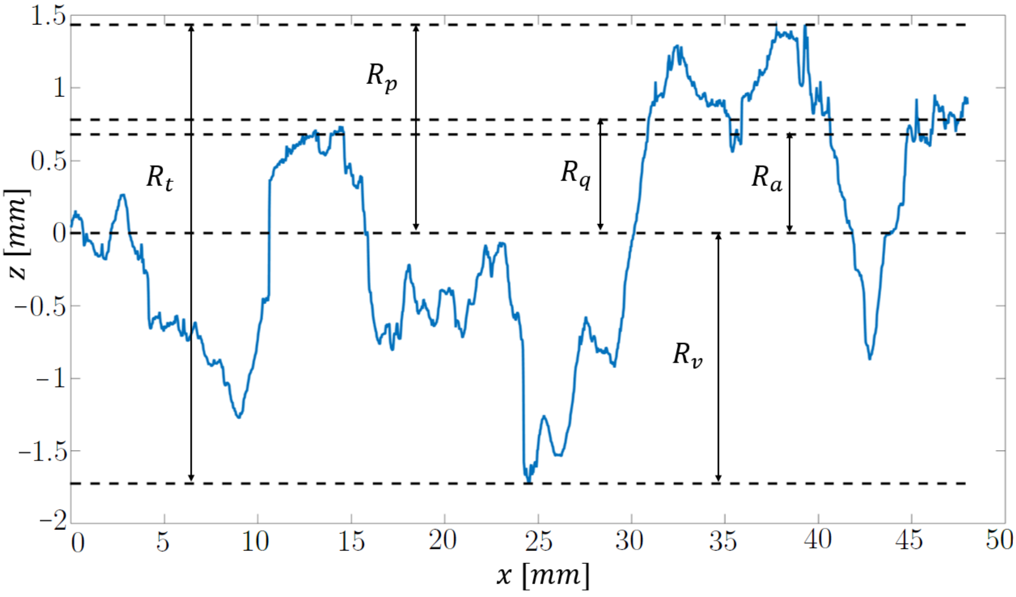

**Figure 3.4:** Definition of surface roughness parameters.

$R_{sk}$ is the skewness of the roughness amplitudes distribution. It is a measure of the asymmetry of the profile.

$$R_{sk} = \frac{1}{N \cdot R_q^3} \sum_{i=1}^{N} z_i^3 \tag{3.2.6}$$

A negative skewness value $R_{sk} < 0$ means that the surface is skewed towards high surface heights, while a positive skewness value $R_{sk} > 0$ means that the surface is skewed towards low surface heights, and a zero skewness values $R_{sk} = 0$ means that the surface is symmetrical about the average line and has a Gaussian distribution.

According to Fortunato [21], asphalt road surfaces usually exhibit a negative skewness. This is a result of the production process where the hot asphalt is compressed and smoothed by rolling a heavy cylinder on the asphalt surface. The negative skewness implies that the surface roughness above the average value is reduced as compared to a surface with zero skewness. This will, for a given contact pressure, result in a larger contact area.

$R_{ku}$ is the kurtosis of the roughness amplitude distribution. It is a measure of the "sharpness" of the surface heights distribution:

$$R_{ku} = \frac{1}{N \cdot R_q^4} \sum_{i=1}^{N} z_i^4 \tag{3.2.7}$$

A kurtosis value larger than three $R_{ku} > 3$ means that the height distribution is sharp, while a kurtosis value less than three $R_{ku} < 3$ means that the height distribution is not sharp, and a $R_{ku} = 3$ means normal distribution of heights.

## 3.3 Surface description

Rough road tracks usually made of asphalt or concrete are rough over many length scales and exhibit the self-affine character of fractal surfaces [40, 61, 62, 68]. An overview of fractal geometry is given by Mandelbrot [56]. By definition, self-affine surfaces show statistical invariance under anisotropic dilation in a certain surface-wavelength ($\lambda$) range, meaning a rough surface shows the same statistical properties and morphology under a length scale $\lambda$ in cross section direction and $\lambda^2 H$ in the perpendicular direction. The so-called Hurst exponent $H$ is introduced as a measure for surface irregularity. The values of $H$ are located in the following range $0 \leq H \leq 1$. $H = 1$ describes a smooth surface, while $H = 0$ indicates a very rough surface.

There are several methods introduced by many researchers to characterize the fractal road surfaces. The most important approaches for the present work are the height difference correlation function introduced by Heinrich and Klüppel [40], the power spectral density suggested by Persson [74], and the surface approximation using a superposition of multiple sine waves with different amplitudes and wavelengths suggested by Reinelt and Wriggers [118]. They are explained as follows.

### 3.3.1 Height difference correlation function

One way to describe the fractal asphalt rough surfaces mathematically is to calculate the height difference correlation (HDC) function. It is introduced as

$$C_{HDC}(\lambda) = \left\langle (\mathrm{z}(\mathrm{x}+\lambda) - \mathrm{z}(\mathrm{x}))^2 \right\rangle . \tag{3.3.1}$$

This function describes the mean ($\langle\cdot\rangle$) square height difference of the height profile $\mathrm{z}(\mathrm{x})$ for different horizontal length scales $\lambda$ in x-direction. It compares the height z of two nearby points with a horizontal distance $\lambda$, see Figure 3.5.

For self-affine surfaces, the HDC function is described in the form of a power law.

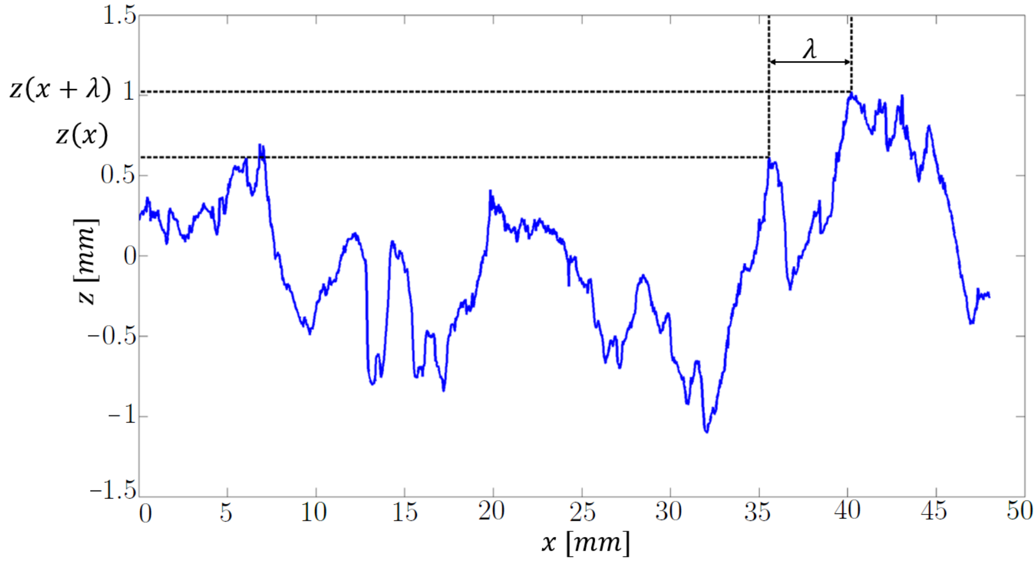

**Figure 3.5:** Height difference correlation function definition.

$$C_{HDC}(\lambda) = \xi_{\perp}^{2}\left(\frac{\lambda}{\xi_{\parallel}}\right)^{2H}, \quad \lambda \leq \xi_{\parallel} \tag{3.3.2}$$

$$C_{HDC}(\lambda) = \xi_{\perp}^{2} \quad\quad, \quad \lambda > \xi_{\parallel} \tag{3.3.3}$$

The HDC function of a self-affine track is depicted in Figure 3.6. The progress of the curve is linear on a double logarithmic scale until a maximum value around the upper cut-off length is reached. Then it settles down to a constant plateau since the height differences are determined by surface envelope. The exponent $2H$ denotes the slope of the gradient section. The upper cutoff-point is defined by the values $\xi_{\perp}^{2}$ and $\xi_{\parallel}$. They are the correlation lengths in the normal and the tangential directions of the surface, respectively.

### 3.3.2 Power spectral density

Another function to characterize the statistical properties of the surface is the power spectral density (PSD). The PSD is defined as the Fourier map of the HDC function. It is introduced by Persson [76] as:

$$C_{PSD}(\mathrm{q}) = \frac{1}{(2\pi)^{2}} \int \langle \mathrm{z}(\mathrm{x})\, \mathrm{z}(0) \rangle\, e^{-i\mathrm{qx}} d\mathrm{x}, \tag{3.3.4}$$

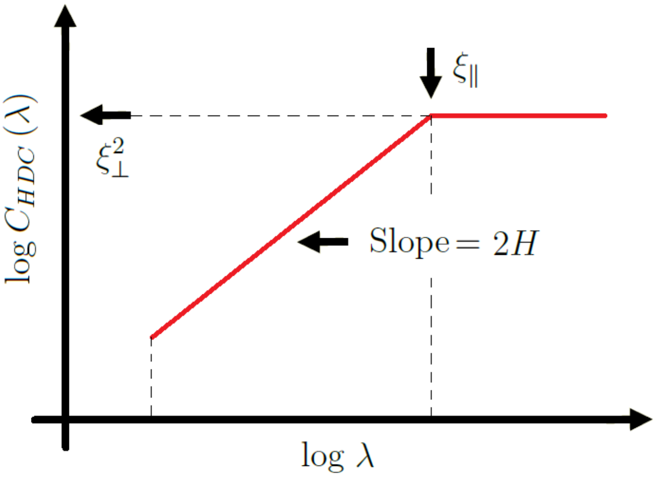

**Figure 3.6:** Scheme of HDC function of a self-affine rough road surface.

where x is the spatial in-plane coordinate, z (x) is the surface height measured from the average surface plane, z (0) is the mean height of the profile. Under the assumption that the statistical properties of the considered surface are translationally invariant and isotropic, the magnitude of the wave vector $q = |\boldsymbol{q}|$ is used to evaluate $C_{PSD}$.

For an ideal case of isotropic PSD with a self affine surface, the PSD will be defined by Persson as [74].

$$C_{PSD}(q) = C_0 \qquad , \qquad q > q_r \tag{3.3.5}$$

$$C_{PSD}(q) = C_0 \left(\frac{q}{q_r}\right)^{-2(H+1)} , \qquad q \leq q_r \tag{3.3.6}$$

where $q_0$, $q_r$ and $q_1$ are the lower, roll-off, and the upper wavenumbers respectively (or equivalently the longest, roll-off and shortest wavelengths). Figure 3.7 shows a schematic example of a PSD function of a a self affine road track.

The PSD function and the HDC function can be equally used to describe the characteristics of a self-affine rough rigid surface and can be transformed to each other.

The mean square slope roughness can be defined from PSD from the following relation as [86]:

$$m_2 = \left\langle |\nabla z|^2 \right\rangle = \int q^2\, C_{PSD}(q)\; dq. \tag{3.3.7}$$

For a self-affine surface, the RMS of surface gradient $h_{rms}^2$ is written as

$$h_{rms}^2 = \int C_{PSD}(q)\; dq = \pi\, C_0\, q_r^2 \left[ \left(1 - q_0^2/q_r^2\right) + \frac{1 - (q_1/q_r)^{-2H}}{H} \right]. \tag{3.3.8}$$

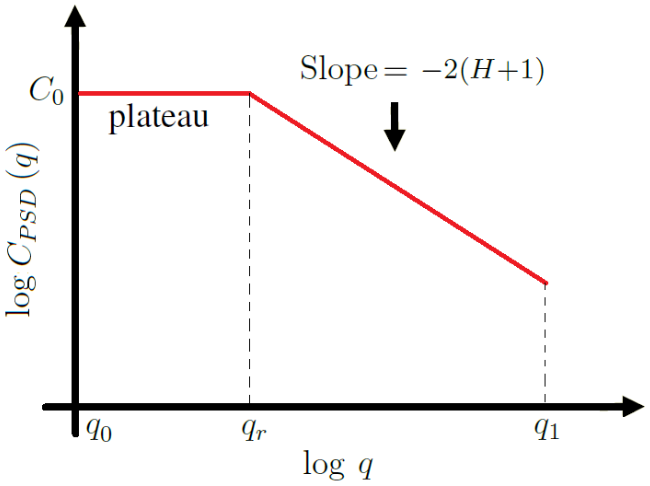

**Figure 3.7:** Scheme of PSD function of a self-affine rough road surface.

The mean square slope for a self-affine track reads [74]:

$$\left[m_2^2(q)\right]_{q>q_r} = \int q^2\, C_{PSD}(q)\ dq = \pi\, C_0\, q_r^4 \left[\frac{(1-q_0^4/q_r^4)}{2} + \frac{(q/q_r)^{2(1-H)}-1}{(1-H)}\right]. \quad (3.3.9)$$

## 3.3.3 Superposition of sinusoidal functions

The motivation to approximate the measured surface by a finite number of sinusoidal waves is to establish multiscale approaches, which allow for a more robust calculation of friction coefficient. The approach was suggested by Reinelt and Wriggers [118] and adopted by other researchers [20]. In their method, they approximated the measured road track with a superposition of multiple sine waves with different amplitudes and wavelengths.

### HDC function of a sinusoidal function

A single sine wave function is characterized by amplitude $\Delta$ and wavelength $L_0$, see Figure 3.8. The latter can be controlled by the wave number q.

$$\mathrm{z}(\mathrm{x}) = \Delta\cdot\sin(q\mathrm{x}) \qquad L_0 = \frac{2\pi}{q} \quad (3.3.10)$$

The equivalent HDC function can be written using equation (3.3.1) as

$$C_z(\lambda) = \frac{q}{2\pi}\int_0^{2\pi/q} \left[\Delta\cdot\sin(q\mathrm{x}+q\lambda) - \Delta\cdot\sin(q\mathrm{x})\right]^2 d\mathrm{x} = 2\Delta^2\cdot sin^2\left(\frac{q\lambda}{2}\right) \quad (3.3.11)$$

On a double logarithmic scale, the general characteristics of a sinusoidal surface show a linear progress for small $\lambda$ until a maximum value around the upper cut-off length

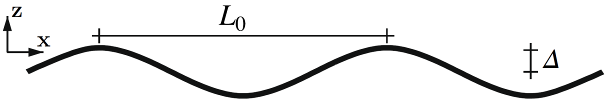

**Figure 3.8:** Sinusoidal surface profile.

is reached. Then the HDC function settles down to a constant plateau. The HDC function of a sine wave could be written as:

$$\tilde{C}_z(\lambda) = 2\Delta^2 \cdot sin^2(\frac{q\lambda}{2}) \qquad \lambda \leq \frac{\pi}{q} \tag{3.3.12}$$

$$\tilde{C}_z(\lambda) = 2\Delta^2 \qquad \lambda > \frac{\pi}{q} \tag{3.3.13}$$

Figure 3.9 shows the HDC function of a simple sine function. The slope of the double logarithmic diagram is D=2. However, track profiles usually have slopes in range of 2.1 to 2.5 [95]. Therefore, in order to achieve a better fit to the measured road track data, multiple sine waves with different amplitudes and wavelengths must be superposed. The more functions are used the better is the agreement with the original surface.

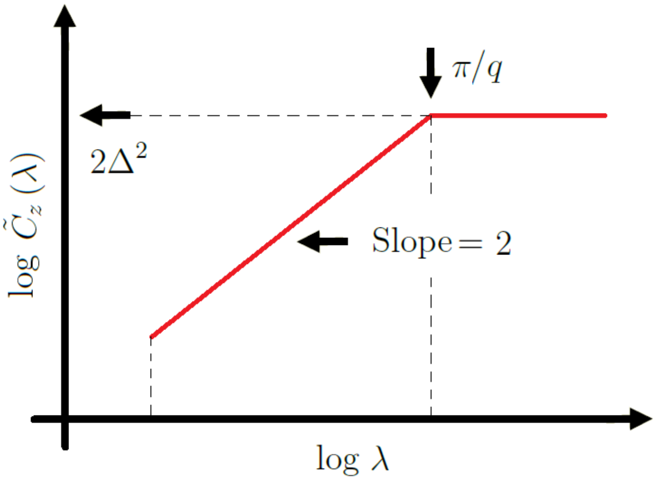

**Figure 3.9:** Scheme of HDC function of a simple sine function.

### Mean square slope of a sinusoidal function

For a simple sinus surface as described in Figure 3.8, the mean square slope roughness is described as [87]

$$m_2^2 = \langle \mathrm{z}\,(\mathrm{x})\,\mathrm{z}\,(0) \rangle = 2\pi^2 \frac{\Delta^2}{L_0^2} \tag{3.3.14}$$

$$m_2 = \sqrt{2}\pi \frac{\Delta}{L_0}, \tag{3.3.15}$$

## 3.4 Surface approximation

The measured track is approximated by a sum over a number of sinusoidal functions $i$

$$\mathrm{z}\left(\mathrm{x}\right)=\sum_{i=1}^{M}\Delta_i\cdot\sin\left(q_i\mathrm{x}+\phi_i\right) \tag{3.4.1}$$

with a random shift angle $\phi_i$. The rough surface is assumed to be periodic with periodicity length $2\pi/q_0$. The Fourier series decomposition of the roughness is therefore characterized by frequencies $q_i = 2^i \cdot q_0$, where $i = 1 : M$ is an integer number which refers to the approximated sinusoidal functions. $M$ is the number of the approximated sine functions. This selection of frequencies (length scales) will allow a better representative approximation of the measured track and it will achieve the periodicity between the selected length scales.

The HDC function of the measured track $C_z\left(\lambda\right)$ consists of N measured points. The index j refers to the j-th point of the measured HDC function.

The superposed sinusoidal functions are fitted to the measured surface based on their HDC functions using the least square algorithm on a double logarithmic scale, which identify the amplitudes $\Delta_i$ and the spatial frequencies $q_i$ such that the following equations hold

$$E=\left(\sum_{j=1}^{N}\left(\sum_{i=1}^{M}\log\left(2\Delta_i^2\cdot sin^2(\frac{q_i\lambda_j}{2})\right)-\log\left(C_z\left(\lambda_j\right)\right)\right)^2\right)^{\frac{1}{2}}\rightarrow\min\qquad\lambda_j\leq\frac{\pi}{q_i} \tag{3.4.2}$$

$$E=\left(\sum_{j=1}^{N}\left(\sum_{i=1}^{M}\log\left(2\Delta_i^2\right)-\log\left(C_z\left(\lambda_j\right)\right)\right)^2\right)^{\frac{1}{2}}\rightarrow\min\qquad\lambda_j>\frac{\pi}{q_i} \tag{3.4.3}$$

where $E$ is the least squares error.

We will test two different numbers of sine waves to approximate the asphalt surface. The first approximation consists of 8 sinusoidal harmonic functions, while 9 sinusoidal waves are considered in the second approximation. The comparison is performed in order to estimate the surface sensitivity of the approximation used. Using lower number of sinusoidal functions with the aforementioned assumption of periodicity will result in large variances in the HDC function, see Figure 3.10.

### Approximation 1- Eight sinusoidal waves

The first approximation results from the superposition of 8 sinusoidal waves with different amplitudes and wavelengths. The HDC function of the sine waves (colored lines) and their superposition (dashed black line) are depicted in Figure 3.11. The red line

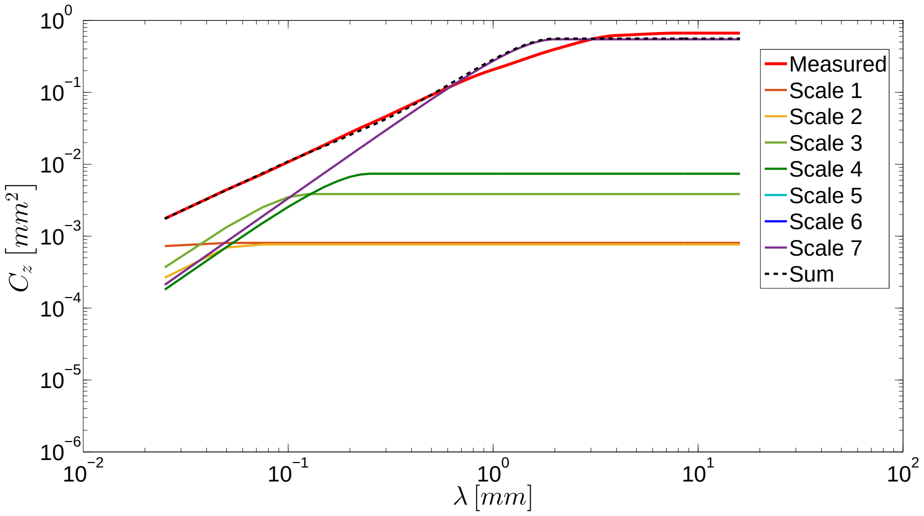

**Figure 3.10:** HDC function of asphalt road measurement, approximated by superposition of 7 sinusoidal waves. Note that using less than 8 sinusoids gives a lower accuracy in the surface approximation.

**Table 3.1:** Surface approximation for asphalt specimen using 8 sine waves

| **Scale** | **Wavelength [mm]** | **Amplitude [mm]** | $m_2$ |
|---|---|---|---|
| 1 | 0.0625 | 0.01867 | 1.3275 |
| 2 | 0.125 | 0.02648 | 0.9403 |
| 3 | 0.25 | 0.02939 | 0.5223 |
| 4 | 0.5 | 0.06626 | 0.5888 |
| 5 | 1 | 0.06177 | 0.2744 |
| 6 | 2 | 0.21635 | 0.4806 |
| 7 | 4 | 0.14772 | 0.1641 |
| 8 | 8 | 0.48995 | 0.2721 |

denotes the averaged measured asphalt road track.

The gradient of the measured line and the superposed fitted line is identical, but their cut-off-lengths differ.

Table 3.1 lists the superimposed sine wavelengths and amplitudes approximated using 8 sinusoidal waves. The identified values of amplitude and wavelength and the corresponding mean square slope are listed in the table. One can note that only one scale has a mean square slope larger than 1.

### Approximation 2- Nine sinusoidal waves

The second approximation has an additional macro sine wave. It keeps the same RMS height as well as the same smallest wavelength of the first approximation since the

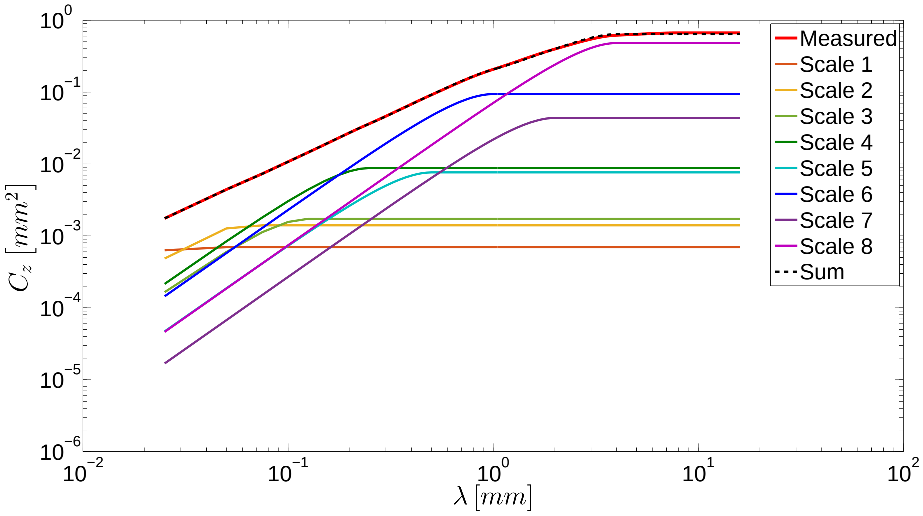

**Figure 3.11:** HDC function of asphalt road measurement, approximated by superposition of 8 sinusoidal waves

friction coefficient is sensitive to the selection of the smallest wavelength [86, 92, 118]. An extra wavelength of $\lambda_{\max} = 16\,[mm]$ is added in this approximation.

Figure 3.12 shows the single and the superposed sine waves for this approximation. The red line denotes the measured line. As can be seen, this approximation gives identical values with the measured line. As the number of sinusoidal waves increases, the approximation improves. The approximated wavelengths and amplitudes using super-

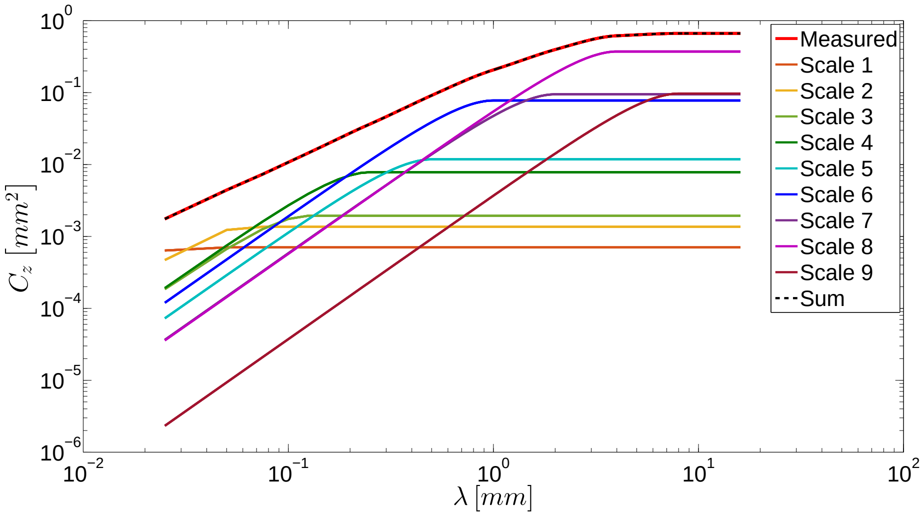

**Figure 3.12:** HDC function of asphalt road measurement, approximated by superposition of 9 sinusoidal waves

**Table 3.2:** Surface approximation for asphalt specimen using 9 sine waves

| **Scale** | **Wavelength [mm]** | **Amplitude [mm]** | $m_2$ |
|---|---|---|---|
| 1 | 0.0625 | 0.01876 | 1.3333 |
| 2 | 0.125 | 0.02608 | 0.9269 |
| 3 | 0.25 | 0.03111 | 0.5229 |
| 4 | 0.5 | 0.06250 | 0.5554 |
| 5 | 1 | 0.07684 | 0.3414 |
| 6 | 2 | 0.19695 | 0.4375 |
| 7 | 4 | 0.21748 | 0.2416 |
| 8 | 8 | 0.43148 | 0.2396 |
| 9 | 16 | 0.21994 | 0.0611 |

position of 9 sinusoidal waves and their corresponding mean square slope are listed in Table 3.2. It is also obvious from the table that only one scale has a mean square slope larger than 1.

Since the measured track is perfectly approximated either with 8 or with 9 sine functions, there will be no need to use more sine functions to approximate the road track.

# Chapter 4

# The influence of geometrical and rheological non-linearity on the calculation of rubber friction

## 4.1 Introduction

Rubber friction can be calculated in the framework of linear viscoelasticity with infinitesimal deformations [11, 13, 14, 68, 72, 88, 91], as well as recurring to the Reynolds roughness assumption, i.e. the roughness square slope $m_2 < 1$. The aforementioned assumptions allow for the use of the viscoelastic half-space (VHS) theory [38] in modeling the deformation response of generic contacting surfaces. This approach is typically adopted in multiscale [68] as well as multi-asperity [40, 44] viscoelastic contact theories and implemented with boundary element numerical formulations [13, 65, 88, 90, 91].

On the other hand, kinematically non-linear continuum mechanics formulations, implemented numerically through finite element (FE) approaches, are able to remove both assumptions and provide a prediction of rubber friction in the finite deformation framework, for arbitrary geometry of the contacting bodies and arbitrary constitutive behavior of the material, albeit with a much higher computational cost[1] .

Multiscale approaches in the numerical FE context for contact to rough surfaces have been proposed by several authors [4, 17, 20, 101, 103, 104, 111, 118]. In particular, micro-rolling rubber friction has been recently addressed in [17, 20, 118]. Here the contributions of the various scales are computed by the decomposition of the roughness profile into sinusoidal components of appropriate amplitudes and wavelengths. The basic building block of this multiscale approach is therefore the computation of rubber friction in the case of a sinusoidal surface, i.e. the simple Westergaard geometry [38].

More in general, the single wavelength profile is often adopted in the contact mechanics literature, since it allows to accurately capture, at least qualitatively, most of

---

[1] Some text passages of this chapter have been quoted verbatim from [87].

the physics occuring in more complex rough contact conditions [10, 12, 57, 122].

It should be noted that, in the full contact case and within linear assumptions, the (both stored and dissipated) energy contributions of each roughness length scale characterizing the surface become effectively uncorrelated in the Fourier space, i.e. different wavelengths contribute independently from each other in the space of frequencies.

In this chapter, a quasi-static isothermal sliding contact of a single rigid roughness wavelength (a Westergaard geometry) on a viscoelastic half-space is taken into account.

The goal of this chapter is to investigate how the linearity assumptions quantitatively affect the rubber friction calculations. Another goal to this chapter is to give a fundamental understanding of the role of non-linearities on the the resulting interface dissipation and contact area formation at the asperity scale. For this aim, predictions of a novel VHS-based numerical contact mechanics model, based on linear kinematics and formulated in terms of boundary elements in the Fourier space, are compared with those of a FE formulation of the viscoelastic contact problem in the finite deformation framework. In both models, a realistic rubber rheology, involving multiple relaxation times, is adopted as required for the accurate description of the rubber relaxation process. The comparison allows to shed light on the accuracy of the widely used assumption of geometric and rheological nonlinearity in the evaluation of rubber friction and contact area.

This chapter consists of three parts. The first one deals with the viscoelastic half-space (VHS)-based model implemented with the BEM. The formulation of the model along with the adopted solution procedure will be discussed.

The second part summarizes the model used for the calculation of rubber friction in the large deformation framework. This includes the material model, the contact formulation and the FE discretization.

In the last part of this chapter, the results from both approaches, in terms of friction coefficient and contact area, are presented and discussed.

## 4.2 Linear viscoelastic model

### 4.2.1 VHS-based formulation

The VHS-based model considers a rigid, periodically rough surface $z\left(\mathrm{x}\right)$ of wavelength $L_0$ in steady sliding adhesionless and frictionless contact with a viscoelastic half space, under isothermal conditions. The model assumes a small deformation regime to be applied, as well as a small square slope roughness, i.e. $m_2 < 1$.

Although the focus of the simulations is on the Westergaard geometry, the proposed

VHS-based model is more general. In Figure 4.1, a schematic representation of the contact geometry is visualized. The black surface represents the road surface, while the blue one refers to the rubber block. The local interface separation $u\left(\mathrm{x}\right)$ can be introduced as

$$u\left(\mathrm{x}\right)=\bar{u}+w\left(\mathrm{x}\right)-z\left(\mathrm{x}\right) \tag{4.2.1}$$

where $\bar{u}$ is the average interface separation. $w\left(\mathrm{x}\right)$ is the surface out-of-average plane displacement and $z\left(\mathrm{x}\right)$ the surface profile. It should be noted that the average values of $w\left(\mathrm{x}\right)$ and $z\left(\mathrm{x}\right)$ are zero.

$$\langle z\left(\mathrm{x}\right)\rangle=0, \qquad \langle w\left(\mathrm{x}\right)\rangle=0 \tag{4.2.2}$$

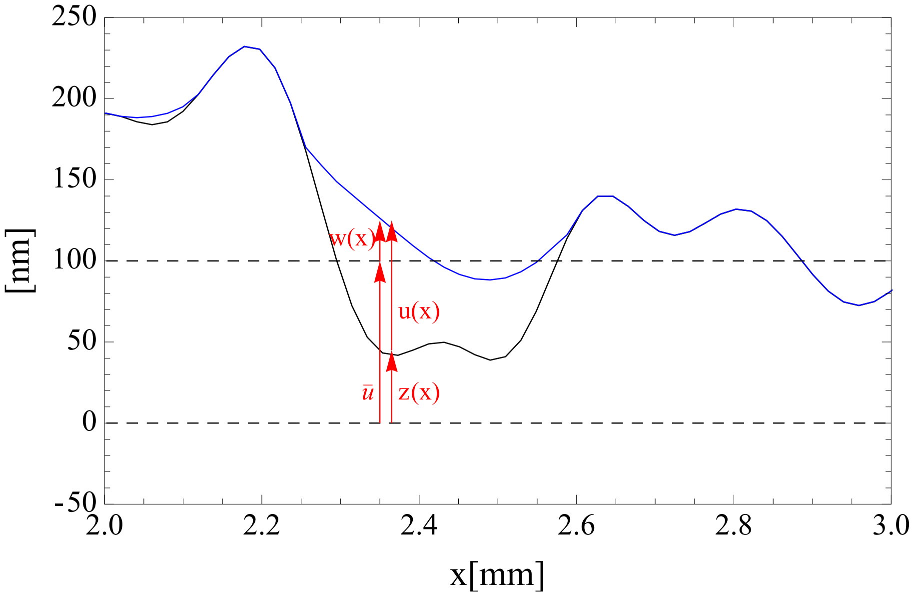

**Figure 4.1:** Generic cross section of the contact geometry.

The following Fourier transforms are defined for $w\left(\mathrm{x}\right)\rightarrow w\left(\mathrm{q}\right)$ as

$$w\left(\mathrm{q}\right)=\frac{1}{\left(2\pi\right)^{2}}\int w\left(\mathrm{x}\right)\, e^{-i\mathrm{qx}}d\mathrm{x} \tag{4.2.3}$$

and for the distribution of the interfacial pressures $t_N$

$$t_N\left(\mathrm{q}\right)=\frac{1}{\left(2\pi\right)^{2}}\int t_N\left(\mathrm{x}\right)\, e^{-i\mathrm{qx}}\,d\mathrm{x} \tag{4.2.4}$$

Scaraggi and Persson [91] suggested that for a linear viscoelastic half-space, one can relate $w\left(\mathrm{x}\right)$ to $t_N\left(\mathrm{x}\right)$ through a very simple equation in the Fourier space as follows

$$w\left(\mathrm{q}\right)=M_{zz}\left(\mathrm{q},\omega\right)\cdot t_N\left(\mathrm{q}\right) \tag{4.2.5}$$

where $M_{zz}(\mathrm{q}, \omega)$ is the complex surface response of the block in the frequency domain. It depends on the rheological and geometrical properties of the block. $M_{zz}(\mathrm{q}, \omega)$ can be written as

$$M_{zz}(\mathrm{q}, \omega) = \frac{2}{[|\mathrm{q}| \, E_r(\omega)]} \tag{4.2.6}$$

$E_r(\omega)$ is a frequency-dependent complex reduced Young's modulus; it is expressed as follows

$$E_r(\omega) = \frac{E(\omega)}{(1 - \nu^2)} \tag{4.2.7}$$

with $\nu$ as the Poisson's ratio. Persson states [68] that the Poisson's ratio undergoes only a tiny variation with the pulsating frequency and thus can be assumed to be constant for simplicity.

According to Lorenz [53], the viscoelastic modulus can be measured using standard techniques, and its real and imaginary part are typically fitted by a generalized Maxwell model [53, 91], obtaining for the reduced modulus:

$$\frac{1}{E_r(\omega)} \approx \frac{1}{E_r(\infty)} + \sum_{k=1}^{N} \frac{H_r(\tau_k)}{1 - i\omega\tau_k} \tag{4.2.8}$$

where N is the number of Maxwell elements, $H_r$ the discrete creep function and $\tau_k$ the k-th relaxation time. $E_r(\infty)$ is the asymptotic reduced elastic modulus in the glassy region of the rubber. In this work, N=6 in order to simulate a realistic rubber creep spectrum. The discrete creep function can be calculated from equation (2.2.9) in Chapter 2.

For adhesionless contact, it is known that:

$$t_N(\mathrm{x}) \geq 0 \tag{4.2.9}$$

$$u(\mathrm{x}) \, t_N(\mathrm{x}) = 0, \tag{4.2.10}$$

with $u(\mathbf{x}) \geq 0$. Once the solution is obtained, the projected contact area $A_c$ can be calculated by considering the grid points where $t_N > 0$, and assigning to each grid point a tributary area.

Finally, the micro-rolling friction coefficient can be determined as the ratio between the micro rolling friction force $F_r$ to the normal force $F_N$

$$\mu = \frac{F_r}{F_N} \tag{4.2.11}$$

Since the average sliding velocity $v_0$ is aligned with the x-axis, the micro-rolling friction coefficient $F_r$ reads

$$F_r = \int_{A_c} t_N(\mathrm{x}) \, \frac{\partial \mathrm{z}}{\partial \mathrm{x}} \, d\mathrm{x} \tag{4.2.12}$$

whereas the normal force $F_N$

$$F_N = \int_{A_c} t_N\left(\mathrm{x}\right)\, d\mathrm{x} \tag{4.2.13}$$

### 4.2.2 Numerical scheme

Discretizing the aforementioned equations on a regular square mesh gives the following set of equations

$$u_{ij} t_{Nij} = L_{ij} \tag{4.2.14}$$

This equation gives the generic residual $L_{ij}$ associated with the discrete version of equation (4.2.10), while the following equation is the discrete counterpart of equation (4.2.1).

$$w_{ij} = u_{ij} - \bar{u} + z_{ij} \tag{4.2.15}$$

$$w_{ij} \overset{FFT}{\to} \Delta t_N\left(q_{hk}\right) = M_{zz} w\left(q_{hk}\right) \overset{iFFT}{\to} t_{Nij} \tag{4.2.16}$$

Equation (4.2.16) originates from equation (4.2.5) and involves the Fast Fourier Transform (FFT), so that

$$t_{Nij} = \Delta t_{Nij} - \min\left(\Delta t_{Nij}\right) \tag{4.2.17}$$

The above mentioned equation (4.2.17) is equivalent to enforcing the condition in equation (4.2.9) at each grid point. whereas

$$\Delta t_{Nij} = t_{Nij} - \langle t_{Nij} \rangle \tag{4.2.18}$$

and $L_{ij}$=0 simply refers to the KKT conditions for adhesionless contact, see equation (2.3.27) in Chapter 2.

The set of nonlinear equations (4.2.14) to (4.2.17) with the unknowns $u_{ij}$, $t_{Nij}$ and $w_{ij}$ at the grid points (i,j) can be solved using a Newton-Raphson scheme. For this purpose, one can write the residual in equation (4.2.14) at the n-th iteration as follows:

$$L_{ij}^{(n+1)} = L_{ij}^{(n)} + \left(\frac{\partial L_{ij}}{\partial u_{hk}}\right)^{(n)} \Delta u_{hk}^{(n)} \tag{4.2.19}$$

The solution increment $\Delta u_{hk}^{(n)} = u_{hk}^{(n+1)} - u_{hk}^{(n)}$ is determined by solving $L_{ij}^{(n+1)}$=0. The Jacobian is calculated as follows:

$$\left(\frac{\partial L_{ij}}{\partial u_{hk}}\right)^{(n)} = \delta_i^h \delta_j^k t_{Nij}^{(n)} + u_{ij}^{(n)} \left(\frac{\partial t_{Nij}}{\partial u_{hk}}\right)^{(n)} \tag{4.2.20}$$

One can accurately approximate $\frac{\partial t_{Nij}}{\partial u_{hk}}$ as:

$$\frac{\partial t_{Nij}}{\partial u_{hk}} \approx \frac{\partial \Delta t_{Nij}}{\partial w_{hk}} \tag{4.2.21}$$

Assuming without loss of generality that $\mathbf{v}_0 = (v_0, 0)$, one can write:

$$\frac{\partial \Delta t_{Nij}}{\partial w_{hk}} \approx \delta_j^k C_{ij}^{hk} \tag{4.2.22}$$

$C_{ij}^{hk}$ represents the compliance matrix. Due to translational invariance, one can get

$$C_{ij}^{hk} = C_{i-h,|j-k|}^{0,0} \tag{4.2.23}$$

$C_{i-h,|j-k|}^{0,0}$ can be easily estimated through the application of Fourier transform in equation (4.2.5). Note that in equation (4.2.22), the coupling between points placed in different columns of the Jacobian has been removed (see the term $\delta_j^k$ in equation (4.2.22)).

Since some of the properties of the compliance matrix imply that

$$\left|\left(C_{ij}^{hk}\right)_{j=k}\right| > \left|\left(C_{ij}^{hk}\right)_{j\neq k}\right| \tag{4.2.24}$$

this allows for a parallel execution of the resolution of $L_{ij}^{(n+1)}$=0 along different mesh rows. The solution accuracy is arbitrarily set by requiring

$$\left\langle \left[L_{ij}^{(n)}\right]^2 / \bar{u}^2 \right\rangle^{1/2} < \varepsilon_L \tag{4.2.25}$$

and

$$\left\langle \left[u_{ij}^{(n)} - u_{ij}^{(n-1)}\right]^2 \right\rangle^{1/2} / \bar{u} < \varepsilon_u \tag{4.2.26}$$

where tolerances $\varepsilon_L$ and $\varepsilon_u$ are usually of order $10^{-6}$.

### 4.2.3 Model validation against existing results

The VHS numerical scheme is applied to the simplest case of a sinusoidal rigid surface, for which the literature provides analytical models for both elastic (Westergaard's solution [38]) and one-relaxation-time viscoelastic rheology (Hunter-Carbone solution [57]).

For elastic rheology, VHS predictions are compared with calculations using Westergaard theory. Figure 4.2 shows the contact area as a function of the dimensionless contact pressure. $p_0^*$ is the contact pressure corresponding to full contact. It is calculated from the following equation [38]

$$p_0^* = \frac{\pi E_r \Delta}{L_0} \tag{4.2.27}$$

where $E_r$ is the reduced elastic modulus that is defined in equation (4.2.7), $\Delta$ is the roughness amplitude, and $L_0$ is the roughness wavelength.

Figure 4.3 reports the contact pressure field corresponding to the arbitrarily chosen

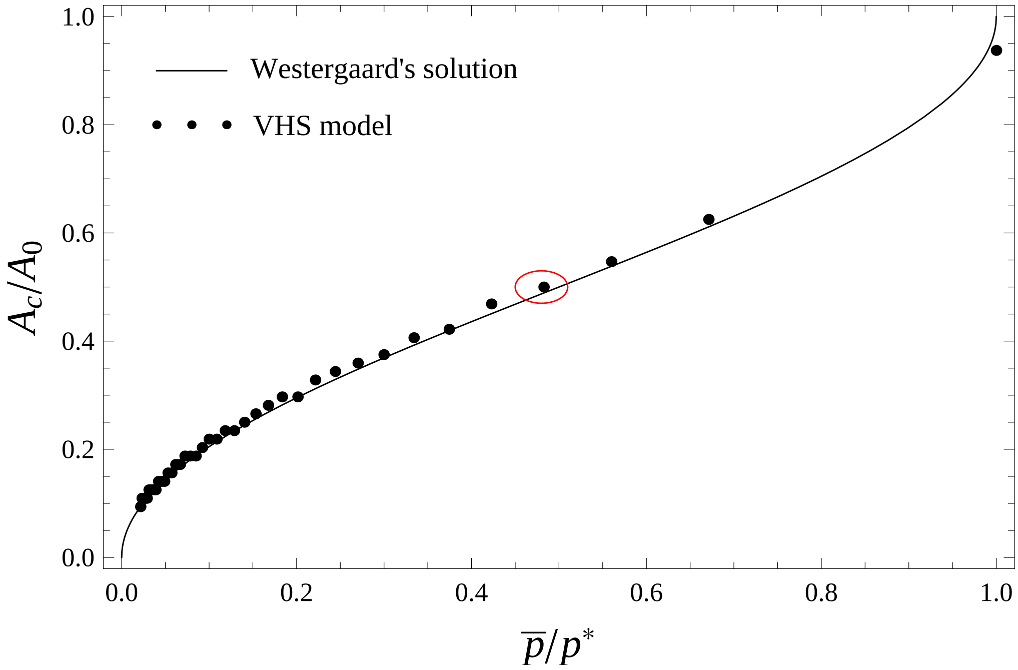

**Figure 4.2:** Normalized projected contact area as a function of the dimensionless applied pressure.

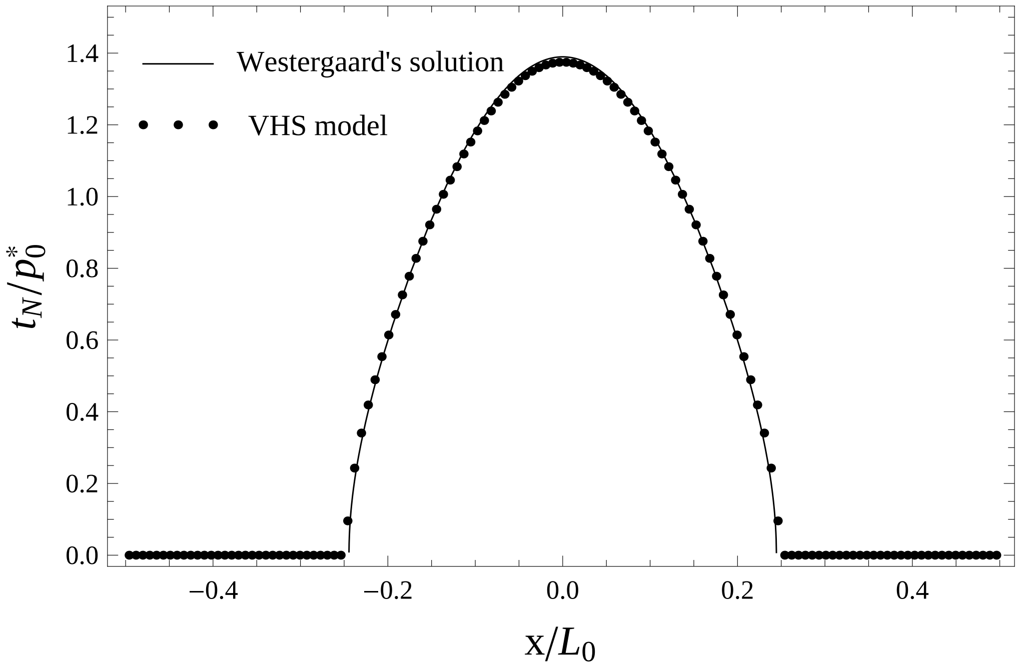

**Figure 4.3:** Dimensionless contact pressure field corresponding the encircled point in Figure 4.2.

(red) encircled point in Figure 4.2.

For a one-relaxation-time viscoelastic rheology, Figure 4.4 shows the interface separation field as predicted by the theory in [57] and the interface separation field as predicted by the proposed VHS model, for different sliding speeds. In this case, $\tau$=0.01 [s], $E_\infty$= 10 [MPa], $E_0$= $E_\infty/10$, Poisson's ratio $\nu$=0.5, $v^* = L_0/(2\pi\tau) = 5/\pi$ [m/s], $\bar{u} = 0.2\Delta$. In both cases, the agreement is excellent.

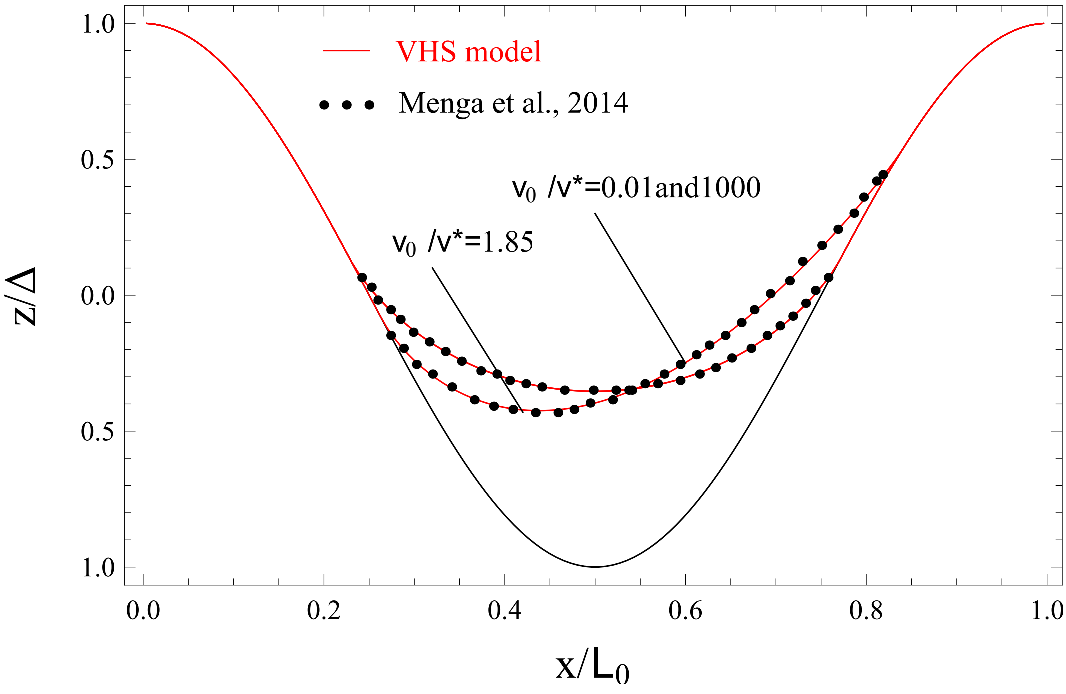

**Figure 4.4:** Dimensionless contact shape as a function of the dimensionless contact position.

Figures 4.5 and 4.6 show, respectively, the dimensionless contact pressure $t_N/p_0^*$ and the dimensionless interface separation z/Δ as a function of the dimensionless contact position x/L$_0$, for different velocities, at constant interface separation $\bar{u} = \Delta/2$. The considered velocities are 0, 1, 3, 6, 10, 100 and 1000 [m/s], which gives the curves from 1 to 7 in Figure 4.5, respectively. Four velocities are taken into account for Figure 4.6: they are 0, 1, 3 and 6 [m/s]. For the given rheological model, the contact pressure $p_0^*$ corresponding to full contact is defined, with respect to the relaxed (reduced) viscoelastic modulus $E_{r0}$, as follows:

$$p_0^* = \frac{\pi E_{r0}\Delta}{L_0} \tag{4.2.28}$$

One can observe that, for a given constant penetration, the contact areas in the rubbery and glassy rubber regimes are equal. This can be justified noting that the Hertzian theory suggests that

$$a^2 = \delta R, \tag{4.2.29}$$

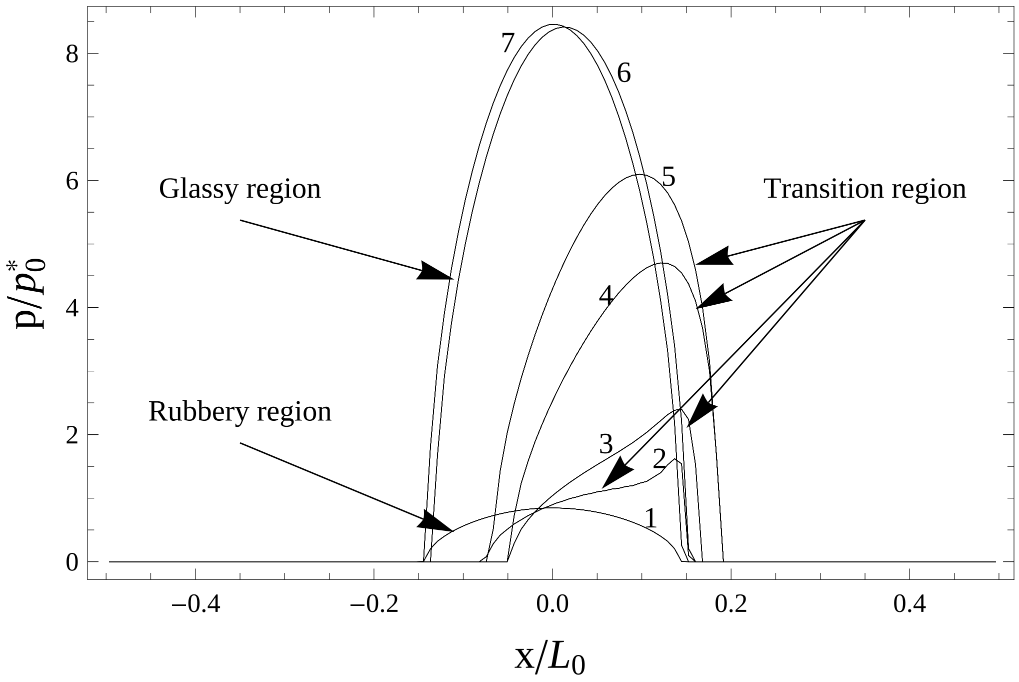

**Figure 4.5:** Dimensionless contact pressure field as a function of the dimensionless contact position.

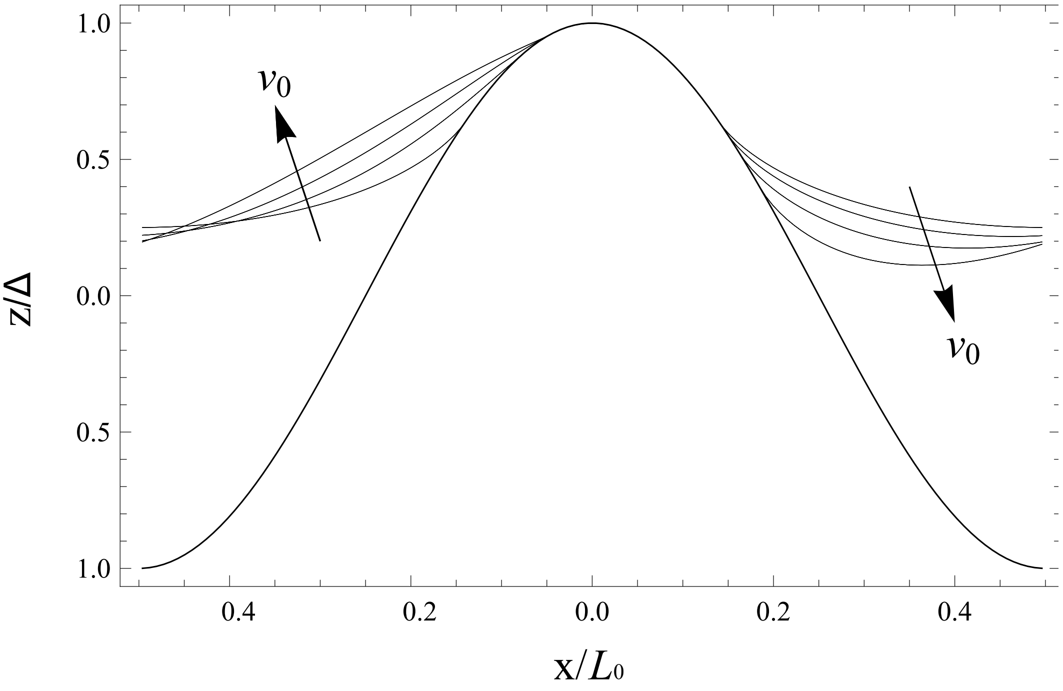

**Figure 4.6:** Dimensionless contact shape as a function of the dimensionless contact position.

where $a$ is the contact radius, $\delta$ is the penetration ($\delta = \Delta - \bar{u}$) and R the equivalent ball radius. Hence, within penetration control, the contact radius is independent of the elastic modulus, whereas

$$\frac{\max\left[t_N\left(\mathrm{x}, v_0 \to \infty\right)\right]}{\max\left[t_N\left(\mathrm{x}, v_0 \to 0\right)\right]} = \frac{E_\infty}{E_0} \tag{4.2.30}$$

Figure 4.7 illustrates the micro-rolling friction coefficient $\mu_r$ as a function of the dimensionless sliding velocity $v_0/v^*$. For a one-relaxation-time creep spectrum, the maximum of the loss modulus occurs at

$$\omega_{\max} = \frac{\sqrt{E_\infty/E_0}}{\tau} \tag{4.2.31}$$

Since $\omega_{\max} = 2\pi v_0/L_0$, the maximum friction occurs at

$$\frac{v_0}{v^*} \approx \sqrt{\frac{E_\infty}{E_0}} \tag{4.2.32}$$

The red line in Figure 4.7 corresponds to the dimensionless sliding velocity at which the loss modulus is maximum.

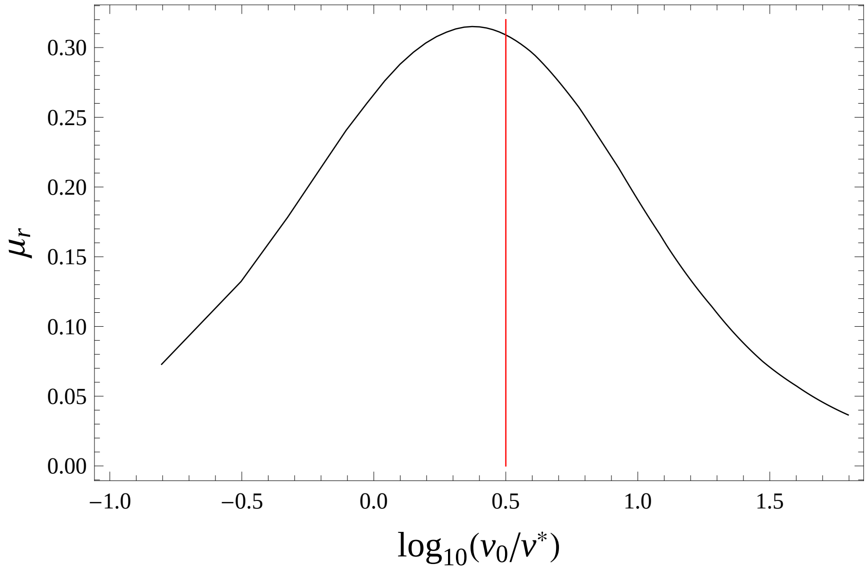

**Figure 4.7:** Micro-rolling friction coefficient as a function of the dimensionless sliding velocity.

# 4.3 Finite deformation model

## 4.3.1 Problem statement

Car tires can be represented by a deformable body undergoing a frictionless contact with a stationary rigid surface which is defined by a sinusoidal analytical function. The sinusoidal analytical function is supposed to represent one of the finite numbers of wavelengths in which the roughness spectrum of a real surface can be decomposed.

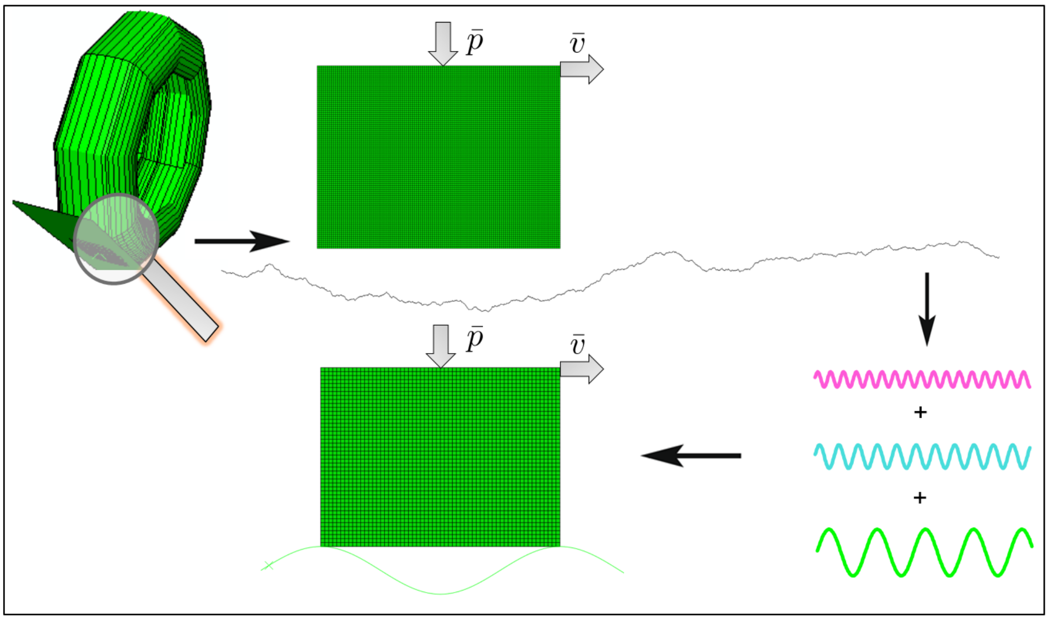

**Figure 4.8:** Macro and micro scales of asphalt specimen.

In order to compute the effective friction coefficient, a micromechanical numerical test is conducted. A rubber test specimen is assumed to be extracted from the boundary layer of the deformable body. Because of the perodic geometry of the surface, one can set the sample width equal to the wavelength of the sinusoidal surface. So, the specimen is considered as a periodic cell extracted from a long boundary layer.

Experimental procedures are mirrored to the micromechanical test. At the beginning, the numerical specimen will be pressed onto the sinusoidal surface with a predetermined normal pressure of absolute value $\bar{p}$ and then dragged over the surface with a specified tangential velocity $\bar{v}$. The micromechanical test is illustrated in Figure (4.9).

The specimen must be statistically representative of the macroscale interface conditions. Since the sample width is fixed to the value of the surface wavelength, the specimen must have sufficient height in order to incorporate the mostly stressed material region, so that the ensuing macroscopic friction coefficient considers the whole

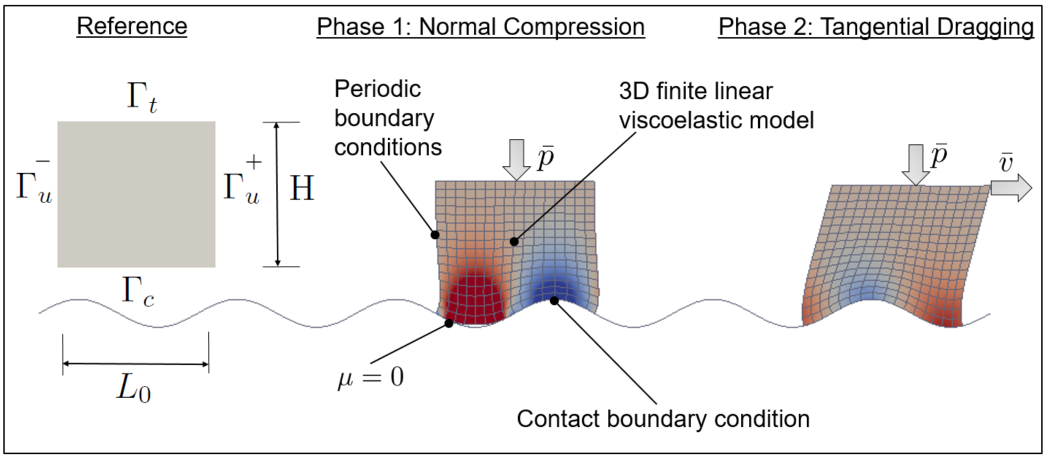

**Figure 4.9:** Micromechanical testing scheme.

amount of energy dissipation taking place at the micro-level. According to De Lorenzis [17], a ratio H/$L_0$=0.75 can be deemed sufficient for all dragging velocities. Thus, this ratio is also adopted in this work.

From numerical standpoint, a sufficiently fine mesh descretization must be guaranteed in order to achieve a satisfactory resolution of the contact area and hence an accurate estimation of the contact stresses. According to De Lorenzis [17], finer resolution leads to a notable decrease in the size of the micro-oscillations and thus to a better iterative convergence behavior.

## 4.3.2 Boundary conditions

The boundary conditions are applied to the lateral, the lower and the upper surfaces of the test specimen, see Figure 4.9. Since the specimen is considered as a periodic cell, periodic boundary conditions are employed on the lateral surfaces $\gamma_u^-$ and $\gamma_u^+$ so that

$$\mathbf{x}^+ - \mathbf{x}^- = \mathcal{F}\left(\mathbf{X}^+ - \mathbf{X}^-\right) \qquad \mathbf{t}^+ = -\mathbf{t}^- \qquad \text{on} \quad \gamma_u^- \cup \gamma_u^+ \tag{4.3.1}$$

where $\mathcal{F}$ is a second order constant tensor and $\gamma$ denotes the boundary $\Gamma$ in the current configuration.

The aforementioned conditions ensure the periodicity of $\mathbf{x}$ and anti-periodicity of $\mathbf{t}$ with reference to confronting lateral surfaces. In the discretized framework, these conditions are applied by direct enforcement of the degrees of freedom of the control nodes on one lateral surface, which are compelled to take the same values of the corresponding ones of the confronting surface. These periodic boundary conditions allow the lateral edges of the rubber sample to be linked. This corresponds to an infinite extension of the sample parallel to the surface.

The lower surface of the specimen undergoes contact constraints with the rigid surface. The contact is enforced using augmented Lagrange multipliers and discretized using surface to surface (STS) discretization, see Subsection 2.3.6.

The upper surface is subjected to the test boundary conditions (the applied pressure $\bar{p}$ and the dragging velocity $\bar{v}$). These conditions must fulfill the micro-macro equality originating from the Hill's energy criterion.

$$\langle \mathbf{t} \rangle_{\gamma_t} \cdot \langle \mathbf{v} \rangle_{\gamma_t} = \langle \mathbf{t} \cdot \mathbf{v} \rangle_{\gamma_t} \tag{4.3.2}$$

The quantities $\bar{\mathbf{t}} = \langle \mathbf{t} \rangle_{\gamma_t}$ and $\bar{\mathbf{v}} = \langle \mathbf{v} \rangle_{\gamma_t}$ are regarded as the macroscopic traction and the macroscopic velocity. In other words. they are considered as macroscopic control parameters of the micromechanical test. Here, $\mathbf{t}$ is the surface traction, $\mathbf{v}$ is the velocity and $\langle \cdot \rangle$ is an averaging operator. It means that in order to fulfill the Hill's criterion, either $\mathbf{t}$ or $\mathbf{v}$ should be specified as constant.

Assuming that $\mathbf{a}^*$ and $\mathbf{n}^*$ are, respectively, the tangent and the normal unit vectors to the surface, the following conditions are applied on $\gamma_t$

- Phase 1 (normal compression)

$$\mathbf{t} \cdot \mathbf{n}^* = \bar{\mathbf{t}} \cdot \mathbf{n}^* = -\bar{p} \qquad \mathbf{x} \cdot \mathbf{a}^* = \mathbf{X} \cdot \mathbf{a}^* \qquad \text{on } \gamma_t \tag{4.3.3}$$

- Phase 2 (tangential dragging)

$$\mathbf{t} \cdot \mathbf{n}^* = \bar{\mathbf{t}} \cdot \mathbf{n}^* = -\bar{p} \qquad \mathbf{v} \cdot \mathbf{a}^* = \bar{\mathbf{v}} \cdot \mathbf{a}^* = \bar{v} \qquad \text{on } \gamma_t \tag{4.3.4}$$

The specimen is first loaded at its upper side by a prescribed vertical pressure $\bar{p}$, which stays constant during the sliding process. During the normal compression phase, the compression time duration $T_1$ controls the speed at which the test specimen is pressed onto the rigid surface. Because of the viscoelastic behavior of the sample, this speed in turn influences the stiffness of the mechanical response during phase 1. Therefore a suitable value of $T_1$ should be chosen.

De Lorenzis [17] stated that the compression time for applying the pressure on the top of the deformable body has a big influence on the oscillations of the resulting friction coefficient. Since the contact area is adjusted in the normal compression phase, a large difference to the stationary contact area during the tangential dragging phase leads to large oscillations. In order to keep the contact area of the compression phase close to the contact area of the dragging phase, De Lorenzis [17] suggested the following equation to evaluate the compression time $T_1$ as a function of the applied velocity $\bar{v}$

$$\sum_{k=1}^{N} E_k e^{-T_1/\tau_k} = \sum_{k=1}^{N} E_k \frac{\bar{\omega}^2 \tau_k^2}{1 + \bar{\omega}^2 \tau_k^2} \tag{4.3.5}$$

with $\bar{\omega} = 2\pi\bar{v}/L_0$. This equation means that the relaxation function of the material evaluated at $T_1$ can be equated to the frequency-dependent storage modulus.

Afterwards, the upper side of the specimen is moved horizontally at constant velocity $\bar{v}$. In the tangential dragging phase, a sufficient dragging distance must be set in order to ensure that the steady-state conditions are matched before the end of the numerical test. De Lorenzis [17] stated that a dragging distance of $12L_0$ is satisfactory. Hence, it is adopted for the range of test variables in this investigation.

### 4.3.3 Material model

As the hysteretic component of rubber friction arises from viscoelastic dissipation in the material bulk, a key ingredient of the numerical model is the viscoelastic constitutive behavior of the rubber. Since the influence of the rheological linearity is investigated, linear viscoelastic material model results are compared to those of a hyper-viscoelastic material model. The detailed description of the used material models is summarized in Section 2.2.3 in Chapter 4.

### 4.3.4 Implementaion in ABAQUS

The commerical FE-software ABAQUS was used for the finite element implementation of the problem. For easier definition of the sinusoidal rigid surface, a keywords version of ABAQUS was used.

The large deformation viscoelastic material model was implemented as user subroutine UMAT within ABAQUS. The periodic boundary conditions are implemented using linear constraint equations.

The weak form of the problem is discretized for the rubber material in ABAQUS using linear four-node elements. The formulation is based on linear shape functions for the displacements. In order to reduce the calculation time, the counter rough rigid surface is discretized in ABAQUS using linear one-dimensional rigid elements.

For the enforcement of contact constrains, the augmented Lagrange multiplier method was used. The lower surface of the rubber respresentative contact element is considered as slave and the road rigid surface takes the role of master. Within ABAQUS, two different contact discretization methods can be selected: node to surface (NTS) or surface to surface (STS) contact elements. As already mentioned in Subsection 2.3.7, NTS contact elements are less stable in the context of large sliding distances and large deformations in the contact zone. Additionally, the contact patch test is not passed by NTS elements and the calculated contact pressure values may be less accurate. As a consequence and in order to ensure stable simulations, the STS contact element is selected for the calculations.

ABAQUS automatically adjusts the time step size and optimizes it by tracking the convergence rate in order to determine when to increase or decrease the time step size.

It reduces the time step size for a slow convergence or divergence behavior and it increases the time step size if fast convergence is met.

As mentioned earlier, computations in this paper are conducted with the assumption of frictionless contact. Since the counter road part is rigid, one can calculate the reaction forces on it in the horizontal and the vertical directions as the horizontal and vertical forces, respectively. Hence one can calculate the friction coefficient.

The projected contact area $A_c$ can be calculated by counting the grid points of the lower surface of the deformable body where the contact pressure is nonzero. Then, based on each contact point, a tributary area can be calculated.

### 4.3.5 Time averaging

The ratio of horizontal and vertical forces yields the mean sliding friction coefficient. The progress of the macroscopic friction coefficient is characterized by a linear increase at the beginning. After passing a maximum value, the macroscopic friction coefficient settles down either to a nearly constant value for small velocities or to a steady oscillation for large velocities.

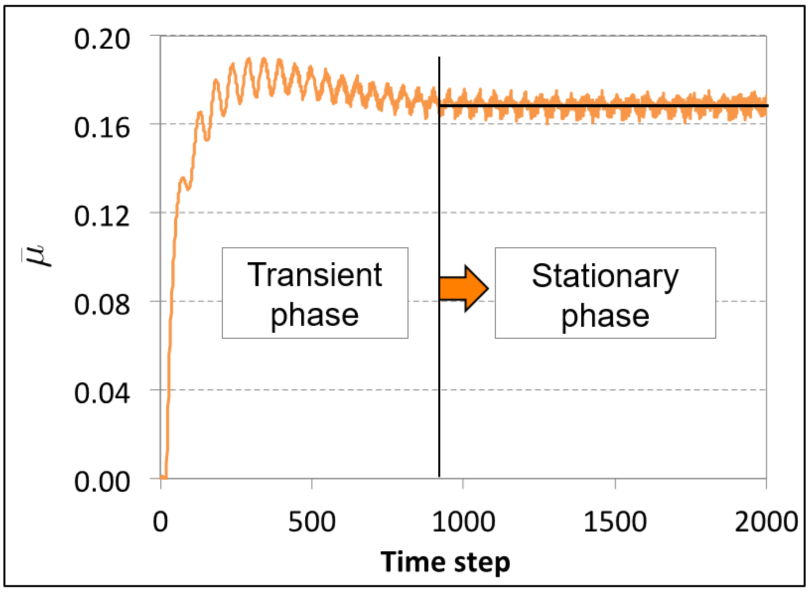

**Figure 4.10:** Time averaging of friction coefficient.

The height of the oscillations depends according to De Lorenzis [17] on several parameters, such as the compression time duration of phase 1 $T_1$, the height of the specimen, the applied pressure $\bar{p}$ and the dragging velocity $\bar{v}$.

In order to extract a single value for the macroscopic friction coefficient from each micromechanical test, time dependency is removed by averaging the friction coefficient over a certain period of time starting from $t_i$ and ending at $t_f$. Denoting with $t_i$ and $t_f$ the initial and final instants of the time averaging period, respectively, and with $\Delta t = t_f - t_i$, the time averaged macroscopic friction coefficient is defined as

$$\mu_{av} = \frac{1}{\Delta t} \int_{t_i}^{t_f} \mu\,(t) dt \tag{4.3.6}$$

Time averaging is a common technique in multiscale contact homogenization approaches. It has been applied by many authors [17, 113, 118, 20].

## 4.4 Comparison between approaches

In this section, the effect of the rheology, kinematics and roughness mean square slope on the friction coefficient and contact area will be studied by comparing the viscoelastic half-space linear model in Section 4.2 with the non-linear model in Section 4.3.

Three cases will be discussed:
(i) linear rheology, linear kinematics and small-slope roughness (VHS model);
(ii) linear rheology and non-linear kinematics (FE model);
(iii) non-linear rheology and non-linear kinematics (the neo-Hookean rubber description is adopted in the FE model).

In this comparison, $L_0$ is set equal to $(2\pi/300)10^{-3}$ m, whereas the adopted aspect ratios $\Delta/L_0$ and the corresponding root mean square slopes $m_2$ are summarized in Table 4.1. A generalized Maxwell model with six Maxwell elements is considered. The corresponding data for an unfilled styrene butadiene rubber can be seen in Table 2.1 in Chapter 2. The loss tangent maximum occurs in correpondence of a time scale $\tau_m = 2\pi/\omega_{\max} \approx 1.97 \cdot 10^{-4}$ $[s]$.

Dimensional analysis is adopted as a tool to evaluate the minimum number of independent parameters which influence the friction coefficient. Therefore, a dimensionless number, called Deborah number $D_h$, is used to characterize the viscoelasticity of the material. It is defined as the ratio of the relaxation time $\tau_m$, and the characteristic time scale of an experiment (or a computer simulation) related to the response of the material $T$. It can be written as:

$$D_h = \frac{\tau_m}{T} = \frac{v \cdot \tau_m}{L_0} \tag{4.4.1}$$

**Table 4.1:** Investigated root mean square slopes

| $\Delta/L_0$ | 0.10 | 0.13 | 0.20 | 0.28 | 0.50 |
|---|---|---|---|---|---|
| $m_2$ | 0.44 | 0.59 | 0.89 | 1.3 | 2.2 |

### 4.4.1 Influence of geometrical non-linearity on calculation of the friction coefficient

Figures 4.11 and 4.12 show the micro-rolling friction coefficient $\mu_r$ as a function of the Deborah number at constant imposed pressure $\bar{p}$= 2[MPa] for the aspect ratios given in Table 4.1. The red dots represents the FE model employing the linear and the non-linear rheology in Figures 4.11 and 4.12, respectively, while the black dots mark the VHS model.

The variation of the micro-rolling friction coefficient as a function of Deborah number exhibits the well-known behavior observed in experiments with a bell-shape distribution and a maximum value in the viscoelastic transition zone. For very low dragging velocities (the rubbery region), the material remains fully relaxed and hence displays a purely elastic response. For very high dragging velocities (the glassy region), the material has no time to relax and therefore shows a stiffer elastic response. In both cases, the friction coefficient tends to zero as the elastic response leads to no energy dissipation. In the intermediate range of dragging velocities (the glassy-to-rubbery region), viscoelastic energy dissipation occurs and a maximum value can be observed.

In Figure 4.11, curves for largest root mean square slopes are not illustrated, because of iterative convergence issues in the FE model. In the non-linear case (Figure 4.12), the agreement in terms of micro-friction coefficient is good for both methods except for the largest adopted value of the root mean square slope ($m_2$=2.2).

For small values of $m_2$, the linear VHS model shows an underestimation of the friction coefficient relative to the non-linear neo-Hookean FE model. This can ascribed to the higher compliance (tangential stiffness) of the neo-Hookean material with respect to the linear elastic rheology, leading to an increased bulk dissipation.

For values of $m_2$ larger than 1, the deviation between the approaches becomes quite large, as the deformation regime induced by large $m_2$ significantly deviates from the small displacement assumption and thus the effect of the non-linearity comes into play.

### 4.4.2 Influence of geometrical non-linearity on calculation of contact area

The projected contact area $A_\mathrm{c}$ can be calculated by counting the grid points where $t_\mathrm{N} > 0$, and assigning to each grid point a tributary area.

Figures 4.13 and 4.14 illustrate the variation of the normalized projected contact area

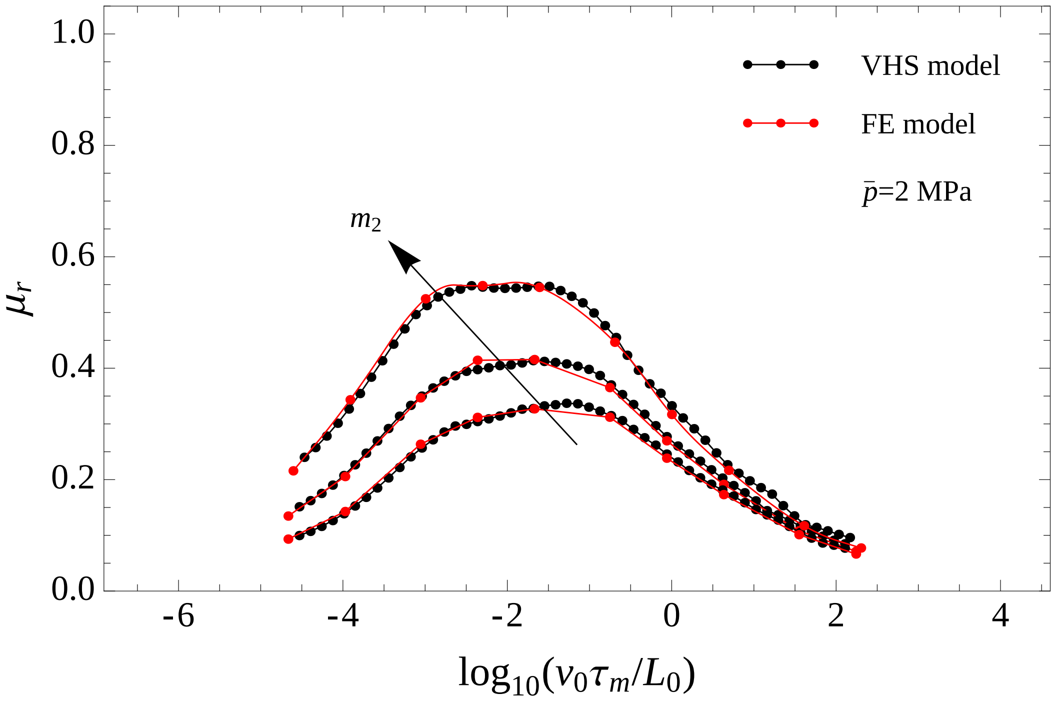

**Figure 4.11:** Micro-rolling friction as a function of Deborah number at constant pressure $\bar{p} = 2$ [MPa] using FE model employing linear rheology compared to VHS theory.

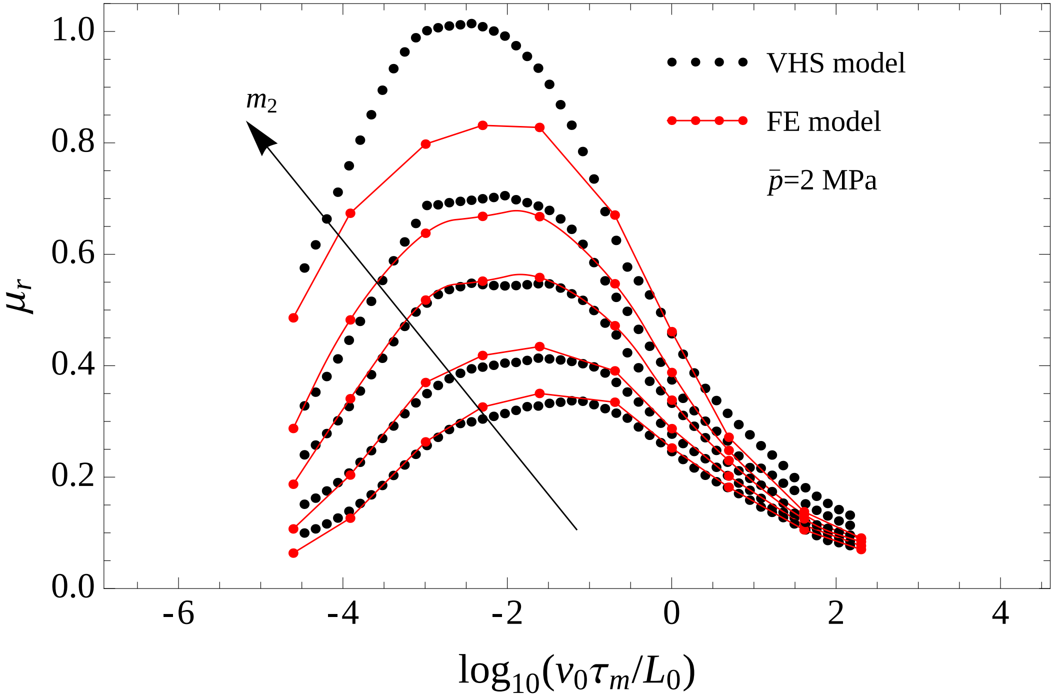

**Figure 4.12:** Micro-rolling friction as a function of Deborah number at constant pressure $\bar{p} = 2$ [MPa] using FE model employing neo-Hookean rheology compared to VHS theory.

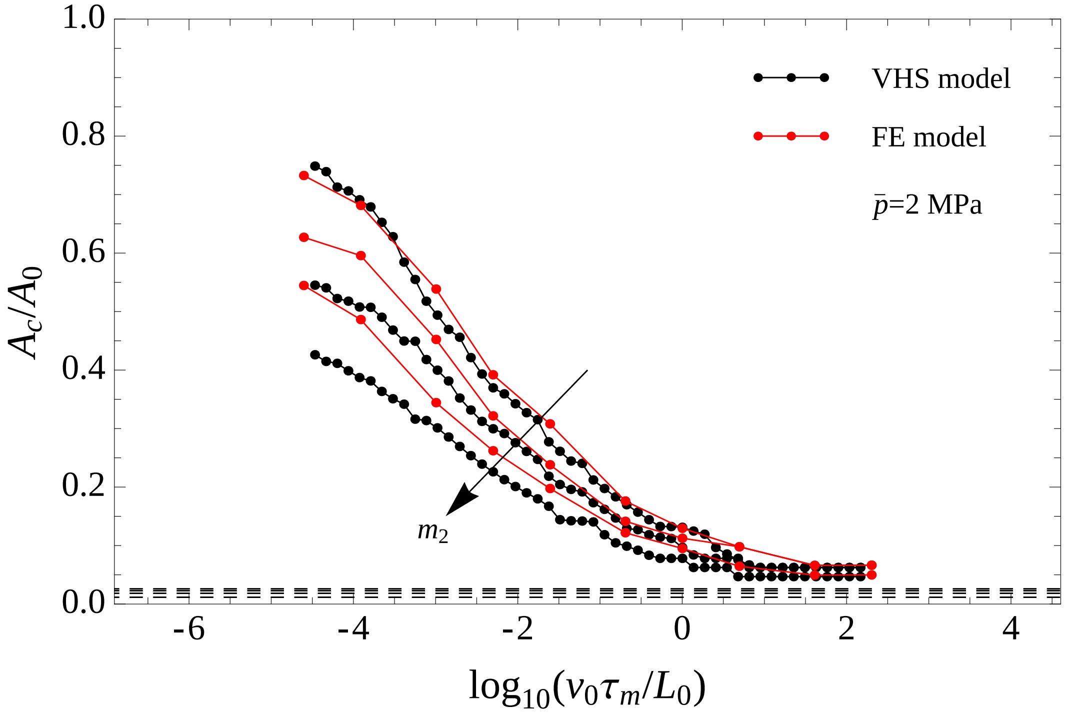

**Figure 4.13:** Normalized contact area as a function of Deborah number at constant pressure $\bar{p} = 2$ [MPa] using FE model employing linear rheology compared to VHS theory.

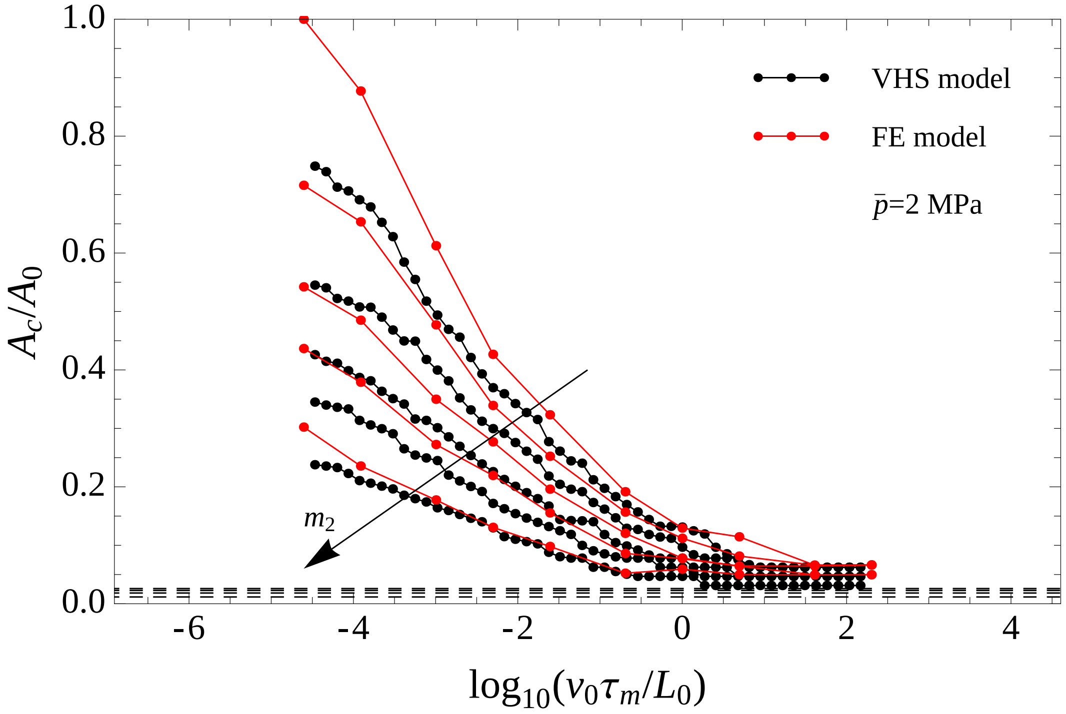

**Figure 4.14:** Normalized contact area as a function of Deborah number at constant pressure $\bar{p} = 2$ [MPa] using FE model employing neo-Hookean rheology compared to VHS theory.

$A_c/A_0$ with Deborah number at constant prescribed pressure. The same notation as in Figures 4.11 and 4.12 is used.

For the lowest range of velocities, the material reacts deformably and the contact area fraction is high. As the velocity increases, the contact area decreases gradually due to the increasingly stiff response of the material. For very large velocities, the contact area is expected to tend asymptotically to the value that would be obtained in small strain conditions for an elastic material with an elastic response with modulus $E_0$. These asymptotic values, calculated with the Hertz theory [31], are reported as dashlines in Figure 4.13, see Section 2.5.

For the linear rheology FE model illustrated in Figure 4.13, the predictions obtained for small $m_2$ are in good agreement with the VHS results, independent of the dragging velocity. Nevertheless, one can observe from the figure that increasing the roughness aspect ratio causes an increase of the contact area with respect to VHS predictions. This is expected as the locally applied contact pressure in the FE model is increased by a factor $\approx \cos(\theta)^{-1}$ with respect to the VHS model, where $\theta$ is the angle between the local surface normal vector and the external normal load direction. Therefore, this first-order geometric non-linearity causes the resulting increase of the contact area, which is consistent with other studies [2].

Figure 4.14 shows the effect of including the nonlinear rheology in the FE calculation. In this case, the larger compliance of the neo-Hookean rheology with respect to the linear viscoelastic case results in a larger contact area even for the smallest adopted $m_2$ value. Increasing $m_2$ determines a reduction of the deviation between the VHS and FE results, even for large $m_2$ asperities where the first-order geometric non-linearity effects appear.

The large slope asperities are expected to be dominated by a second-order geometric non-linearity effect, which is related to the curvature of the local asperity and hence to its bending energy. The bending energy deformation mode can only be simulated in the FE model, while it is neglected in the VHS model. Therefore, in the VHS model, the energy required to fill a deep $m_2$ asperity is underestimated in terms of deformation modes (the curvature-related bending energy is neglected), whereas it is overestimated as a result of the adopted linear rheological model and of the (neglected) first-order non-linearity effect. Another interesting point is that the aforementioned effects compensate each other at large $m_2$ asperities. Furthermore, these effects are rapidly reduced at relatively large dragging velocities $\bar{v}$. By increasing the dragging velocity, the rubber viscoelastic modulus increases, resulting in the reduction of the contact area. Therefore, the contact takes place on the top of the asperity, where the geometric non-linearities discussed above can be neglected.

### 4.4.3 Influence of geometrical non-linearity on estimation of contact pressure and separation fields

Figures 4.15 and 4.16 show, respectively, the contact pressure and the contact separation field for the $m_2$=2.2 case, as calculated from the VHS (black dots) and FE (red dots) model at imposed pressure $\bar{p}$=2 [MPa]. Three velocities have been selected, belonging to the rubbery, rubbery-to-glassy, and the glassy regions. The rubbery region is distinguished by the smallest dragging velocity and thus the largest contact area, while the glassy region is characterized by the largest sliding speed and the smallest contact area. One can obeserve that the FE contact pressure curve shows some oscillations in the rubbery-glassy transition zone. These oscillations are spurious and can be removed either by reducing the mesh size or by decreasing the Poisson's ratio.

In Figures 4.17 and 4.19 [4.18 and 4.20] one can see, respetively, the contact pressure [separation] field for the FE model employing linear or non-linear neo-Hookean rheology (red dots). The black dots are from the VHS contact model. The applied pressure is $\bar{p}$=2 [MPa], and $m_2$=0.44. One can observe that both linear and non-linear rheology FE models show, albeit small, quantitative differences with respect to the VHS results, especially in the glassy-to-rubbery region. However, the corresponding micro-rolling friction remains nearly unaffected. So, a remarkable agreement between FE and VHS can be seen.

This is confirmed by Figure 4.21, which shows the micro-rolling friction coefficient as a function of the normalized imposed pressure $\bar{p}/E_{0r}$ for $m_2$=0.44 and for a sliding velocity belonging to the rubbery-to-glassy transition rubber region. The red curve is for the neo-Hookean FE model, while the black one is from the VHS model. One can see comparable results over the whole range of applied pressures, which extend from the small contact area regime up to values close to full contact.

## 4.5 Conclusions

In summary, one can conclude that the contact area is much more sensitive to the geometrical and rheological nonlinearities than the rolling friction coefficient. The friction coefficient, as shown in Figures 4.11 and 4.12 seems to be insensitive to geometrical and rheological non-linearities except for mean slopes larger than one.

The small deformation and the small root mean square slope assumptions in the linear viscoelastic model lead to quantitative deviations from the results obtained with a non-linear finite element description in terms of contact area fraction and local contact pressure distribution. However, the agreement between the results in terms of the rolling friction coefficient is remarkably good, except for root mean square slopes larger than 1.

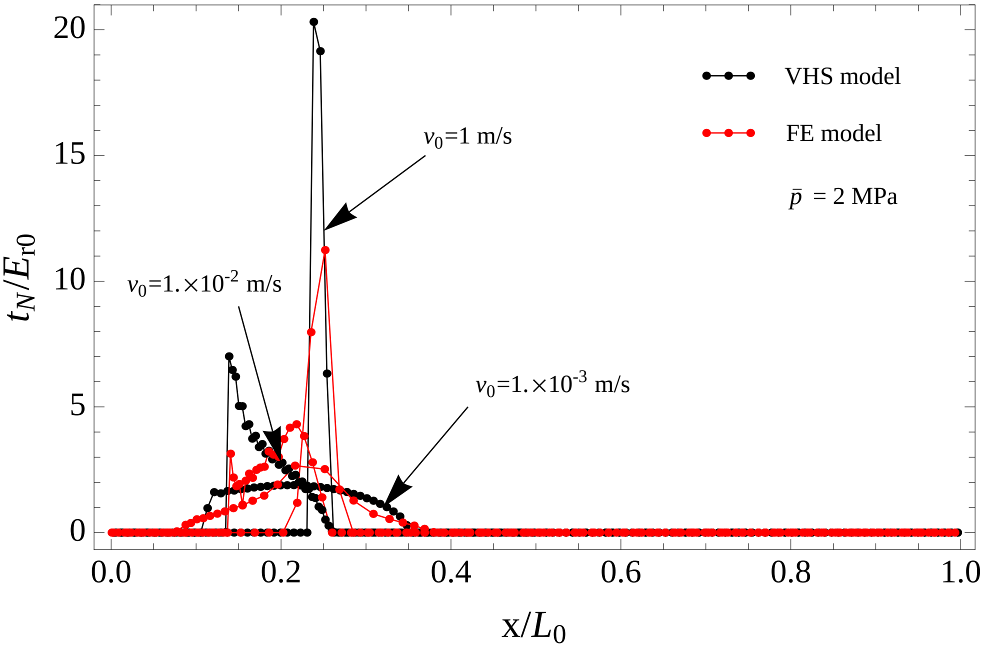

**Figure 4.15:** Dimensionless contact pressure as a function of the dimensionless contact position for $m_2$=2.2, using FE model employing neo-Hookean rheology, compared to VHS theory.

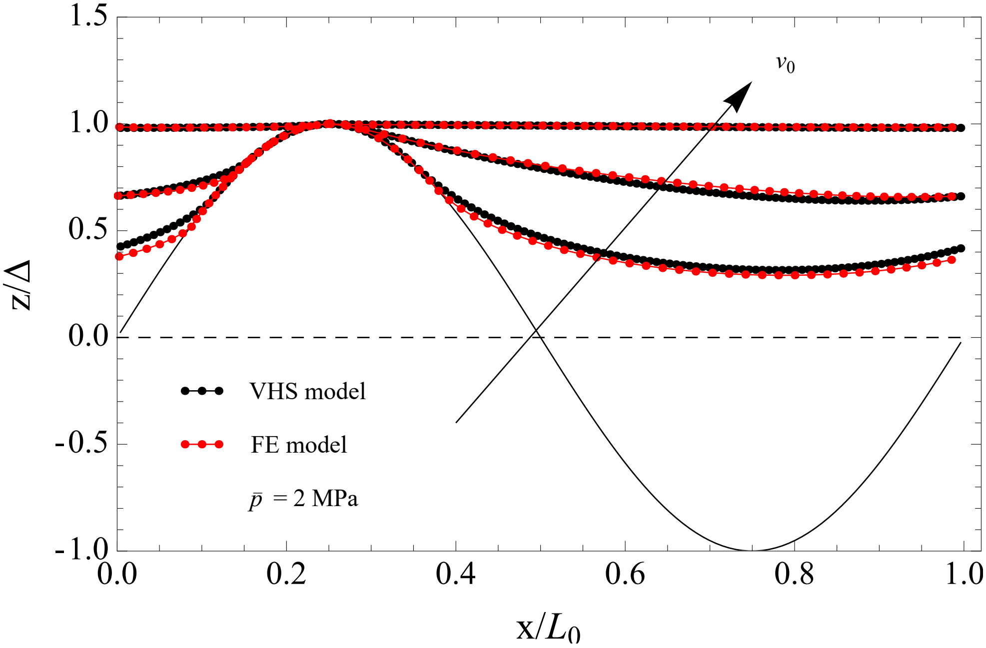

**Figure 4.16:** Dimensionless deformed rubber profile as a function of the dimensionless contact position for $m_2$=2.2, using FE model employing neo-Hookean rheology, compared to VHS theory.

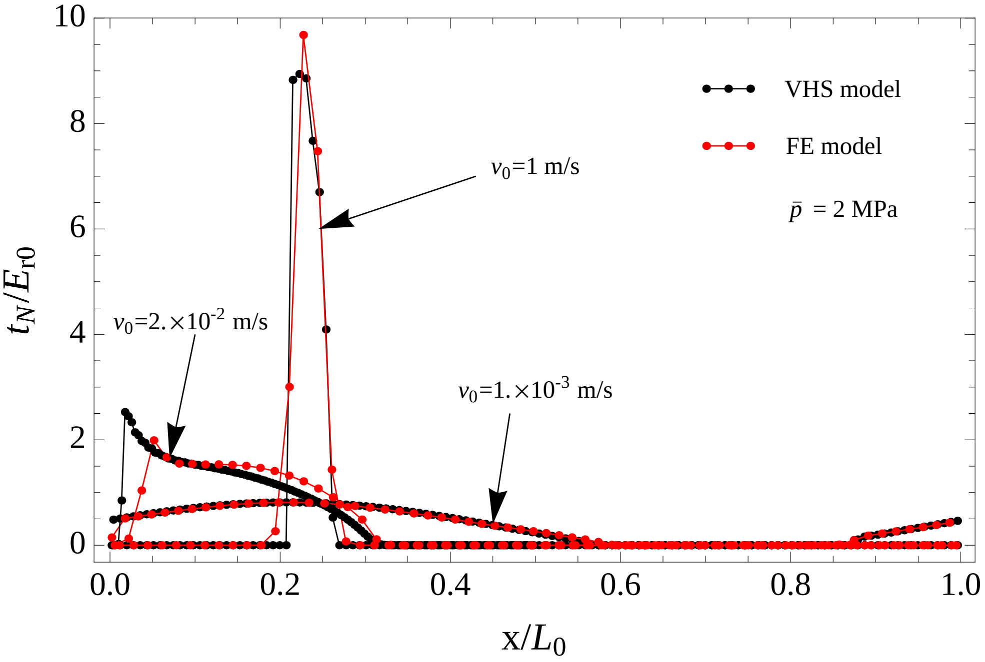

**Figure 4.17:** Dimensionless contact pressure as a function of the dimensionless contact position for $m_2$=0.44, using FE model employing linear rheology, compared to VHS theory.

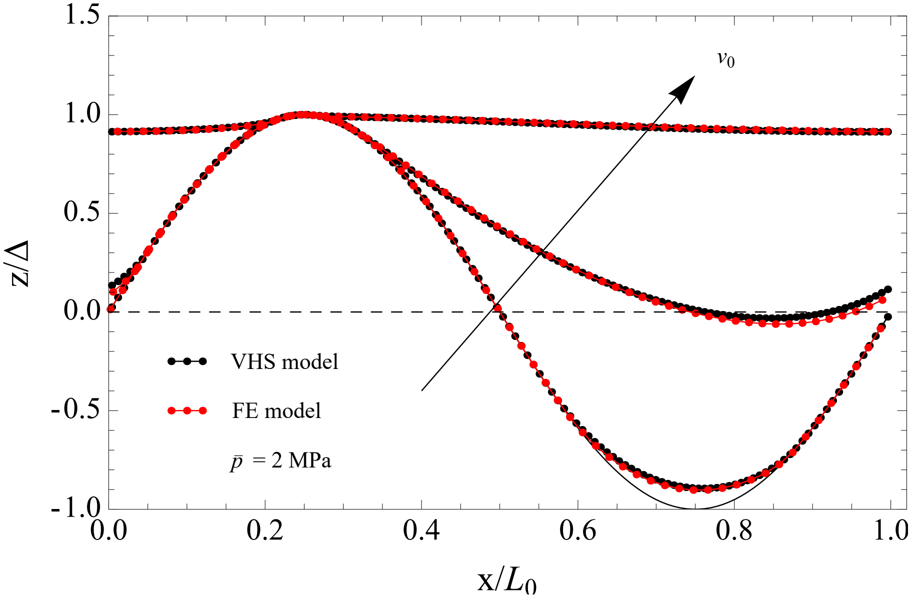

**Figure 4.18:** Dimensionless deformed rubber profile as a function of the dimensionless contact position for $m_2$=0.44, using FE model employing linear rheology, compared to VHS theory.

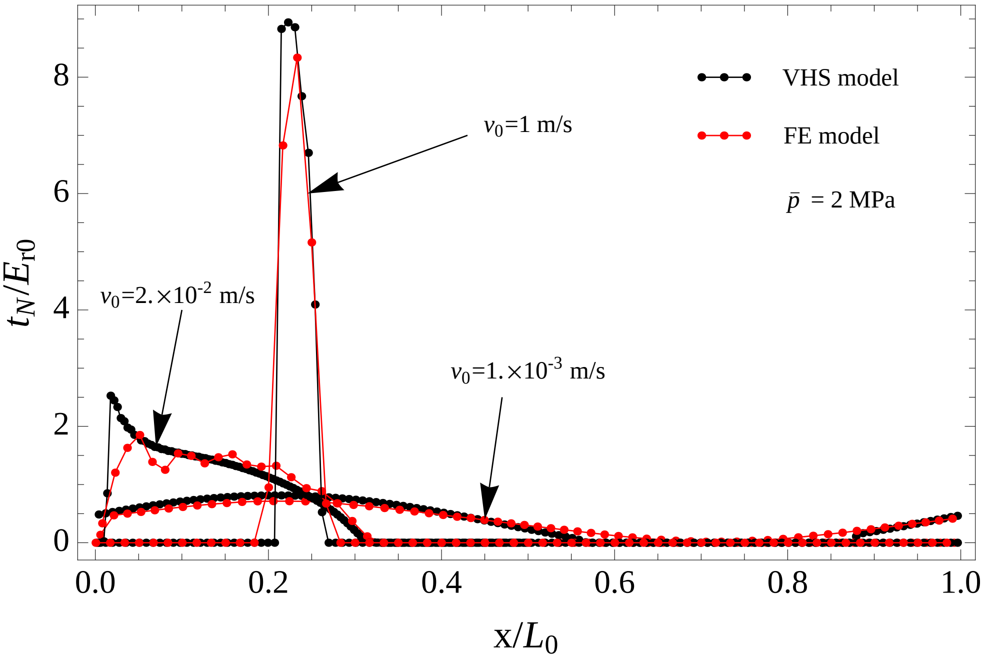

**Figure 4.19:** Dimensionless contact pressure as a function of the dimensionless contact position for $m_2$=0.44, using FE model employing neo-Hookean rheology, compared to VHS theory.

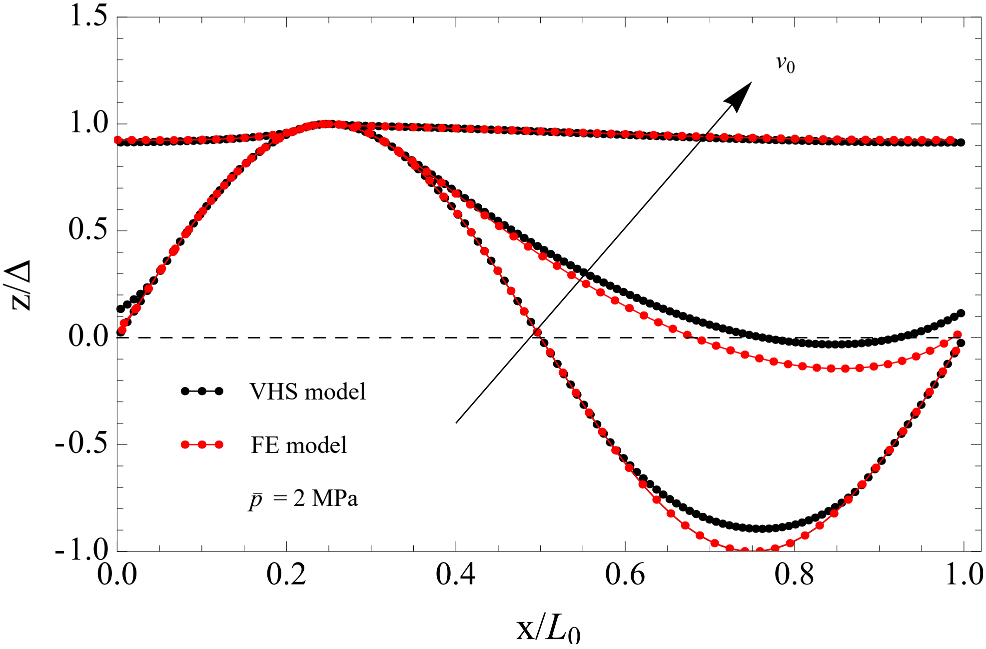

**Figure 4.20:** Dimensionless deformed rubber profile as a function of the dimensionless contact position for $m_2$=0.44, using FE model employing neo-Hookean rheology, compared to VHS theory.

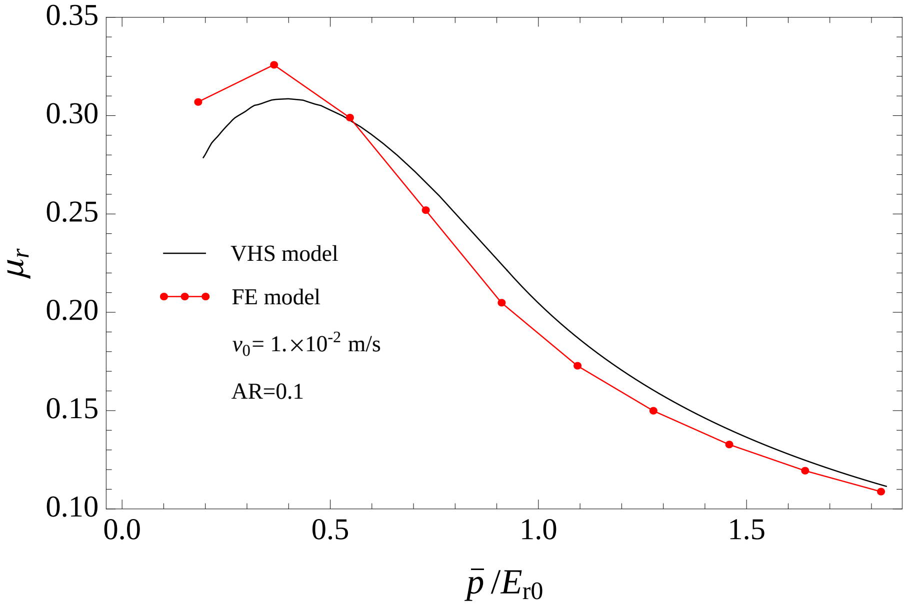

**Figure 4.21:** Micro rolling friction as a function of the dimensionless average contact pressure for $m_2$=0.44 corresponding to aspect ratio $\Delta/L_0 = 0.1$ using FE model employing neo-Hookean rheology compared to VHS theory.

Therefore, this study confirms that friction coefficient predictions within a reasonable degree of accuracy can be obtained using the linear viscoelastic models under the assumption that the roughness features moderate values of root mean square slopes (lower than 1), while more accurate but computationally expensive finite element computations must be adopted for large root mean square slopes (larger than 1). This conclusion will be exploited in a novel multiscale approach, which will be explained in detail in Chapter 5.

# Chapter 5

# Hybrid multiscale approach to rubber friction

Despite the rapidly increasing capabilites of computers during the last decade, the computational cost to solve the problem of a car tire sliding on road surfaces is extremely expensive since the roughness includes a wide range of length scales, which requires extremely small mesh size. Moreover, high non-linearity resulting from the contact conditions in addition to large deformations all affect the convergence rate. Hence, it is necessary to use a multiscale approach in order to predict the frictional behavior.

Starting from the conclusion of Chapter 4 that the VHS-based boundary elements approach provides quantitatively accurate results for roughness mean square slopes smaller than 1, a new hybrid (FEM/BEM) multiscale approach is established in this chapter. The multiscale approach is based on the decomposition of the measured roughness into a finite number of sinusoidal functions by fitting their sum of height difference correlation functions to the height difference correlation function of the measured roughness, see Section 3.3.

In the hybrid multiscale approach, the micro-rolling friction coefficient is calculated initially based on linear VHS-based model as a predictor. Then, the amount of correction is computed for length scales that have large mean square slopes based on the difference of the calculated friction coefficients using the VHS-based model and the finite deformation model at theses length scales. This allows an efficient approach for computing friction coefficients.

## 5.1 Principle of the hybrid multiscale approach

The multiscale approach focuses on the behavior of the micro scale and its influence on an overlaying macroscopic scale. The hybrid multiscale approach is applied using the following steps:
1) As an initial step, the friction coefficient is calculated using the VHS-based model as a predictor, $\mu_{init}$.

2) Subsequently, a frictionless contact is simulated at the smallest length scale, where a large mean square slope (larger than 1) was observed in Tables 3.1 and 3.2. The simulation should be performed using the VHS-based model on one hand, and the finite deformation model on the other hand. For each applied squeezing pressure $p_i$, an average separation $\bar{u}_i$, a micro-rolling friction coefficient calculated based on the VHS-based model $\mu_{BEM,i}$ and a micro-rolling friction coefficient calculated based on the finite deformation model $\mu_{FEM,i}$ are extracted. The geometry of the separation is shown in Figure 5.1.

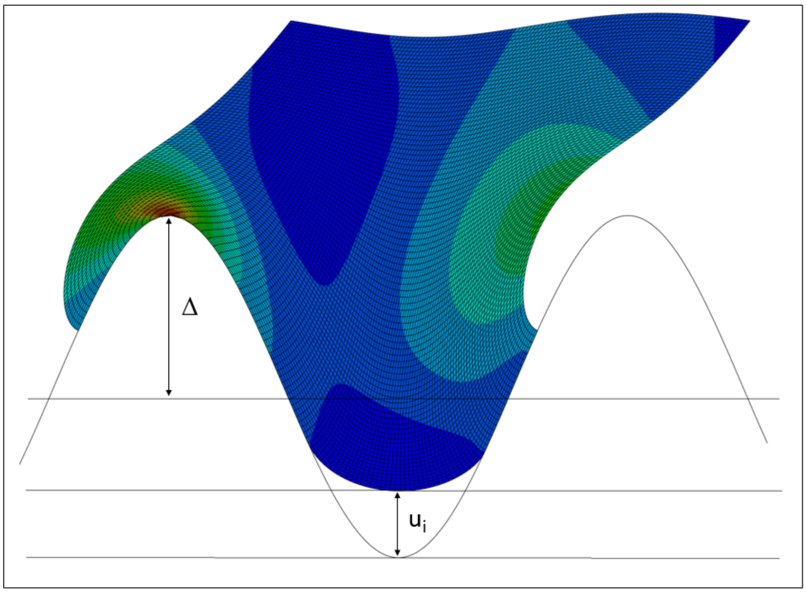

**Figure 5.1:** Separation of the node i

3) The behavior of the microscale as computed in step 2 is condensed in as a local repulsive law between the applied pressure and the average separation. At higher applied pressure, the average separation is lower. This repulsive law is transferred into the macroscales (the scales that have small mean square slops less than 1) as an input to project the microscale contribution into the macroscales and it controls the deformation behavior of the rubber according to the applied pressure. This will result in a contact pressure field $p_i$.
An example of the repulsive law for two different sliding velocities is illustrated in Figure 5.2.

4) The amount of correction in the micro-rolling friction coefficient is calculated from the difference of the micro-rolling friction coefficients resulting from the VHS-based model and the finite deformation model.

$$\Delta\mu_i = \mu_{FEM,i} - \mu_{BEM,i} \tag{5.1.1}$$

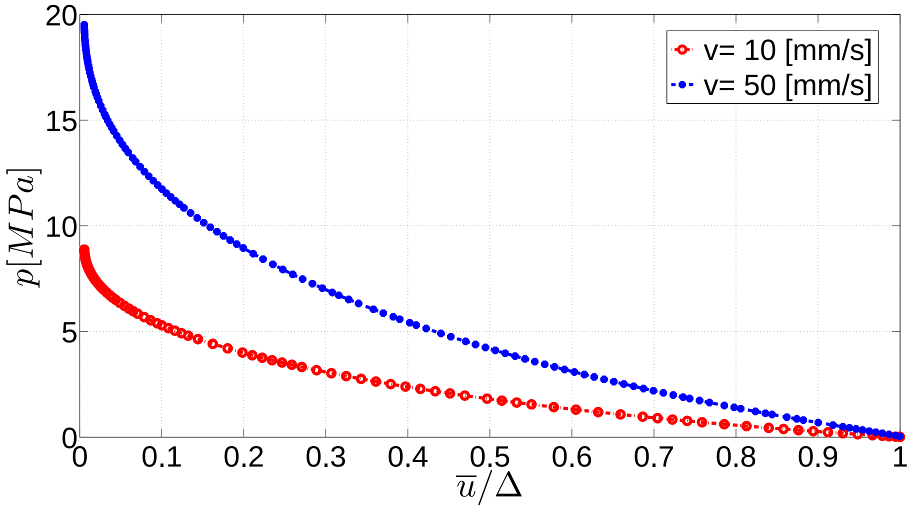

**Figure 5.2:** Repulsive law between the applied pressure and the average separation for the smallest length scale at velocities of 10 and 50 [mm/s].

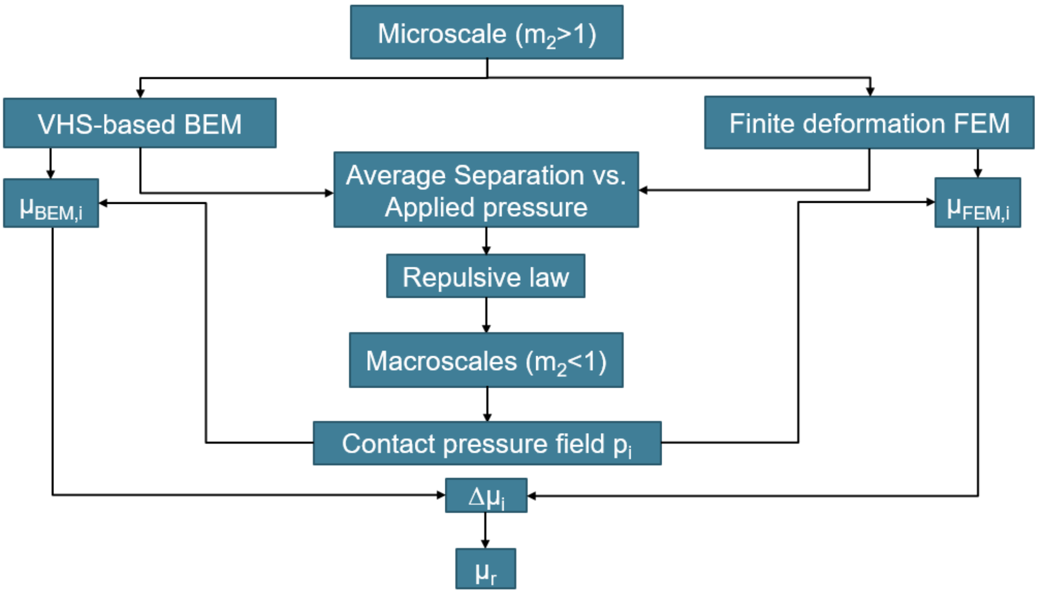

**Figure 5.3:** Algorithm of the hybrid multiscale approach

Then, it is added to the value of the initial predictor to calculate the micro-rolling friction coefficient $\mu_r$.

$$\mu_r = \mu_{init} + \frac{1}{M}\sum_{i=1}^{M} \Delta\mu_i \tag{5.1.2}$$

where $M$ is number of contact points. The flow chart of the hybrid multiscale approach is represented in Figure 5.3.

## 5.2 Sensitivity to the number of superimposed sinusoidal waves

Since small-scale wavelengths have a major role in rubber friction [86, 92, 118], it is important to investigate the friction coefficient sensitivity to the selection of the number of superimposed sinusoidal waves. Two different approximations consisting of different numbers of superimposed sinusoidal waves will be taken into account. The first one consists of 8 superimposed sinusoidal waves and the second one consists of 9 superimposed sinusoidal waves. Since the measured track is perfectly approximated with 8 and 9 sine functions, there will be no need to use more sine functions to approximate the road track, while using less than 8 sinusoids gives a lower accuracy in the surface approximation. The amplitudes and the wavelengths are summarized in Tables 3.1 and 3.2 in Chapter 3.

A random phase angle between the superimposed sinusoidal waves is considered so that different realizations of the measured surface are generated. Five different realizations are taken for each case, see Figures 5.4 and 5.5. The resulting surface for each realization is assumed to be Gaussian. Finally, the friction coefficients are averaged and compared to each other, see Tables 5.1 and 5.2 for a velocity of 10 [mm/s]. The bold numbers in the tables denote the maximum friction coefficient values.

The comparison is done with a varying applied pressures at two different sliding velocities: 10 and 50 mm/s, belonging to the rubbery region and the maximum dissipation region, respectively, see Figures 5.6 and 5.7.

The relative error average in the micro-rolling friction coefficient is estimated as follows

$$e\,[\%] = \frac{1}{K}\sum_{i=1}^{K} \frac{|\mu_{a,i} - \mu_{b,i}|}{\mu_{b,i}} * 100 \tag{5.2.1}$$

where $e$ is the relative error average, $K$ is number of points ranging from a normalized contact area of 0.01 to 0.1 with a step size of 0.01. $\mu_{a,i}$ is the micro-rolling friction coefficient calculated using 8 sine waves to approximate the surface, while $\mu_{b,i}$ represents the micro-rolling friction coefficient calculated using 9 sine waves to approximate the surface.

The averaged values show comparable results in terms of friction coefficient. The error

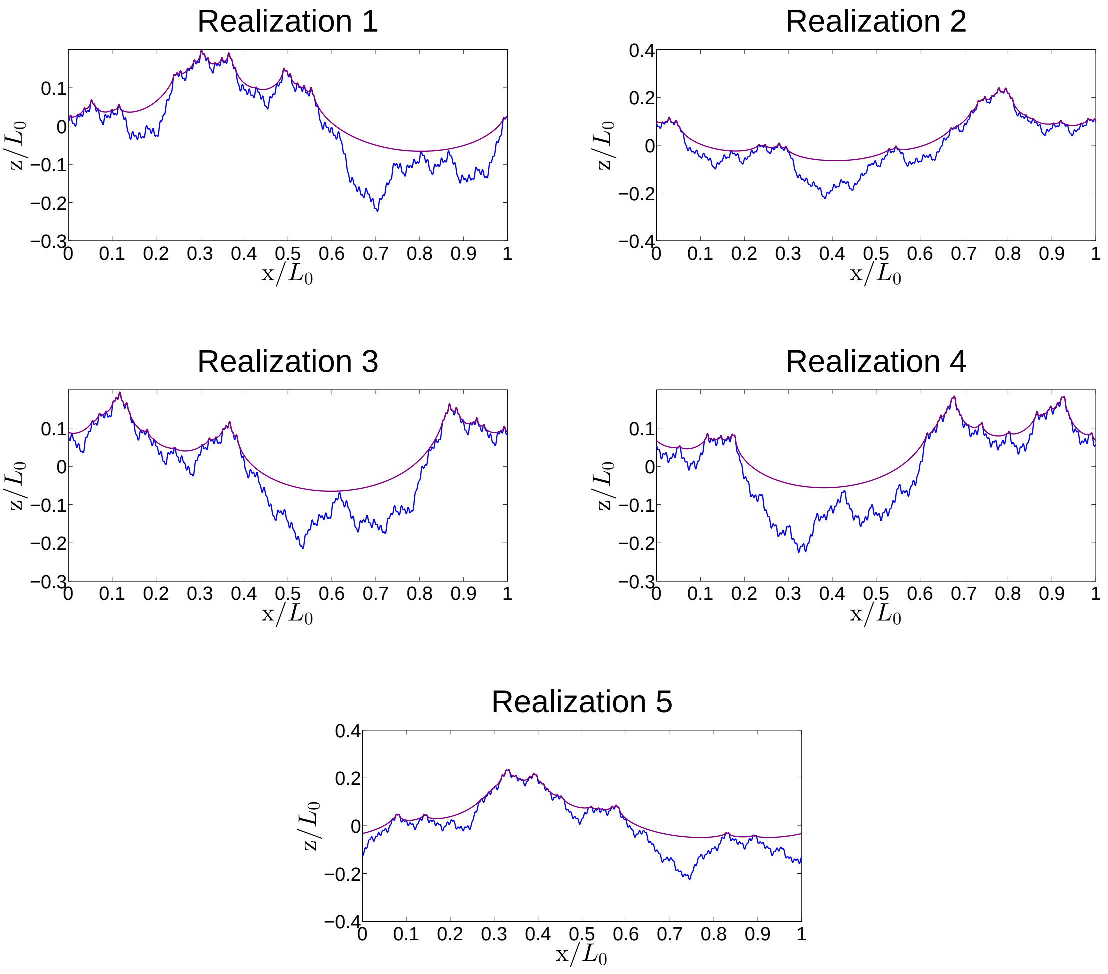

Realization 1

Realization 2

Realization 3

Realization 4

Realization 5

**Figure 5.4:** Realizations for superposition of 8 sinusoidal waves.

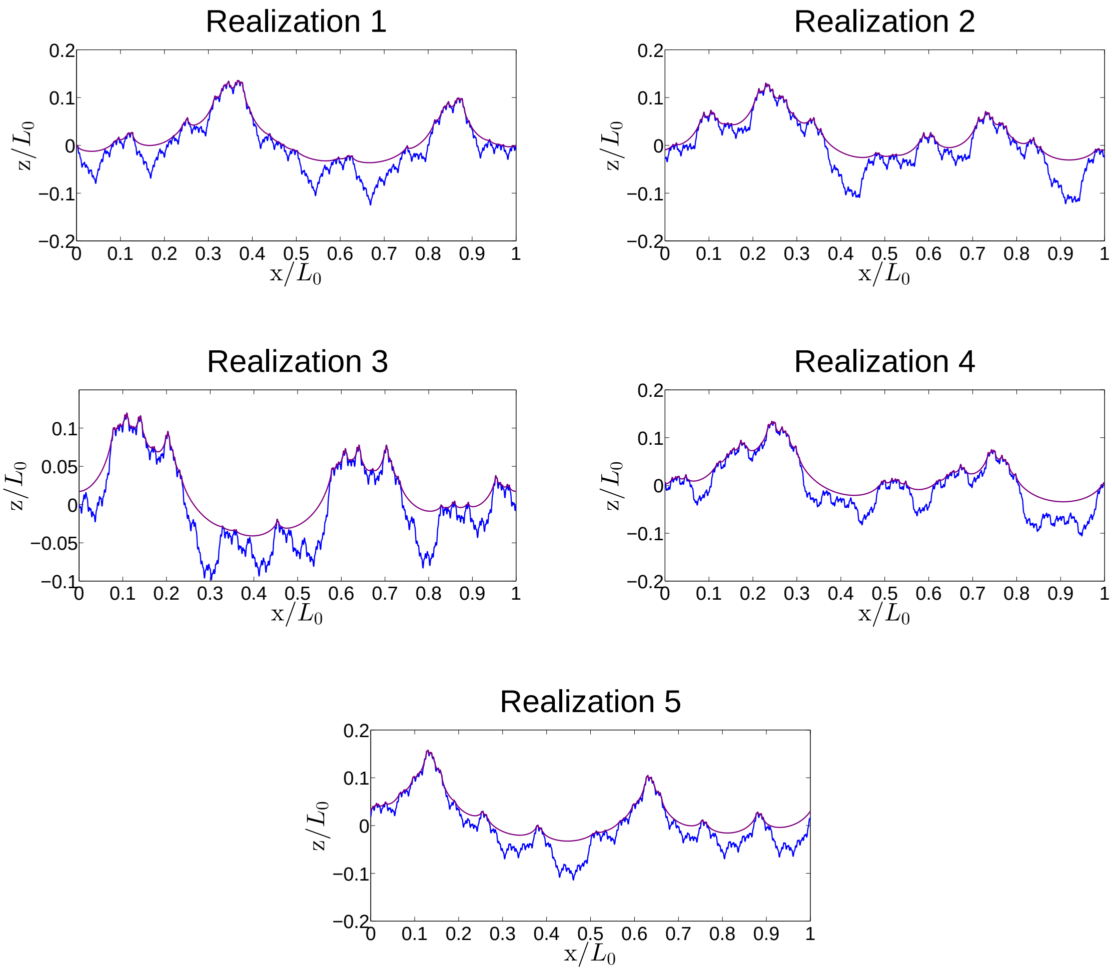

**Figure 5.5:** Realizations for superposition of 9 sinusoidal waves.

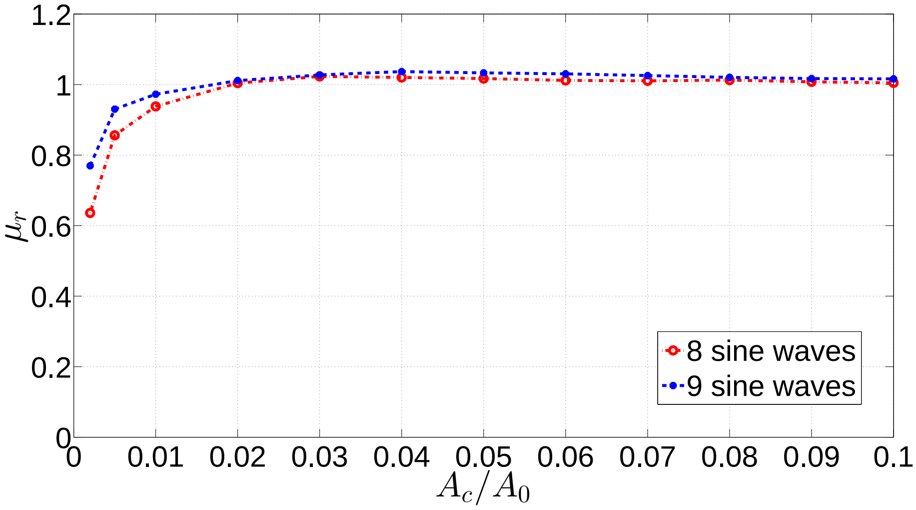

**Figure 5.6:** Comparison of friction coefficient using VHS-based BE approach at a velocity of 10 mm/s using different number of sine waves to approximate the surface.

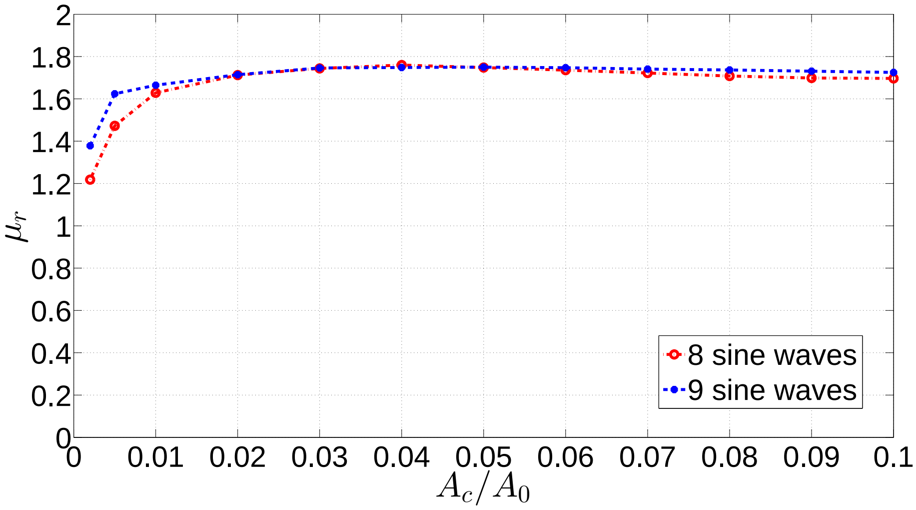

**Figure 5.7:** Comparison of friction coefficient using VHS-based BE approach at a velocity of 50 mm/s using different number of sine waves to approximate the surface.

**Table 5.1:** Averaged micro-rolling friction coefficient calculated using VHS-based BEM for a measured surface approximated by 8 superimposed sinusoidal waves and a velocity of 10 mm/s.

| | **Friction coefficient for realization #** | | | | | |
|---|---|---|---|---|---|---|
| $A_c/A_0$ | **1** | **2** | **3** | **4** | **5** | **Avg** |
| 0.002 | 0.70099 | 0.53646 | 1.11166 | 0.40200 | 0.42895 | 0.63601 |
| 0.005 | 0.85334 | 0.81127 | 1.15151 | 0.74896 | 0.71634 | 0.85628 |
| 0.01 | 0.88905 | 0.95564 | 1.16447 | 0.89442 | 0.78765 | 0.93825 |
| 0.02 | 0.94566 | 1.02248 | 1.16428 | 0.99161 | 0.89696 | 1.00420 |
| 0.03 | 0.95591 | 1.03794 | **1.17878** | 1.01493 | 0.92815 | **1.02315** |
| 0.04 | 0.96250 | 1.05073 | 1.13973 | 1.01517 | **0.93308** | 1.02024 |
| 0.05 | 0.98236 | 1.05029 | 1.11494 | **1.03281** | 0.90510 | 1.01710 |
| 0.06 | 0.98745 | 1.06041 | 1.08713 | 1.03158 | 0.89307 | 1.01193 |
| 0.07 | 0.99219 | **1.06119** | 1.08505 | 1.02368 | 0.89152 | 1.01072 |
| 0.08 | 1.00497 | 1.05913 | 1.08008 | 1.02807 | 0.89194 | 1.01284 |
| 0.09 | 1.00990 | 1.04772 | 1.06412 | 1.02824 | 0.88980 | 1.00796 |
| 0.1 | **1.01151** | 1.04459 | 1.05118 | 1.02583 | 0.89183 | 1.00499 |

**Table 5.2:** Averaged micro-rolling friction coefficient calculated using hybrid multiscale approach for a measured surface approximated by 8 superimposed sinusoidal waves and a velocity of 10 mm/s.

| | **Friction coefficient for realization #** | | | | | |
|---|---|---|---|---|---|---|
| $A_c/A_0$ | **1** | **2** | **3** | **4** | **5** | **Avg** |
| 0.002 | 0.63607 | 0.82234 | 0.81251 | 0.70867 | 0.86938 | 0.76979 |
| 0.005 | 0.82447 | 1.06663 | 0.94304 | 0.92268 | 0.89487 | 0.93034 |
| 0.01 | 0.85618 | 1.09059 | 0.94377 | 1.01123 | 0.96118 | 0.97259 |
| 0.02 | 0.93616 | 1.13011 | 0.94720 | 1.05071 | **0.99236** | 1.01131 |
| 0.03 | 0.97843 | 1.13484 | 0.96406 | 1.07030 | 0.98917 | 1.02736 |
| 0.04 | 0.99717 | 1.16281 | **0.97499** | **1.07567** | 0.97388 | **1.03690** |
| 0.05 | 1.00398 | **1.17346** | 0.97146 | 1.05695 | 0.96046 | 1.03326 |
| 0.06 | **1.00921** | 1.17215 | 0.97361 | 1.04725 | 0.94999 | 1.03044 |
| 0.07 | 0.99871 | 1.16371 | 0.96931 | 1.04915 | 0.94724 | 1.02562 |
| 0.08 | 0.98781 | 1.15340 | 0.96025 | 1.05250 | 0.94920 | 1.02063 |
| 0.09 | 0.98578 | 1.14208 | 0.95359 | 1.05758 | 0.94647 | 1.01710 |
| 0.1 | 0.98460 | 1.13824 | 0.95492 | 1.06037 | 0.94352 | 1.01633 |

is estimated at 1.38 % for a velocity of 10 mm/s and at 1 % for a velocity of 50 mm/s. One can conclude that, as the smallest wavelength scale and the RMS height are kept the same and the upper cut-off covers the physics of the measured road track roughness, the friction coefficient is not sensitive to the number of superimposed sinusoidal waves used to approximate the surface.

## 5.3 Results of the hybrid multiscale approach

### 5.3.1 Results on microscale

The microscale results are derived on the smallest scale of the approximation using 8 superimposed sine functions , i.e. the wavelength is 0.0625 [mm] with an amplitude of 0.01867 [mm]. The mean square slope roughness is 1.3275, see Table 3.1 in Chapter 3.

Figure 5.8 shows the micro-rolling friction as a function of the applied pressure for the smallest scale and a sliding velocity of 10 [mm/s] belonging to the rubbery region. The blue curve is for the finite deformation model, while the red one is from the VHS-based model.

One can observe that for very small applied pressure values, the VHS-based model slightly underestimates the friction coefficient compared to the finite deformation model. This can be justified by the fact that at very small applied pressures, the contact occurs only at the top of the asperity, so the geometric nonlinearity can be neglected.

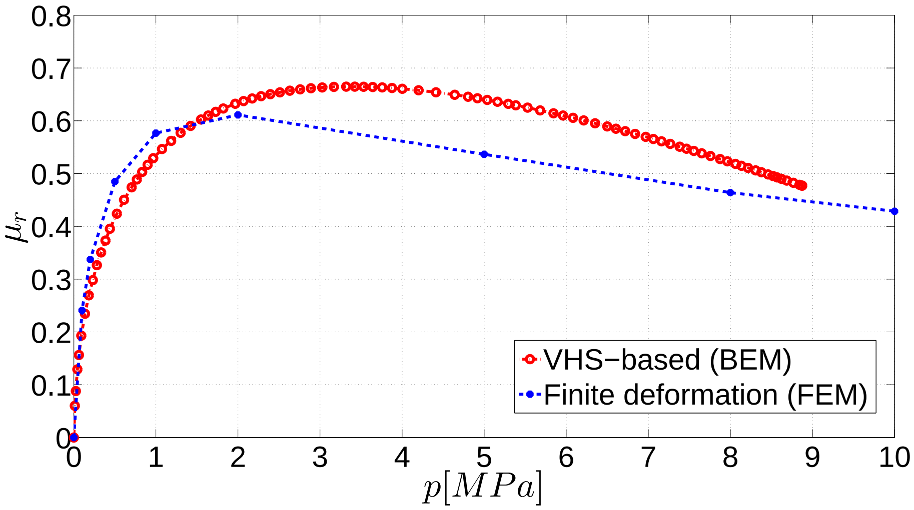

**Figure 5.8:** Friction coefficient versus applied pressure for the smallest wavelength at a velocity of 10 mm/s.

A decreasing friction coefficient for high pressure values is observed for both approaches. This is expected since an increasing pressure leads to higher normal forces whereas the tangential forces stemming from the hysteresis friction are not increasing in the same manner. One can note that for higher applied pressures, the difference between the approaches becomes larger, as the deformation regime induced by large mean square slope roughness significantly deviates from the small displacement assumption and thus the effect of the nonlinearity comes into play.

Figure 5.9 shows the micro-rolling friction coefficient as a function of the applied pressure for the smallest scale and a sliding velocity of 50 [mm/s] belonging to the maximum dissipation region. One can observe similar trends as in Figure 5.8 with a higher maximum friction value and a shift towards larger pressures. The deviation between the finite deformation model and the VHS-based model is extremely large in this case.

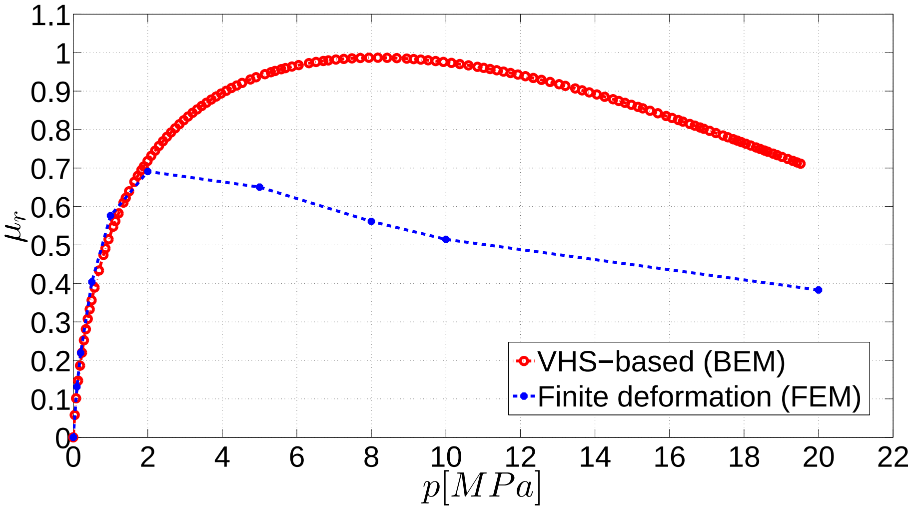

**Figure 5.9:** Friction coefficient versus applied pressure for the smallest wavelength at a velocity of 50 mm/s.

### 5.3.2 Macroscopic results

The results on larger scales are now calculated using the repulsive law deduced from the microscale, which is shown in Figure 5.2. Figures 5.10 and 5.11 show examples of the contact pressure field as a function of the dimensioness contact position for one of the realizations with dragging velocities of 10 mm/s and 50 mm/s, respectively. It should be noted that according to these contact pressures, the corresponding micro-rolling friction coefficients at the contact points are approximated using the results of the friction coefficients at the smallest scale, which are shown in Figures 5.8 and 5.9.

Figures 5.12 and 5.13 show the friction coefficient as a function of the normalized contact area calculated using the multiscale hybrid method for velocities belonging to the rubbery region and the maximum dissipation region, respectively.

The curves show a non-monotonic behavior, where friction increases at small values of contact area. For high enough loads the friction coefficient decreases slightly with increasing load (corresponding to increasing contact area) and the numerical results smoothly converge to the mean field predictions.

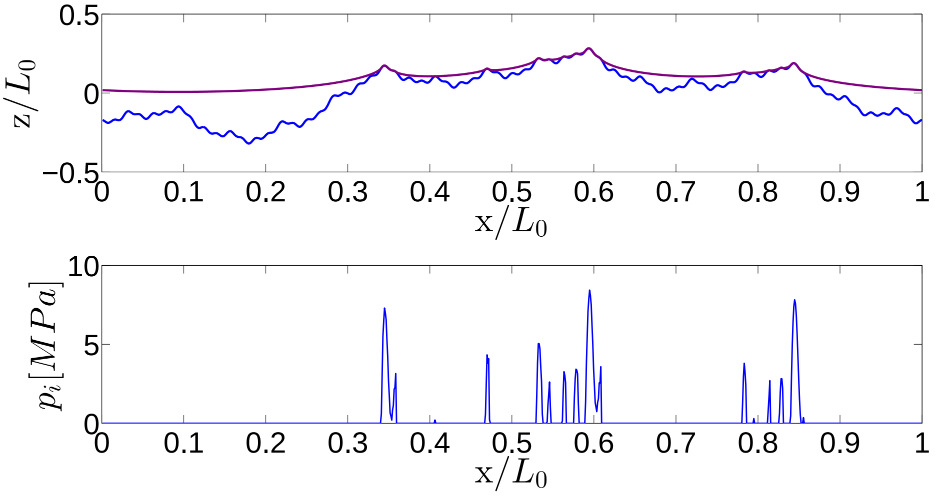

**Figure 5.10:** Contact pressure distribution resulting from the repulsive law as a function of the dimensioness contact position for a sliding velocity of 10 mm/s.

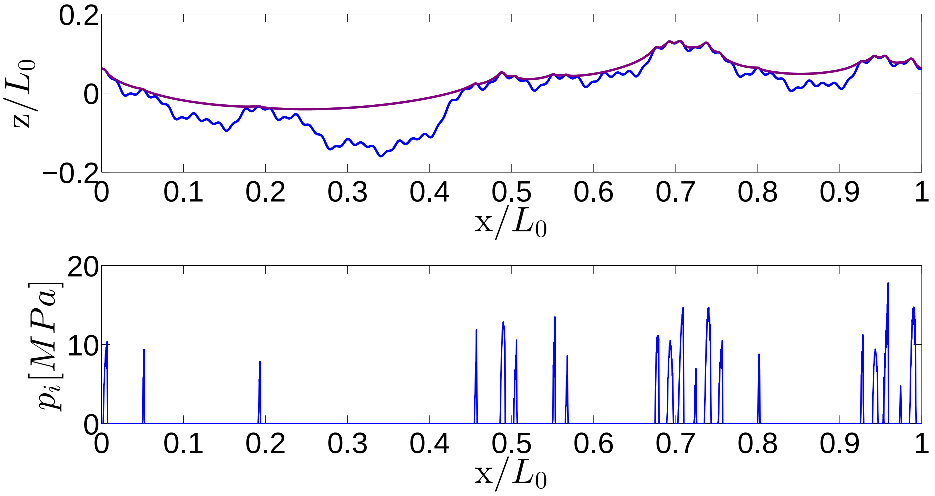

**Figure 5.11:** Contact pressure distribution resulting from the repulsive law as a function of the dimensioness contact position for a sliding velocity of 50 mm/s.

**Table 5.3:** Example of how the correlation of the micro-rolling fricition coefficient is calculated from the pressure distribution resulting from the repulsive law at a velocity of 10 mm/s.

| $p_i[MPa]$ | $\mu_{FEM,i}$ | $\mu_{BEM,i}$ | $\Delta\mu_i$ |
|---|---|---|---|
| 8.46180 | 0.45575 | 0.49823 | -0.04248 |
| 8.07463 | 0.46260 | 0.51772 | -0.05511 |
| 8.00526 | 0.46383 | 0.52114 | -0.05731 |
| 7.68399 | 0.47157 | 0.53675 | -0.06518 |
| 7.36913 | 0.47918 | 0.55154 | -0.07235 |
| 6.59313 | 0.49795 | 0.58548 | -0.08752 |
| 6.22233 | 0.50692 | 0.60025 | -0.09332 |
| 6.05398 | 0.51100 | 0.60659 | -0.09559 |
| 5.26714 | 0.53003 | 0.63293 | -0.10290 |
| 4.64028 | 0.54544 | 0.64927 | -0.10383 |
| 3.30858 | 0.57856 | 0.66455 | -0.08599 |
| 3.24604 | 0.58012 | 0.66438 | -0.08426 |
| 1.75708 | 0.60273 | 0.61885 | -0.01611 |
| 0.86548 | 0.55191 | 0.50974 | 0.04216 |
| **Avg** | **0.51697** | **0.58267** | **-0.06570** |

One can observe also that the multiscale approach is not sensitive to the selection of the number of superimposed sinusoidal waves as the lower cut-off and the RMS height are kept the same and the upper cut-off covers the details of the measured road track roughness. The averaged values of the hybrid multiscale method show comparable results in terms of friction coefficient. The relative error average, which is calculated from equation (5.2.1), is estimated at 1 % for a velocity of 10 mm/s and at 1.7 % for a velocity of 50 mm/s.

However, all the curves show a remarkable difference at very small contact areas. This can be justified by the fact that at relatively small values of contact area, the number of contact patches is typically limited by the finite size effect. The latter is related to the inability of a numerical simulation done with a finite roughness realization to provide enough statistical content in term of contact patches (thus poor contact pressure statistics) and roughness heights statistics. On the other hand, at smaller contact areas the contact patch is of order of the mesh resolution. As a consequence, the contact zone area must be meshed finer, though decreasing the mesh size will affect the computation time [85].

Figures 5.14 and 5.15 illustrate the amount of correlation between the initially predicted micro-rolling friction coefficient which is calculated using VHS-based model and the corrected micro-rolling friction coefficient which is calculted using the hybrid approach for two different velocities belonging to the rubbery and the glassy to rubbery

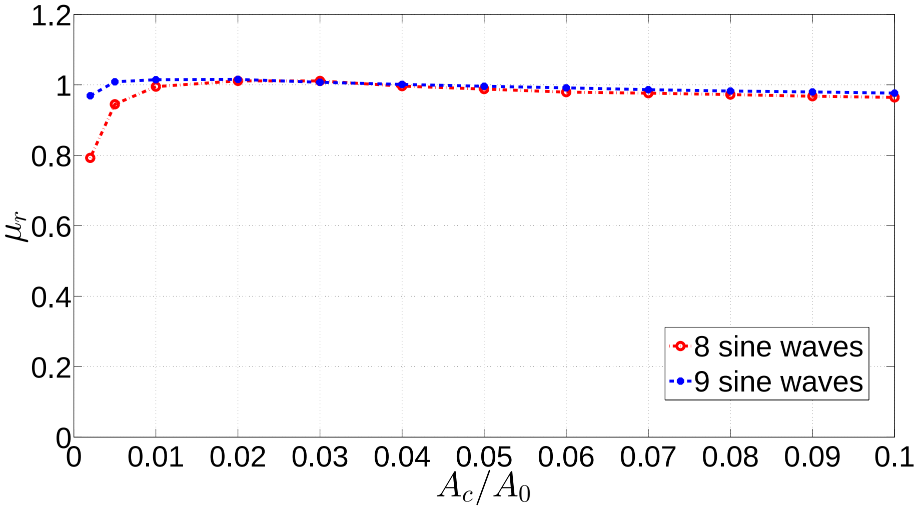

**Figure 5.12:** Comparison of friction coefficient as a function of the normalized contact area using hybrid multiscale approach for both surface approximations at a velocity of 10 [mm/s].

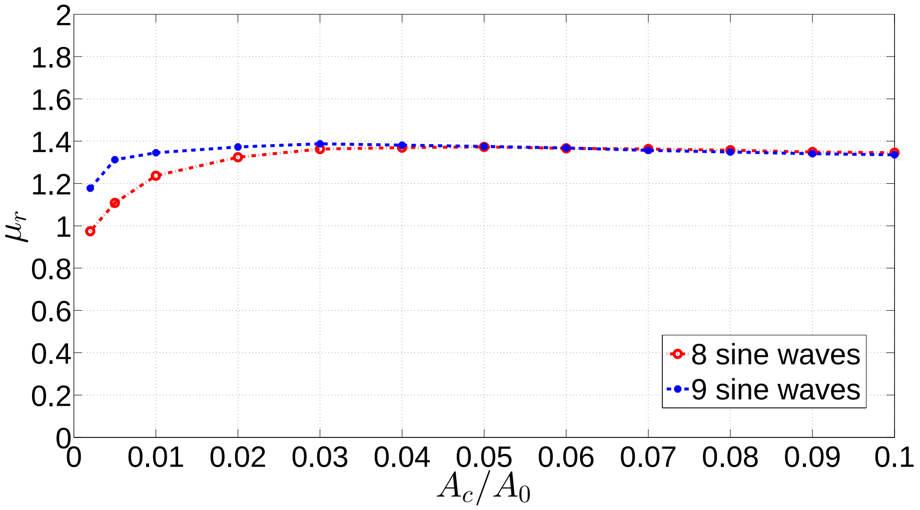

**Figure 5.13:** Comparison of friction coefficient as a function of the normalized contact area using hybrid multiscale approach for both surface approximations at a velocity of 50 [mm/s].

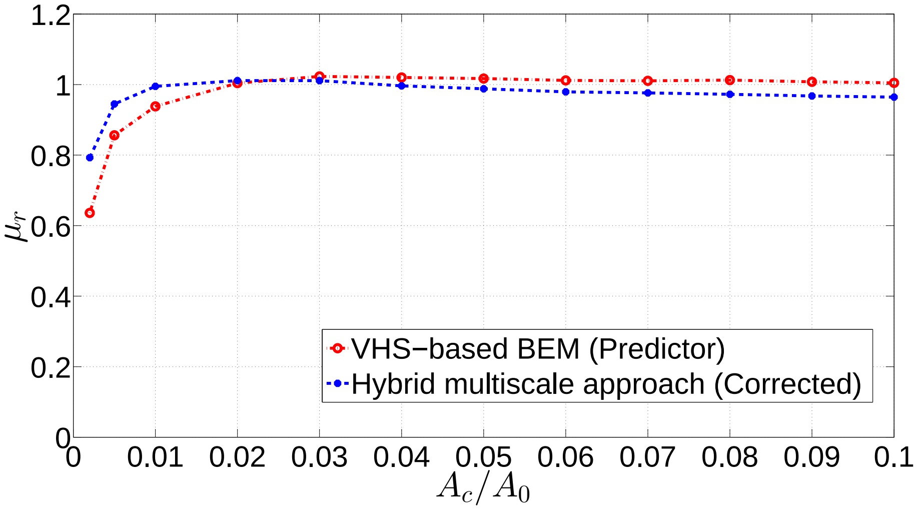

**Figure 5.14:** Amount of correction in the micro-rolling friction coefficient for a velocity of 10 mm/s.

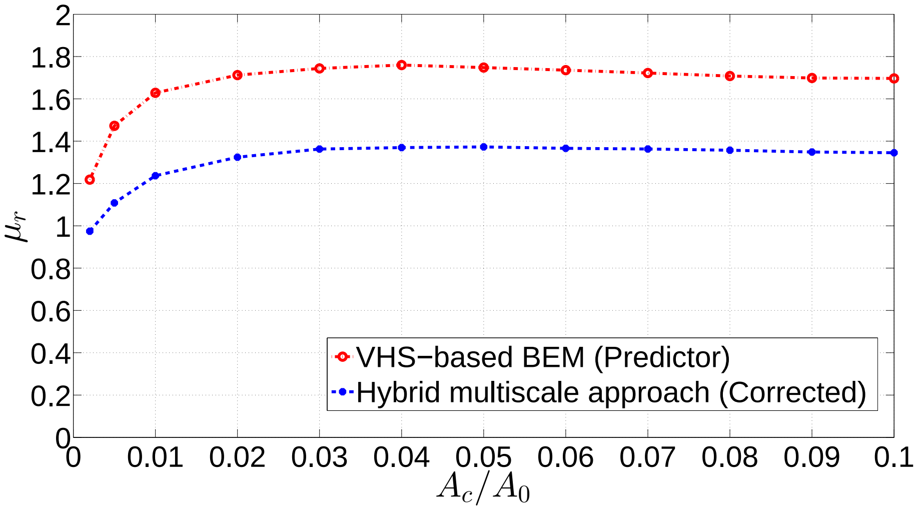

**Figure 5.15:** Amount of correction in the micro-rolling friction coefficient for a velocity of 50 mm/s.

regions.

The amount of correlation in the micro-rolling friction coefficient is consistent with results in the Figures 5.8 and 5.9. For a low dragging velocity of 10 mm/s, the amount of correlation in the micro-rolling friction coefficient between the initially predicted VHS-based model and the correlated hybrid multiscale approach is relatively small. This can be justified by the fact that for low sliding velocities, the local contact pressures are more evenly distributed and they are small, see Figure 5.10. And for small pressures, the results of the finite deformation model and the VHS-based model are comparable, see Figure 5.8. However, for a dragging velocity of 50 [mm/s], the amount of correlation is large, this can be ascribed to the difference in the irregular distribution of the contact pressures at larger dragging velocities and the large contact pressures resulting, see Figure 5.11. The effect of the nonlinearity is remarkable, see Figure 5.9.

## 5.4 Numerical verification of the hybrid multiscale approach

In this section, the performance of the proposed hybrid multiscale method is illustrated by means of a simple example. An artificial surface with a microscopic and macroscopic contribution is considered. Three sinusoidal functions are superimposed and can easily be split for the multiscale method into a macro and a micro part. The micro part has a mean square slope larger than one, while the macro part includes the length scales that have a mean square slope less than one. Five different realizations of the artificial surface are taken into account by assuming a random phase angle between the superimposed sine functions. Then the friction coefficient is averaged, see Tables A.7 to A.12 in the Appendix.

The superimposed artificial surface contains a macroscopic and microscopic part:

$$\mathrm{z_{full}}\left(\mathrm{x}\right) = \mathrm{z_{micro}}\left(\mathrm{x}\right) + \mathrm{z_{macro}}\left(\mathrm{x}\right) \tag{5.4.1}$$

with the dimensions (all in mm):

$$\mathrm{z_{micro}}\left(\mathrm{x}\right) = 0.01867 \cdot \sin\left(\frac{2\pi}{0.0625}\mathrm{x}\right) \tag{5.4.2}$$

$$\mathrm{z_{macro}}\left(\mathrm{x}\right) = 0.02648 \cdot \sin\left(\frac{2\pi}{0.125}\mathrm{x}\right) + 0.02939 \cdot \sin\left(\frac{2\pi}{0.25}\mathrm{x}\right) \tag{5.4.3}$$

The considered scales in this case are the first three scales in table 3.1, where the microscale has been already calculated before, see Figures 5.2, 5.8, and 5.9.

In order to verify the hybrid multiscale approach, calculations on the artificial (full) surface using finite deformation model and using the proposed hybrid multiscale method are compared to each other. The comparison is done for a velocity of 10 mm/s belonging to the rubbery region and for a velocity of 50 mm/s belonging to the glassy to rubbery region.

The relative error average in the micro-rolling friction coefficient is estimated as follows

$$e\,[\%] = \frac{1}{K}\sum_{i=1}^{K}\frac{|\mu_{FE,i} - \mu_{Hybrid,i}|}{\mu_{FE,i}} * 100 \tag{5.4.4}$$

where $e$ is the relative error average, $K$ is number of points ranging from a normalized contact area of 0.01 to 0.1 with a step size of 0.01. $\mu_{FE,i}$ is the micro-rolling friction coefficient calculated using the finite deformation model, while $\mu_{Hybrid,i}$ represents the micro-rolling friction coefficient calculated using the hybrid multiscale method.

Figures 5.16 and 5.17 show a comparison between all investigated approaches, i.e. VHS-based BEM that is used as a predictor, finite deformation FEM that is used as a benchmark, and the hybrid multiscale approach, for a velocity belonging to the rubbery and the glassy to rubbery regions, respectively. The comparison is done in terms of micro-rolling friction coefficient as a function of the normalized contact area. This comparison between the hybrid approach and the nonlinear FEM approach is done in order to verify the accuracy of the hybrid multiscale approach.

The averaged values shows a small deviation between the approaches. The relative error average, which is calculated from equation (5.4.4), is estimated at 2.9 % for a velocity of 10 mm/s and at 7.1 % for a velocity of 50 mm/s. At relatively small values of contact area, the deviation between the approaches is relatively large, where the hybrid multiscale approach underestimates the micro-rolling friction coefficient even more than the VHS-based BEM approach.

This can be justified by the fact that the hybrid multiscale approach depends strongly on the contact pressure distribution to calculate the micro-rolling friction coefficient, and at relatively small values of contact areas, the number of contact patches is typically limited by the finite size effect. The latter is related to the inability of a numerical simulation to provide enough statistical content in terms of contact patches which result in poor contact pressure statistics at very small values of contact area. One can note that when the contact area increases, the amount of the difference between the approaches decreases and the agreement between the results in terms of the rolling friction coefficient is remarkably good. This comparison confirms that friction coefficient predictions within a reasonable degree of accuracy can be obtained for low sliding speeds using the hybrid multiscale approach, except for low contact areas where poor contact pressure statistics are obtained.

From comparison of the results of Figures 5.16 and 5.17 to those of Figures 5.14 and 5.15, one can note that the microscales (the smallest wavelengths) ranging from 0.0625 to 0.25 mm have the largest contribution to the micro-rolling friction coefficient.

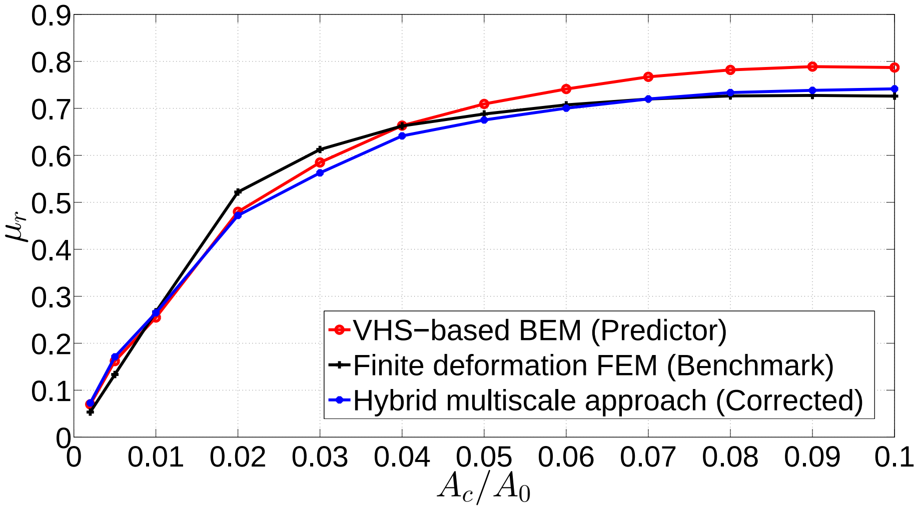

**Figure 5.16:** Comparison of friction coefficient as a function of the normalized contact area between the approaches for a surface approximation using superposition of 3 sinusoidal waves at a velocity of 10 [mm/s].

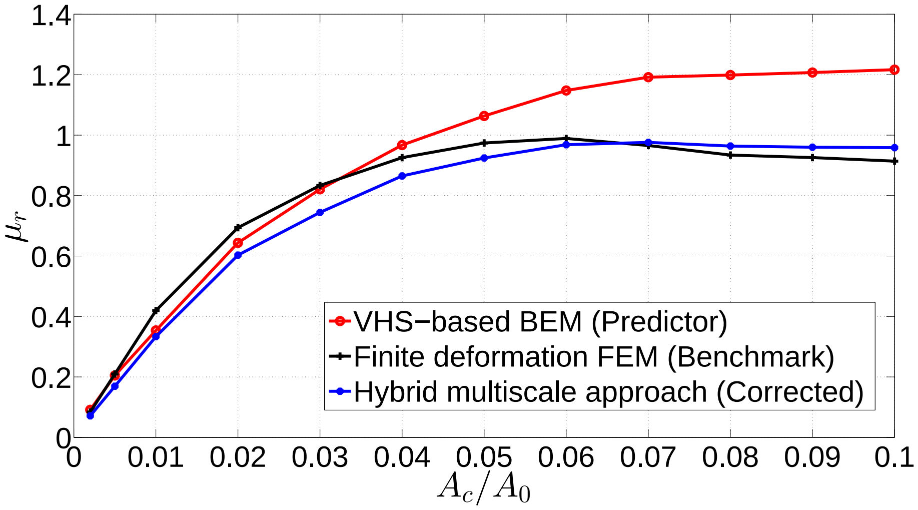

**Figure 5.17:** Comparison of friction coefficient as a function of the normalized contact area between the approaches for a surface approximation using superposition of 3 sinusoidal waves at a velocity of 50 [mm/s].

## 5.5 Conclusions

In summary, one can conclude that the hybrid multiscale approach can predict the micro-rolling friction coefficient within a plausible degree of accuracy for a relatively large contact area and low sliding velocities, while for small contact areas, the hybrid multiscale approach underestimates the friction coefficient. This is ascribed to the poor contact pressures statistics at small contact areas.

While the result is reproduced within a reasonable degree of accuracy for relatively large contact areas, the hybrid multiscale calculation needs only about 65% of the calculation time compared to the finite deformation FEM calculation including the computation times for all microscopic simulations.

Another conclusion is that the hybrid multiscale approach is not sensitive to the number of superimposed sine functions used to approximate the surface as the smallest length scale and the RMS height are kept the same and the upper cut-off covers the measured road track roughness.

Finally, the microscales ranging between few micrometers and few decimals of millimeters have the largest contribution to the hysteresis dissipation mechanism. Therefore, it is very important to include all surface details when calculating the rolling friction coefficient. This is consistent with other investigations about the role of small-scale wavelengths [86, 92, 118].

# Chapter 6

# Summary and outlook

## 6.1 Summary and conclusions

This thesis presents the derivation of a hybrid multiscale method for calculation of hysteretic rubber friction on rough surfaces. The motivation comes from the tire industry in order to develop future car tires with optimized characteristics, like reduced fuel consumption, minimized wear, and increased grip.

The major fraction of rubber friction at low velocities is generally attributed to hysteretic friction, where energy is dissipated inside the material due to repeated loading and unloading induced by surface irregularities. In general, we considered two families of approaches to investigate rubber friction, linear VHS-based models implemented with the BEM and finite deformation models implemented with the FEM. The linear model assumes a flat geometry of the rough surface (Reynolds roughness assumption). The aforementioned assumptions allow for the use of the VHS-theory in modeling the deformation response. Kinematically non-linear continuum mechanics formulations, implemented numerically through FEM, do not have these limitations and are able to provide predictions of rubber friction in a finite deformation framework, but at much higher computational cost.

Since many length scales contribute to rubber friction, it is necessary to investigate the entire geometry on all involved scales. Because of hardware restrictions and the computational cost, the FEM-implemented finite deformations model is not able to investigate all involved length scales at once. The problem is extremely expensive since the roughness includes a wide range of length scales, which requires extremely small mesh size in addition to the high nonlinearity resulting from contact conditions and large deformations, which influences the convergence rate.

On the other hand, the BEM-implemented VHS-based linear model has the ability to model all involved scales together with a reduced computational cost under the assumption of flat geometry of the rough surface. However, this assumption is an oversimplification of reality.

A road track was considered in this work. The asphalt roughness was measured using a profilometer. The roughness was approximated using a superposition of sine functions that differ in their wavelengthes and amplitudes, by fitting their sum of height difference correlation functions to the height difference correlation function of the measured roughness. The measured road track roughness has one scale (the micro scale) that violates the Reynolds assumption of flat geometry of the rough surface.

The first part of the thesis is concerned with investigation of the role of mean square slope roughness on the calculation of rubber friction. The Reynolds assumption accuracy is investigated in this part. The results of a linear viscoelastic model are compared with those obtained from non-linear finite element calculations. A sinusoidal rigid profile indenting a rubber block was considered here for simplicity, whereas the effects of mean square slope roughness were evaluated by varying the aspect ratio, loading conditions and sliding speed of the contact interface. It has been found that accurate friction predictions can be obtained through the linear viscoelastic model within Reynolds assumption for moderate values of root mean square slopes, whereas non-linear finite element computations should be adopted for large root mean square slopes. The contact area is much more sensitive to the geometrical and rheological nonlinearities than the rolling friction coefficient. The small deformation and the small root mean square slope assumptions in the linear viscoelastic model leads to quantitative deviations from the results obtained with a non-linear finite element description in terms of contact area fraction and local contact pressure distribution.

Starting from this conclusion, a new novel hybrid (finite deformation FEM/linear VHS-BEM) multiscale approach that combines the speed of linear viscoelastic model and the accuracy of the finite deformations model is established. The multiscale approach starts with precalculating the micro-rolling friction coefficient using VHS-based BEM as predictor, and then correlating the rolling friction coefficient. The behavior of the microscale is calculated as a function of the applied pressure for each dragging velocity using the VHS-based model on one hand, and the finite deformation model on the other hand. Then, the behavior of the microscale is transferred to the macroscales as a local repulsive law between the applied pressure and the average separation. The repulsive law controls the deformation behavior of the rubber according to the pressure. Depending on the local contact pressures resulting from the local repulsive law, the amount of correlation in the rolling friction coefficient is calculated as the difference between the rolling friction coefficients corresponding to the local contact pressures resulting from both approaches.

The presented hybrid multiscale approach has proven to be a suitable tool to study rolling-friction coefficient within a plausible degree of accuracy for relative large contact area and low sliding velocities. It allows a more faster calculation of friction coefficient than the finite deformation model. The sensitivity of the hybrid multiscale approach to the number of superimposed sine functions was studied and it has been found that the method is insensitive to the number of selected sine functions as the lower cut-off and the RMS height are kept the same and the upper cut-off covers the measured road track roughness. It has been found also in this study that the microscales ranging between few micrometers and few decimals of millimeters have the largest contribution to the hysteresis dissipation mechanism. Therefore, it is very important to include all surface details when calculating the rolling friction coefficient.

## 6.2 Future work

Possible advancements and extensions of the hybrid multiscale approach framework are as follows:

- Experimental validation of the approach. Suitable experiments should be designed in order to verify the approach. However, the prior history of the tire has a pronounced effect on rubber friction [115] and could produce local heating in the tread-block element. Furthermore, rubber is sensitive to outdoor environmental conditions like road environment, and humidity of the air [41, 115].

- Inclusion of adhesional effects. The adhesion can be estimated by introducing a macroscopic shear law coupled to the hysteretic part by evaluation of contact area [91]. It should be noted that hysteresis is dominated by length scales of a few micrometres and adhesion by even smaller length scales of a few hundred nanometres [115]. This includes developing computational algorithms which adaptively refine the nominal contact area in the region of true contact until a certain critical smallest length scale is reached.

- The approach was investigated for low dragging velocities and by assuming an isothermal contact. The work should be extended to high dragging velocities by inclusion of flash temperature effects. Williams-Landel-Ferry master curves for the characterisation of rubber material properties should be included [118].

- The work focuses on dry friction of rubber. Further studies should be devoted to investigate the wet friction. While hysteresis and adhesion are dominant for dry friction contacts, their influence decreases in wet friction. With increasing thickness of the water layer, the number of asperity contacts between tire and road surface becomes smaller and an increasing amount of normal contact force is transmitted via fluid forces and corresponding to that the tangential contact force is smaller, until in the extreme case the whole contact force is transmitted by the fluid film via pressure and viscous shearing [8, 50]. As a consequence, a complicated behavior is observed.

- Combination of all physical effects in the simulation setup, adding e.g. wear effects or water interaction, reveals many possibilities for future studies.

- Inclusion of advanced kinematics (e.g. rolling) into the multiscale approach, making the results comparable to tire test results.

- The transformation of the two-dimensional setup to a fully three-dimensional multiscale calculation remains a challenging topic for rough surfaces and could be studied in future.
- Future work should be devoted to the reduction of the computational cost, for example parallelization or using preconditioned iterative solution techniques to solve dense linear systems of equations arising from BEM.

# Appendix A

# Averaging tables

**Table A.1:** Averaged micro-rolling friction coefficient calculated using VHS-based BEM for a measured surface approximated by 8 superimposed sinusoidal waves and a velocity of 50 mm/s.

| | **Friction coefficient for realization #** | | | | | |
|---|---|---|---|---|---|---|
| **$A_c/A_0$** | **1** | **2** | **3** | **4** | **5** | **Avg** |
| 0.002 | 1.23991 | 1.15982 | 1.25875 | 1.51400 | 0.91912 | 1.21832 |
| 0.005 | 1.55822 | 1.40060 | 1.41840 | 1.58153 | 1.40306 | 1.47236 |
| 0.01 | 1.67754 | 1.64296 | 1.60462 | 1.69321 | 1.52456 | 1.62858 |
| 0.02 | 1.74327 | **1.70431** | 1.68306 | 1.75188 | 1.67896 | 1.71230 |
| 0.03 | 1.77189 | 1.68409 | 1.70648 | 1.77554 | 1.78090 | 1.74378 |
| 0.04 | **1.79497** | 1.68084 | **1.71533** | 1.77922 | **1.82777** | **1.75963** |
| 0.05 | 1.78435 | 1.66527 | 1.69227 | **1.78006** | 1.81703 | 1.74780 |
| 0.06 | 1.77845 | 1.64041 | 1.68056 | 1.77419 | 1.80547 | 1.73582 |
| 0.07 | 1.76270 | 1.62798 | 1.66897 | 1.75859 | 1.79248 | 1.72214 |
| 0.08 | 1.73871 | 1.62121 | 1.65566 | 1.74784 | 1.77662 | 1.70801 |
| 0.09 | 1.72241 | 1.62257 | 1.64324 | 1.74228 | 1.76280 | 1.69866 |
| 0.1 | 1.72000 | 1.62725 | 1.64301 | 1.73960 | 1.75355 | 1.69668 |

**Table A.2:** Averaged micro-rolling friction coefficient calculated using VHS-based BEM for a measured surface approximated by 9 superimposed sinusoidal waves and a velocity of 50 mm/s.

| | **Friction coefficient for realization #** | | | | | |
|---|---|---|---|---|---|---|
| **$A_c/A_0$** | **1** | **2** | **3** | **4** | **5** | **Avg** |
| 0.002 | 1.15216 | 1.45058 | 1.36765 | 1.55109 | 1.37009 | 1.37831 |
| 0.005 | 1.34747 | 1.75071 | 1.58615 | 1.71104 | 1.72445 | 1.62396 |
| 0.01 | 1.39418 | 1.79391 | 1.61860 | 1.74441 | 1.77182 | 1.66458 |
| 0.02 | 1.46175 | **1.79708** | 1.70812 | 1.75327 | 1.85127 | 1.71430 |
| 0.03 | 1.48423 | 1.78357 | 1.78374 | 1.74687 | **1.93188** | 1.74606 |
| 0.04 | 1.50127 | 1.73994 | 1.82328 | **1.74712** | 1.92969 | 1.74826 |
| 0.05 | 1.52379 | 1.72673 | 1.84692 | 1.74249 | 1.90908 | **1.74980** |
| 0.06 | 1.54088 | 1.71638 | **1.84966** | 1.72862 | 1.90135 | 1.74738 |
| 0.07 | 1.54699 | 1.70514 | 1.84492 | 1.71843 | 1.88814 | 1.74072 |
| 0.08 | **1.54976** | 1.69845 | 1.84592 | 1.70732 | 1.88228 | 1.73675 |
| 0.09 | 1.54903 | 1.69209 | 1.84273 | 1.69944 | 1.87015 | 1.73069 |
| 0.1 | 1.54246 | 1.68377 | 1.84322 | 1.69666 | 1.85874 | 1.72497 |

**Table A.3:** Averaged micro-rolling friction coefficient calculated using hybrid multiscale approach (FEM-BEM) for a measured surface approximated by 8 superimposed sinusoidal waves and a velocity of 10 mm/s.

| | **Friction coefficient for realization #** | | | | | |
|---|---|---|---|---|---|---|
| $A_c/A_0$ | **1** | **2** | **3** | **4** | **5** | **Avg** |
| 0.002 | 0.82675 | 0.81597 | 0.79436 | 0.74848 | 0.77798 | 0.79271 |
| 0.005 | 0.89704 | 0.92136 | 0.85445 | 1.00606 | **1.04625** | 0.94503 |
| 0.01 | 0.94578 | 1.01717 | 0.93559 | **1.04272** | 1.03432 | 0.99512 |
| 0.02 | 0.98274 | 1.03084 | 0.97855 | 1.04034 | 1.02406 | **1.01131** |
| 0.03 | **0.98597** | **1.03566** | **0.98004** | 1.02654 | 1.02804 | 1.01125 |
| 0.04 | 0.96799 | 1.02641 | 0.96369 | 1.00595 | 1.01817 | 0.99644 |
| 0.05 | 0.95783 | 1.01953 | 0.95483 | 0.99670 | 1.01122 | 0.98802 |
| 0.06 | 0.94436 | 1.00681 | 0.95569 | 0.98874 | 1.00150 | 0.97942 |
| 0.07 | 0.94040 | 1.00861 | 0.95351 | 0.97979 | 0.99958 | 0.97638 |
| 0.08 | 0.93643 | 1.00323 | 0.95362 | 0.97378 | 0.99506 | 0.97243 |
| 0.09 | 0.93408 | 0.99727 | 0.94842 | 0.97102 | 0.98789 | 0.96773 |
| 0.1 | 0.93397 | 0.99352 | 0.94533 | 0.97097 | 0.97890 | 0.96454 |

**Table A.4:** Averaged micro-rolling friction coefficient calculated using hybrid multiscale approach (FEM-BEM) for a measured surface approximated by 9 superimposed sinusoidal waves and a velocity of 10 mm/s.

| | **Friction coefficient for realization #** | | | | | |
|---|---|---|---|---|---|---|
| $A_c/A_0$ | **1** | **2** | **3** | **4** | **5** | **Avg** |
| 0.002 | 1.01395 | 0.92693 | 0.89243 | 0.99520 | 1.01760 | 0.96922 |
| 0.005 | **1.07900** | 0.90034 | **1.01954** | 1.01843 | **1.02646** | 1.00875 |
| 0.01 | 1.07195 | 0.92915 | 1.00214 | 1.06270 | 1.00704 | 1.01460 |
| 0.02 | 1.04918 | 0.97823 | 0.98841 | **1.06795** | 0.99364 | **1.01548** |
| 0.03 | 1.02442 | 0.98734 | 0.97018 | 1.06195 | 0.99276 | 1.00733 |
| 0.04 | 1.00502 | 0.99041 | 0.96946 | 1.04929 | 0.99232 | 1.00130 |
| 0.05 | 0.99984 | **0.99390** | 0.95858 | 1.03925 | 0.98869 | 0.99605 |
| 0.06 | 0.99567 | 0.99051 | 0.95368 | 1.03017 | 0.98781 | 0.99157 |
| 0.07 | 0.98565 | 0.98580 | 0.95136 | 1.02333 | 0.98575 | 0.98638 |
| 0.08 | 0.98135 | 0.98403 | 0.94809 | 1.01753 | 0.98201 | 0.98260 |
| 0.09 | 0.97968 | 0.98110 | 0.94625 | 1.01260 | 0.98035 | 0.98000 |
| 0.1 | 0.97400 | 0.97767 | 0.94355 | 1.00705 | 0.98105 | 0.97666 |

**Table A.5:** Averaged micro-rolling friction coefficient calculated using hybrid multiscale approach (FEM-BEM) for a measured surface approximated by 8 superimposed sinusoidal waves and a velocity of 50 mm/s.

| | **Friction coefficient for realization #** | | | | | |
|---|---|---|---|---|---|---|
| $A_c/A_0$ | **1** | **2** | **3** | **4** | **5** | **Avg** |
| 0.002 | 0.88526 | 0.85226 | 1.06465 | 0.95723 | 1.11207 | 0.97429 |
| 0.005 | 0.97544 | 0.96699 | 1.25043 | 1.19113 | 1.15635 | 1.10807 |
| 0.01 | 1.21319 | 1.15041 | 1.27986 | 1.28429 | 1.25661 | 1.23687 |
| 0.02 | 1.28740 | 1.25004 | **1.38255** | **1.37257** | 1.32842 | 1.32419 |
| 0.03 | 1.38482 | 1.37251 | 1.36295 | 1.35178 | 1.34218 | 1.36285 |
| 0.04 | 1.39875 | 1.40222 | 1.34838 | 1.34381 | 1.35553 | 1.36974 |
| 0.05 | **1.41746** | **1.40796** | 1.34179 | 1.34114 | 1.35569 | **1.37281** |
| 0.06 | 1.39826 | 1.39750 | 1.34110 | 1.33204 | 1.36174 | 1.36613 |
| 0.07 | 1.39451 | 1.39131 | 1.33533 | 1.32885 | **1.36503** | 1.36301 |
| 0.08 | 1.38425 | 1.38619 | 1.33210 | 1.31961 | 1.36444 | 1.35732 |
| 0.09 | 1.37387 | 1.38093 | 1.32629 | 1.30504 | 1.35810 | 1.34885 |
| 0.1 | 1.36970 | 1.37912 | 1.32150 | 1.30160 | 1.35466 | 1.34532 |

**Table A.6:** Averaged micro-rolling friction coefficient calculated using hybrid multiscale approach (FEM-BEM) for a measured surface approximated by 9 superimposed sinusoidal waves and a velocity of 50 mm/s.

| | **Friction coefficient for realization #** | | | | | |
|---|---|---|---|---|---|---|
| $A_c/A_0$ | **1** | **2** | **3** | **4** | **5** | **Avg** |
| 0.002 | 0.96921 | 1.48563 | 1.26914 | 1.11142 | 1.05342 | 1.17776 |
| 0.005 | 1.22256 | **1.54938** | 1.34629 | 1.23787 | 1.20495 | 1.31221 |
| 0.01 | 1.26601 | 1.52650 | 1.35244 | 1.31766 | 1.26402 | 1.34533 |
| 0.02 | 1.29320 | 1.51566 | **1.39767** | 1.36853 | 1.28799 | 1.37261 |
| 0.03 | **1.32162** | 1.50417 | 1.39555 | 1.41323 | 1.30366 | **1.38765** |
| 0.04 | 1.29918 | 1.49910 | 1.38097 | 1.42252 | **1.30489** | 1.38133 |
| 0.05 | 1.29518 | 1.49312 | 1.37617 | **1.43046** | 1.28126 | 1.37524 |
| 0.06 | 1.29159 | 1.48825 | 1.36869 | 1.42058 | 1.27104 | 1.36803 |
| 0.07 | 1.27903 | 1.48275 | 1.35475 | 1.40193 | 1.26401 | 1.35649 |
| 0.08 | 1.28115 | 1.47894 | 1.34060 | 1.38272 | 1.26134 | 1.34895 |
| 0.09 | 1.28030 | 1.47155 | 1.32462 | 1.37241 | 1.25488 | 1.34075 |
| 0.1 | 1.27982 | 1.46598 | 1.30862 | 1.37146 | 1.25223 | 1.33562 |

**Table A.7:** Averaged micro-rolling friction coefficient calculated using VHS-based BEM for an artificial surface composed of 3 superimposed sine functions and a velocity of 10 mm/s.

| | **Friction coefficient for realization #** | | | | | |
|---|---|---|---|---|---|---|
| $A_c/A_0$ | **1** | **2** | **3** | **4** | **5** | **Avg** |
| 0.002 | 0.08607 | 0.07008 | 0.10117 | 0.07425 | 0.01736 | 0.06979 |
| 0.005 | 0.19065 | 0.16052 | 0.20082 | 0.17425 | 0.08327 | 0.16190 |
| 0.01 | 0.26009 | 0.23540 | 0.24906 | 0.25708 | 0.27202 | 0.25473 |
| 0.02 | 0.49944 | 0.45773 | 0.51888 | 0.49199 | 0.43058 | 0.47972 |
| 0.03 | 0.60943 | 0.57367 | 0.59875 | 0.60839 | 0.53411 | 0.58487 |
| 0.04 | 0.71755 | 0.67627 | **0.66273** | 0.71589 | 0.54394 | 0.66328 |
| 0.05 | 0.80528 | 0.73457 | 0.66219 | 0.79710 | 0.54818 | 0.70946 |
| 0.06 | 0.85530 | 0.78580 | 0.65725 | 0.85568 | 0.55209 | 0.74122 |
| 0.07 | 0.89507 | 0.83402 | 0.63148 | 0.91245 | 0.56267 | 0.76714 |
| 0.08 | **0.91959** | 0.85874 | 0.63270 | 0.93550 | 0.56298 | 0.78190 |
| 0.09 | 0.91366 | 0.86859 | 0.63555 | **0.95870** | 0.56789 | **0.78888** |
| 0.1 | 0.89295 | **0.87532** | 0.64541 | 0.94793 | **0.57312** | 0.78695 |

**Table A.8:** Averaged micro-rolling friction coefficient calculated using finite deformation FEM for an artificial surface composed of 3 superimposed sine functions and a velocity of 10 mm/s.

| | **Friction coefficient for realization #** | | | | | |
|---|---|---|---|---|---|---|
| $A_c/A_0$ | **1** | **2** | **3** | **4** | **5** | **Avg** |
| 0.002 | 0.05570 | 0.05868 | 0.04883 | 0.05575 | 0.04783 | 0.05336 |
| 0.005 | 0.13924 | 0.14669 | 0.12207 | 0.13938 | 0.11957 | 0.13339 |
| 0.01 | 0.27849 | 0.29338 | 0.24414 | 0.27877 | 0.23913 | 0.26678 |
| 0.02 | 0.54182 | 0.54954 | 0.48827 | 0.55117 | 0.47827 | 0.52182 |
| 0.03 | 0.63097 | 0.63523 | 0.58851 | 0.68277 | 0.52468 | 0.61243 |
| 0.04 | 0.70179 | 0.69740 | **0.64500** | 0.73474 | 0.53450 | 0.66268 |
| 0.05 | 0.74753 | 0.74107 | 0.63352 | 0.77394 | 0.54432 | 0.68808 |
| 0.06 | 0.77543 | 0.78237 | 0.62403 | 0.80115 | 0.55414 | 0.70742 |
| 0.07 | 0.79715 | 0.80042 | 0.61612 | 0.82022 | 0.56505 | 0.71979 |
| 0.08 | **0.80302** | 0.81235 | 0.61348 | 0.82750 | 0.57621 | 0.72651 |
| 0.09 | 0.78802 | **0.81297** | 0.61520 | **0.83415** | 0.58753 | **0.72757** |
| 0.1 | 0.77388 | 0.81268 | 0.61847 | 0.82636 | **0.59928** | 0.72613 |

**Table A.9:** Averaged micro-rolling friction coefficient calculated using hybrid multiscale approach for an artificial surface composed of 3 superimposed sine functions and a velocity of 10 mm/s.

| | **Friction coefficient for realization #** | | | | | |
|---|---|---|---|---|---|---|
| $A_c/A_0$ | **1** | **2** | **3** | **4** | **5** | **Avg** |
| 0.002 | 0.10253 | 0.06639 | 0.06628 | 0.09093 | 0.03767 | 0.07276 |
| 0.005 | 0.23179 | 0.15129 | 0.14832 | 0.21595 | 0.10747 | 0.17096 |
| 0.01 | 0.30223 | 0.22942 | 0.24578 | 0.29601 | 0.25010 | 0.26471 |
| 0.02 | 0.47186 | 0.46537 | 0.49848 | 0.46203 | 0.46237 | 0.47202 |
| 0.03 | 0.56699 | 0.54927 | 0.59193 | 0.57758 | 0.52783 | 0.56272 |
| 0.04 | 0.67706 | 0.65812 | **0.65091** | 0.68321 | 0.53765 | 0.64139 |
| 0.05 | 0.74777 | 0.68721 | 0.64307 | 0.74751 | 0.55044 | 0.67520 |
| 0.06 | 0.79081 | 0.72457 | 0.63510 | 0.79802 | 0.55346 | 0.70039 |
| 0.07 | 0.83645 | 0.75328 | 0.62124 | 0.82932 | 0.55943 | 0.71994 |
| 0.08 | **0.83798** | 0.78536 | 0.61989 | 0.85319 | 0.57180 | 0.73364 |
| 0.09 | 0.82584 | 0.78849 | 0.62198 | **0.87412** | 0.58099 | 0.73828 |
| 0.1 | 0.81393 | **0.80514** | 0.62745 | 0.87069 | **0.59056** | **0.74155** |

**Table A.10:** Averaged micro-rolling friction coefficient calculated using VHS-based BEM for an artificial surface composed of 3 superimposed sine functions and a velocity of 50 mm/s.

| | **Friction coefficient for realization #** | | | | | |
|---|---|---|---|---|---|---|
| $A_c/A_0$ | **1** | **2** | **3** | **4** | **5** | **Avg** |
| 0.002 | 0.09579 | 0.11132 | 0.06984 | 0.07345 | 0.10569 | 0.09122 |
| 0.005 | 0.18448 | 0.25659 | 0.18365 | 0.16764 | 0.23165 | 0.20480 |
| 0.01 | 0.20413 | 0.46071 | 0.41028 | 0.28147 | 0.41223 | 0.35376 |
| 0.02 | 0.34653 | 0.83074 | 0.78757 | 0.41845 | 0.83530 | 0.64372 |
| 0.03 | 0.47213 | 1.06350 | 1.04277 | 0.47707 | 1.04803 | 0.82070 |
| 0.04 | 0.68889 | 1.18116 | 1.21759 | 0.47772 | 1.26967 | 0.96701 |
| 0.05 | 0.75271 | 1.34051 | **1.26727** | 0.54652 | 1.40973 | 1.06335 |
| 0.06 | 0.88521 | 1.42782 | 1.23981 | 0.61390 | **1.57197** | 1.14775 |
| 0.07 | 0.97443 | **1.52494** | 1.22814 | 0.70299 | 1.52772 | 1.19164 |
| 0.08 | 1.00766 | 1.48891 | 1.21208 | 0.76467 | 1.52090 | 1.19885 |
| 0.09 | 1.03277 | 1.45036 | 1.18521 | 0.85910 | 1.50760 | 1.20701 |
| 0.1 | **1.04458** | 1.44400 | 1.16931 | **0.93605** | 1.48972 | **1.21673** |

**Table A.11:** Averaged micro-rolling friction coefficient calculated using finite deformation FEM for an artificial surface composed of 3 superimposed sine functions and a velocity of 50 mm/s.

| | **Friction coefficient for realization #** | | | | | |
|---|---|---|---|---|---|---|
| $\boldsymbol{A_c/A_0}$ | **1** | **2** | **3** | **4** | **5** | **Avg** |
| 0.002 | 0.06983 | 0.10437 | 0.10298 | 0.06374 | 0.07843 | 0.08387 |
| 0.005 | 0.17458 | 0.26092 | 0.25745 | 0.15935 | 0.19607 | 0.20967 |
| 0.01 | 0.34917 | 0.52183 | 0.51489 | 0.31870 | 0.39214 | 0.41935 |
| 0.02 | 0.52447 | 0.82068 | 0.82818 | 0.63057 | 0.66497 | 0.69377 |
| 0.03 | 0.66037 | 0.98235 | 1.00561 | 0.75265 | 0.76667 | 0.83353 |
| 0.04 | 0.74516 | 1.06472 | 1.10476 | 0.86378 | 0.84928 | 0.92554 |
| 0.05 | 0.82218 | 1.12418 | **1.16022** | 0.86980 | 0.89376 | 0.97403 |
| 0.06 | 0.88333 | **1.12795** | 1.12846 | 0.88354 | **0.92116** | **0.98889** |
| 0.07 | 0.92328 | 1.05212 | 1.02969 | 0.90270 | 0.92008 | 0.96557 |
| 0.08 | 0.94607 | 0.97726 | 0.92162 | 0.91501 | 0.91012 | 0.93402 |
| 0.09 | **0.95848** | 0.95067 | 0.90119 | 0.92256 | 0.89573 | 0.92573 |
| 0.1 | 0.92966 | 0.94628 | 0.88910 | **0.92301** | 0.88134 | 0.91388 |

**Table A.12:** Averaged micro-rolling friction coefficient calculated using hybrid multiscale approach for an artificial surface composed of 3 superimposed sine functions and a velocity of 50 mm/s.

| | **Friction coefficient for realization #** | | | | | |
|---|---|---|---|---|---|---|
| $\boldsymbol{A_c/A_0}$ | **1** | **2** | **3** | **4** | **5** | **Avg** |
| 0.002 | 0.07848 | 0.09242 | 0.05927 | 0.06698 | 0.05894 | 0.07122 |
| 0.005 | 0.17788 | 0.22190 | 0.15270 | 0.16211 | 0.13106 | 0.16913 |
| 0.01 | 0.30082 | 0.41633 | 0.36301 | 0.30629 | 0.27906 | 0.33310 |
| 0.02 | 0.46516 | 0.65292 | 0.70744 | 0.55986 | 0.62979 | 0.60304 |
| 0.03 | 0.59762 | 0.80499 | 0.90261 | 0.66079 | 0.75588 | 0.74438 |
| 0.04 | 0.72640 | 0.91556 | 1.06024 | 0.73509 | 0.88776 | 0.86501 |
| 0.05 | 0.79902 | 0.98660 | **1.08323** | 0.76204 | 0.99027 | 0.92423 |
| 0.06 | 0.88396 | **1.03595** | 1.06074 | 0.79366 | **1.06706** | 0.96827 |
| 0.07 | 0.94033 | 1.03123 | 1.00541 | 0.83613 | 1.06711 | **0.97604** |
| 0.08 | 0.96660 | 1.01196 | 0.93913 | 0.86489 | 1.03645 | 0.96381 |
| 0.09 | **0.98325** | 1.01193 | 0.89687 | 0.90141 | 1.00598 | 0.95989 |
| 0.1 | 0.96796 | 1.00712 | 0.89115 | **0.92736** | 0.99910 | 0.95854 |

# Bibliography

[1] Abbot, E. J., Firestone, F. A. (1933). Specifying surface quality. Mech. Eng, 55(9), 569-572.

[2] Abdelrahman, A. A., El-Shafei, A. G., Mahmoud, F. F. (2015). Analysis of steady-state rolling contact problems in nonlinear viscoelastic materials. Journal of Tribology, 137(3), 031402.
http://doi.org/10.1115/1.4029938

[3] Altenbach H. (2012). Kontinuumsmechanik: Einführung in die materialunabhängigen und materialabhä ngigen Gleichungen. Springer, Berlin, 2nd edition. (In German)

[4] Bandeira, A. A., Wriggers, P., de Mattos Pimenta, P. (2004). Numerical derivation of contact mechanics interface laws using a finite element approach for large 3D deformation. International Journal for numerical methods in Engineering, 59(2), 173-195.
http://doi.org/10.1002/nme.867

[5] Bathe, K. J., Chaudhary, A. (1985). A solution method for planar and axisymmetric contact problems. International Journal for Numerical Methods in Engineering, 21(1), 65-88.
http://doi.org/10.1002/nme.1620210107

[6] Belytschko, T., Liu, W. K., Moran, B., Elkhodary, K. (2013). Nonlinear finite elements for continua and structures. John wiley and sons.

[7] Benson, D. J., Hallquist, J. O. (1990). A single surface contact algorithm for the post-buckling analysis of shell structures. Computer Methods in Applied Mechanics and Engineering, 78(2), 141-163.
http://doi.org/10.1016/0045-7825(90)90098-7

[8] Besdo, D., Heimann, B., Klüppel, M., Kröger, M., Wriggers, P., Nackenhorst, U. (2010). Elastomere friction: theory, experiment and simulation (Vol. 51). Springer Science and Business Media.

[9] Bonet, J., Wood, R. D. (1997). Nonlinear continuum mechanics for finite element analysis. Cambridge university press.

[10] Carbone, G., Decuzzi, P. (2004). Elastic beam over an adhesive wavy foundation. Journal of applied physics, 95(8), 4476-4482.
https://doi.org/10.1063/1.1650560

[11] Carbone, G., Lorenz, B., Persson, B. N. J., Wohlers, A. (2009). Contact mechanics and rubber friction for randomly rough surfaces with anisotropic statistical properties. The European Physical Journal E, 29(3), 275-284.
http://doi.org/10.1140/epje/i2009-10484-8

[12] Carbone, G., Mangialardi, L. (2004). Adhesion and friction of an elastic half-space in contact with a slightly wavy rigid surface. Journal of the Mechanics and Physics of Solids, 52(6), 1267-1287.
http://doi.org/10.1016/j.jmps.2003.12.001

[13] Carbone, G., Putignano, C. (2013). A novel methodology to predict sliding and rolling friction of viscoelastic materials: theory and experiments. Journal of the Mechanics and Physics of Solids, 61(8), 1822-1834.
http://doi.org/10.1016/j.jmps.2013.03.005

[14] Carbone, G., Putignano, C. (2014). Rough viscoelastic sliding contact: theory and experiments. Physical Review E, 89(3), 032408.
http://doi.org/ 10.1103/PhysRevE.89.032408

[15] Chadwick, P. (2012). Continuum mechanics: concise theory and problems. Courier Corporation.

[16] Ciarlet, P. G. (1988). Mathematical Elasticity, I: Three-dimensional elasticity. Vol. 20 of Stud. Math. Appl. Elsevier.

[17] De Lorenzis, L., Wriggers, P. (2013). Computational homogenization of rubber friction on rough rigid surfaces. Computational Materials Science, 77, 264-280.
http://doi.org/10.1016/j.commatsci.2013.04.049.

[18] De Lorenzis, L., Wriggers, P., Weissenfels, C. (2017). Computational Contact Mechanics with the Finite Element Method. Encyclopedia of Computational Mechanics Second Edition, 1-45.
http://doi.org/10.1002/9781119176817.ecm2033

[19] El-Abbasi, N., Bathe, K. J. (2001). Stability and patch test performance of contact discretizations and a new solution algorithm. Computers and Structures, 79(16), 1473-1486.
http://doi.org/10.1016/S0045-7949(01)00048-7

[20] Falk, K., Lang, R., Kaliske, M. (2016). Multiscale Simulation to Determine Rubber Friction on Asphalt Surfaces. Tire Science And Technology, 44(4), 226-247.
http://doi.org/10.2346/tire.16.440401

[21] Fortunato, G., Ciaravola, V., Furno, A., Scaraggi, M., Lorenz, B., Persson, B. N. (2017). Dependency of rubber friction on normal force or load: theory and experiment. Tire Science and Technology, 45(1), 25-54.
http://arxiv.org/abs/1512.01359

[22] Gäbel, G.S. (2009). Beobachtung und Modellierung lokaler Phänomene im Reifen/Fahrbahn-Kontakt. Ph.D. thesis, Leibniz Universität Hannover. (In German).

[23] Gent, A. N. (2012). Engineering with rubber: how to design rubber components. Carl Hanser Verlag GmbH Co KG.

[24] Greenwood, J. A., Johnson, K. L., Choi, S. H., Chaudhury, M. K. (2008). Investigation of adhesion hysteresis between rubber and glass using a pendulum. Journal of Physics D: Applied Physics, 42(3), 035301.
http://doi.org/10.1088/0022-3727/42/3/035301

[25] Greenwood, J. A., Williamson, J. P. (1966). Contact of nominally flat surfaces. Proc. R. Soc. Lond. A, 295(1442), 300-319.
http://doi.org/10.1098/rspa.1966.0242

[26] Grosch, K. A. (1963). The relation between the friction and visco-elastic properties of rubber. Proc. R. Soc. Lond. A, 274(1356), 21-39.
http://doi.org/10.1098/rspa.1963.0112

[27] Grosch, K. A. (1963). Visco-elastic properties and the friction of solids: Relation between the friction and visco-elastic properties of rubber. Nature, 197, 858-859.
http://doi.org/10.1038/197858a0

[28] Hallquist, J. O. (1979). An implicit, finite-deformation, finite-element code for analyzing the static and dynamic response of two-dimensional solids (No. UCRL-52678). California Univ., Livermore (USA). Lawrence Livermore Lab.

[29] Hallquist, J. O., Goudreau, G. L., Benson, D. J. (1985). Sliding interfaces with contact-impact in large-scale Lagrangian computations. Computer methods in applied mechanics and engineering, 51(1-3), 107-137.
http://doi.org/10.1016/0045-7825(85)90030-1

[30] Haupt, P. (2013). Continuum mechanics and theory of materials. Springer Science and Business Media.

[31] Hertz, H. (1881), Ueber die Berührung fester elastischer Körper. Journal für die reine und angewandte Mathematik 92, 156. (In German).

[32] Hofstetter, K., Eberhardsteiner, J., Mang, H. A. (2006). Efficient treatment of rubber friction problems in industrial applications. Structural Engineering and Mechanics, 22(5), 517-539.
http://doi.org/10.12989/sem.2006.22.5.517

[33] Hofstetter, K., Grohs, C., Eberhardsteiner, J., Mang, H. A. (2006). Sliding behaviour of simplified tire tread patterns investigated by means of FEM. Computers and structures, 84(17-18), 1151-1163.
http://doi.org/10.1016/j.compstruc.2006.01.010

[34] Holzapfel G.A. (2000). Nonlinear solid mechanics: A continuum approach for engineering. Wiley, 1st edition.

[35] Hughes, T. J. R., Taylor, R. L., Kanoknukulchai, W. (1977). A finite element method for large displacement contact and impact problems. Formulations and Computational Algorithms in FE Analysis, 468-495.

[36] Hughes, T. J., Taylor, R. L., Sackman, J. L., Curnier, A., Kanoknukulchai, W. (1976). A finite element method for a class of contact-impact problems. Computer methods in applied mechanics and engineering, 8(3), 249-276.
http://doi.org/10.1016/0045-7825(76)90018-9

[37] Ignatyev, P. A., Ripka, S., Mueller, N., Torbruegge, S., Wies, B. (2015). Tire ABS-Braking Prediction with Lab Tests and Friction Simulations. Tire Science And Technology, 43(4), 260-275.
http://doi.org/10.2346/tire.15.430401

[38] Johnson, K. L. (1987). Contact mechanics. Cambridge university press.

[39] Kaliske, M., Rothert, H. (1997). Formulation and implementation of three-dimensional viscoelasticity at small and finite strains. Computational Mechanics, 19(3), 228-239.
http://doi.org/10.1007/s004660050171

[40] Klüppel, M., Heinrich, G. (2000). Rubber friction on self-affine road tracks. Rubber chemistry and technology, 73(4), 578-606.
http://doi.org/10.5254/1.3547607.

[41] Kogbara, R. B., Masad, E. A., Kassem, E., Scarpas, A. (2018). Skid Resistance Characteristics of Asphalt Pavements in Hot Climates. Journal of Transportation Engineering, Part B: Pavements, 144(2), 04018015.
http://doi.org/10.1061/JPEODX.0000046

[42] Lahayne, O., Eberhardsteiner, J. (2007). Investigation of the temperature behaviour of sliding rubber materials. WIT Transactions on Engineering Sciences, 55.
http://doi.org/10.2495/SECM070151

[43] Laursen, T. A. (2013). Computational contact and impact mechanics: fundamentals of modeling interfacial phenomena in nonlinear finite element analysis. Springer Science and Business Media.

[44] Le Gal, A., Klüppel, M. (2007). Investigation and modelling of rubber stationary friction on rough surfaces. Journal of Physics: Condensed Matter, 20(1), 015007. http://doi.org/10.1088/0953-8984/20/01/015007.

[45] Lee, D. H., Cho, N. G. (2012). Assessment of surface profile data acquired by a stylus profilometer. Measurement science and technology, 23(10), 105601. http://doi.org/10.1088/0957-0233/23/10/105601

[46] Lindner M. (2005). Experimentelle und theoretische Untersuchungen zur Gummireibung and Profilklötzen und Dichtungen. Ph.D. thesis, Leibniz Universität Hannover . (In German).

[47] Linke, T., Wangenheim, M., Lind, H., Ripka, S. (2014). Experimental friction and temperature investigation on aircraft tires. Tire Science and Technology, 42(3), 116-144.
http://doi.org/10.2346/tire.14.420301.

[48] Lion, A. (1997). A physically based method to represent the thermo-mechanical behaviour of elastomers. Acta Mechanica, 123(1-4), 1-25.
http://doi.org/10.1007/BF01178397

[49] Lion, A. (1997). On the large deformation behaviour of reinforced rubber at different temperatures. Journal of the Mechanics and Physics of Solids, 45(11-12), 1805-1834.
http://doi.org/10.1016/S0022-5096(97)00028-8.

[50] Liu, F., Sutcliffe, M. P. F., Graham, W. R. (2008). Modeling of tread block contact mechanics using linear viscoelastic theory. Tire science and technology, 36(3), 211-226.
http://doi.org/10.2346/1.2965832

[51] Löhnert, S. (1999). An adaptive stepsize control for the integration of evolution equations in viscoelasticity. Diplomarbeit, Teschnische Universität Darmstadt.

[52] Lorenz B., Oh Y.R., Nam S.K., Jeon S.H. (2015). Rubber friction on road surfaces: Experiment and theory for low sliding speeds. The Journal of Chemical Physics, 142 (19): 194 701.
http://doi.org/10.1063/1.4919221

[53] Lorenz, B., Pyckhout-Hintzen, W., Persson, B. N. J. (2014). Master curve of viscoelastic solid: Using causality to determine the optimal shifting procedure, and to test the accuracy of measured data. Polymer, 55(2), 565-571.
http://doi.org/10.1016/j.polymer.2013.12.033

[54] Lu, T. (2010). The influence of pavement stiffness on vehicle fuel consumption (Doctoral dissertation, University of Nottingham).

[55] Lubliner, J. (1985). A model of rubber viscoelasticity. Mechanics Research Communications, 12(2), 93-99.
http://doi.org/10.1016/0093-6413(85)90075-8

[56] Mandelbrot, B. B. (1982). The fractal geometry of nature (Vol. 2). New York: WH freeman.

[57] Menga, N., Putignano, C., Carbone, G., Demelio, G. P. (2014). The sliding contact of a rigid wavy surface with a viscoelastic half-space. Proc. R. Soc. A, 470(2169), 20140392.
http://doi.org/10.1098/rspa.2014.0392

[58] Mullins, L. (1948). Effect of stretching on the properties of rubber. Rubber Chemistry and Technology, 21(2), 281-300.
http://doi.org/10.5254/1.3546914

[59] Nitsche, R., Wriggers, P., Hauret, P. (2011). A multiscale projection method for contact on rough surfaces. (Ph.D. thesis). Inst. für Kontinuumsmechanik. , Leibniz Universität Hannover.

[60] Ogden, R. W. (1997). Non-linear elastic deformations. Courier Corporation.

[61] Palasantzas, G. (2003). Influence of self-affine surface roughness on the friction coefficient for rubbers. Journal of applied physics, 94(9), 5652-5655.
https://doi.org/10.1063/1.1616985

[62] Palasantzas, G., De Hosson, J. T. M. (2003). Self-affine roughness effects on the contact area between elastic bodies. Journal of applied physics, 93(2), 898-902.
http://doi.org/10.1063/1.1528300

[63] Papadopoulos, P., Taylor, R. L. (1992). A mixed formulation for the finite element solution of contact problems. Computer Methods in Applied Mechanics and Engineering, 94(3), 373-389.
http://doi.org/10.1016/0045-7825(92)90061-N

[64] Papadopoulos, P., Taylor, R. L. (1993). A simple algorithm for three-dimensional finite element analysis of contact problems. Computers and Structures, 46(6), 1107-1118.
http://doi.org/10.1016/0045-7949(93)90096-V

[65] Pastewka, L., Prodanov, N., Lorenz, B., Müser, M. H., Robbins, M. O., Persson, B. N. (2013). Finite-size scaling in the interfacial stiffness of rough elastic contacts. Physical Review E, 87(6), 062809.
http://doi.org/10.1103/PhysRevE.87.062809

[66] Payne, A. R. (1962). The dynamic properties of carbon black-loaded natural rubber vulcanizates. Part I. Journal of applied polymer science, 6(19), 57-63.
http://doi.org/10.1002/app.1962.070061906

[67] Payne, A. R. (1962). The dynamic properties of carbon black loaded natural rubber vulcanizates. Part II. Journal of Applied Polymer Science, 6(21), 368-372.
http://doi.org/10.1002/app.1962.070062115

[68] Persson, B. N. (2001). Theory of rubber friction and contact mechanics. The Journal of Chemical Physics, 115(8), 3840-3861.
http://doi.org/10.1063/1.1388626

[69] Persson, B. N. (2006). Contact mechanics for randomly rough surfaces. Surface science reports, 61(4), 201-227.
http://doi.org/10.1016/j.surfrep.2006.04.001

[70] Persson, B. N. (2006). Rubber friction: role of the flash temperature. Journal of Physics: Condensed Matter, 18(32), 7789.
http://doi.org/10.1088/0953-8984/18/32/025

[71] Persson, B. N. J. (2009). Theory of powdery rubber wear. Journal of Physics: Condensed Matter, 21(48), 485001.
http://doi.org/10.1088/0953-8984/21/48/485001

[72] Persson, B. N. J. (2010). Rolling friction for hard cylinder and sphere on viscoelastic solid. The European Physical Journal E, 33(4), 327-333.
http://doi.org/10.1140/epje/i2010-10678-y

[73] Persson, B. N. J. (2010). Rubber friction and tire dynamics. Journal of Physics: Condensed Matter, 23(1), 015003.
http://doi.org/10.1088/0953-8984/23/1/015003.

[74] Persson, B. N. J. (2014). On the fractal dimension of rough surfaces. Tribology Letters, 54(1), 99-106.
http://doi.org/10.1007/s11249-014-0313-4

[75] Persson, B. N. J. (2014). Role of frictional heating in rubber friction. Tribology Letters, 56(1), 77-92.
http://doi.org/10.1007/s11249-014-0386-0

[76] Persson, B. N. J., Albohr, O., Tartaglino, U., Volokitin, A. I., Tosatti, E. (2004). On the nature of surface roughness with application to contact mechanics, sealing, rubber friction and adhesion. Journal of Physics: Condensed Matter, 17(1), R1.
http://doi.org/10.1088/0953-8984/17/1/R01.

[77] Persson, B. N. J., Scaraggi, M., Volokitin, A. I., Chaudhury, M. K. (2013). Contact electrification and the work of adhesion. EPL (Europhysics Letters), 103(3), 36003.
http://doi.org/10.1209/0295-5075/103/36003

[78] Persson, B. N., Tosatti, E. (2000). Qualitative theory of rubber friction and wear. The Journal of Chemical Physics, 112(4), 2021-2029.
http://doi.org/10.1063/1.480762.

[79] Poon, C. Y., Bhushan, B. (1995). Comparison of surface roughness measurements by stylus profiler, AFM and non-contact optical profiler. Wear, 190(1), 76-88. http://doi.org/10.1016/0043-1648(95)06697-7

[80] Raous, M., Cangémi, L., Cocu, M. (1999). A consistent model coupling adhesion, friction, and unilateral contact. Computer methods in applied mechanics and engineering, 177(3-4), 383-399. http://doi.org/10.1016/S0045-7825(98)00389-2

[81] Reese, S., Govindjee, S. (1997). Theoretical and numerical aspects in the thermo-viscoelastic material behaviour of rubber-like polymers. Mechanics of Time-Dependent Materials, 1(4), 357-396. http://doi.org/10.1023/A:1009795431265

[82] Reese, S., Govindjee, S. (1998). A theory of finite viscoelasticity and numerical aspects. International journal of solids and structures, 35(26-27), 3455-3482. http://doi.org/10.1016/S0020-7683(97)00217-5

[83] Ripka, S., Gäbel, G., Wangenheim, M. (2009). Dynamics of a Siped Tire Tread Block-Experiment and Simulation. Tire Science and Technology, 37(4), 323-339. http://doi.org/10.2346/1.3148296

[84] Röthemeyer, F., Sommer, F. (2013). Kautschuktechnologie: Werkstoffe-Verarbeitung-Produkte. Carl Hanser Verlag GmbH Co KG. (In German)

[85] Scaraggi, M. (2015). Partial surface texturing: A mechanism for local flow reconditioning in lubricated contacts. Proceedings of the Institution of Mechanical Engineers, Part J: Journal of Engineering Tribology, 229(4), 493-504. http://doi.org/10.1177/1350650114539935

[86] Scaraggi, M., Comingio, D. (2017). Rough contact mechanics for viscoelastic graded materials: The role of small-scale wavelengths on rubber friction. International Journal of Solids and Structures, 125, 276-296. http://doi.org/10.1016/j.ijsolstr.2017.06.008

[87] Scaraggi, M., Comingio, D., Al-Qudsi, A., De Lorenzis, L. (2016). The influence of geometrical and rheological non-linearity on the calculation of rubber friction. Tribology International, 101, 402-413. http://doi.org/10.1016/j.triboint.2016.04.027

[88] Scaraggi, M., Persson, B. N. (2014). Rolling friction: comparison of analytical theory with exact numerical results. Tribology Letters, 55(1), 15-21. http://doi.org/10.1007/s11249-014-0327-y

[89] Scaraggi, M., Persson, B. N. (2015). General contact mechanics theory for randomly rough surfaces with application to rubber friction. The Journal of chemical physics, 143(22), 224111. http://doi.org/10.1063/1.4936558

[90] Scaraggi, M., Persson, B. N. J. (2014). Theory of viscoelastic lubrication. Tribology International, 72, 118-130.
http://doi.org/10.1016/j.triboint.2013.12.011

[91] Scaraggi, M., Persson, B. N. J. (2015). Friction and universal contact area law for randomly rough viscoelastic contacts. Journal of Physics: Condensed Matter, 27(10), 105102.
http://doi.org/10.1088/0953-8984/27/10/105102

[92] Scaraggi, M., Persson, B. N. J. (2016). The effect of finite roughness size and bulk thickness on the prediction of rubber friction and contact mechanics. Proceedings of the Institution of Mechanical Engineers, Part C: Journal of Mechanical Engineering Science, 230(9), 1398-1409.
http://doi.org/10.1177/0954406216642261

[93] Schallamach, A. (1952). The load dependence of rubber friction. Proceedings of the Physical Society. Section B, 65(9), 657.
http://doi.org/10.1088/0370-1301/65/9/301

[94] Schallamach, A. (1953). The velocity and temperature dependence of rubber friction. Proceedings of the Physical Society. Section B, 66(5), 386.
http://doi.org/10.1088/0370-1301/66/5/306

[95] Schramm, E. J. (2003). Reibung von Elastomeren auf rauen Oberflächen und Beschreibung von Nassbremseigenschaften von PKW-Reifen (Doctoral dissertation). University of Regensburg (2002). (In German)

[96] She, H., Malotky, D., Chaudhury, M. K. (1998). Estimation of adhesion hysteresis at polymer/oxide interfaces using rolling contact mechanics. Langmuir, 14(11), 3090-3100.
http://doi.org/10.1021/la971061m

[97] Simo, J. C., Wriggers, P., Taylor, R. L. (1985). A perturbed Lagrangian formulation for the finite element solution of contact problems. Computer methods in applied mechanics and engineering, 50(2), 163-180.
http://doi.org/10.1016/0045-7825(85)90088-X

[98] SIMULIA, Abaqus Theory Guide (6.14), Dassault Systémes SIMULIA Corp., Providence Rhode Island USA, 2014.

[99] SIMULIA, Abaqus Analysis User's Guide (6.14), Dassault Systémes SIMULIA Corp., Providence Rhode Island USA, 2014.

[100] Srirangam, S. K. (2015). Numerical Simulation of Tire-Pavement Interaction. (Ph.D. thesis), Delft University of Technology.

[101] Stupkiewicz, S. (2007). Micromechanics of contact and interphase layers (Vol. 30). Springer Science and Business Media.

[102] Taylor, R. L., Papadopoulos, P. (1991). On a patch test for contact problems in two dimensions. Computational methods in nonlinear mechanics, 690, 702.

[103] Temizer, I., Wriggers, P. (2008). A multiscale contact homogenization technique for the modeling of third bodies in the contact interface. Computer Methods in Applied Mechanics and Engineering, 198(3-4), 377-396.
http://doi.org/10.1016/j.cma.2008.08.008

[104] Temizer, I., Wriggers, P. (2010). Inelastic analysis of granular interfaces via computational contact homogenization. International Journal for Numerical Methods in Engineering, 84(8), 883-915.
http://doi.org/10.1002/nme.2921

[105] Temizer, I., Wriggers, P. (2010). Thermal contact conductance characterization via computational contact homogenization: a finite deformation theory framework. International Journal for Numerical Methods in Engineering, 83(1), 27-58.
http://doi.org/10.1002/nme.2822

[106] Temizer, I. (2011). Thermomechanical contact homogenization with random rough surfaces and microscopic contact resistance. Tribology International, 44(2), 114-124.
http://doi.org/10.1016/j.triboint.2010.09.011

[107] Temizer, I. (2014). Multiscale thermomechanical contact: Computational homogenization with isogeometric analysis. International Journal for Numerical Methods in Engineering, 97(8), 582-607.
http://doi.org/10.1002/nme.4604

[108] Temizer, I. (2016). Sliding friction across the scales: Thermomechanical interactions and dissipation partitioning. Journal of the Mechanics and Physics of Solids, 89, 126-148.
http://doi.org/10.1016/j.jmps.2016.01.012

[109] Timoshenko, S. P., Goodier, J. N., Abramson, H. N. (1970). Theory of elasticity. Journal of Applied Mechanics, 37, 888.

[110] Truesdell, C., Noll, W. (2013). The Non-Linear Field Theories of Mechanics/Die Nicht-Linearen Feldtheorien der Mechanik (Vol. 2). Springer Science and Business Media.

[111] Tworzydlo, W. W., Cecot, W., Oden, J. T., Yew, C. H. (1998). Computational micro-and macroscopic models of contact and friction: formulation, approach and applications. Wear, 220(2), 113-140.
http://doi.org/10.1016/S0043-1648(98)00194-X

[112] Wagner, P., Wriggers, P., Klapproth, C., Prange, C. (2014). Multiscale FEM approach for rubber friction on rough surfaces. 14th European Mechanics of Materials Conference EMMC-14, Gothenburg, Sweden.

[113] Wagner, P., Wriggers, P., Klapproth, C., Prange, C., Wies, B. (2015). Multiscale FEM approach for hysteresis friction of rubber on rough surfaces. Computer Methods in Applied Mechanics and Engineering, 296, 150-168.
http://doi.org/10.1016/j.cma.2015.08.003

[114] Wagner, P., Wriggers, P., Veltmaat, L., Clasen, H., Prange, C., Wies, B. (2017). Numerical multiscale modelling and experimental validation of low speed rubber friction on rough road surfaces including hysteretic and adhesive effects. Tribology International, 111, 243-253.
http://doi.org/10.1016/j.triboint.2017.03.015

[115] Wallaschek, J., Wies, B. (2013). Tyre tread-block friction: modelling, simulation and experimental validation. Vehicle System Dynamics, 51(7), 1017-1026.
http://doi.org/10.1080/00423114.2013.803580

[116] Willner, K. (2013). Kontinuums-und kontaktmechanik: Synthetische und analytische darstellung. Springer-Verlag. (In German).

[117] Wriggers, P. (2008). Nonlinear finite element methods. Springer Science and Business Media.

[118] Wriggers, P., Reinelt, J. (2009). Multi-scale approach for frictional contact of elastomers on rough rigid surfaces. Computer Methods in Applied Mechanics and Engineering, 198(21-26), 1996-2008.
http://doi.org/10.1016/j.cma.2008.12.021

[119] Wriggers, P., Simo, J. C. (1985). A note on tangent stiffness for fully nonlinear contact problems. Communications in Applied Numerical Methods, 1(5), 199-203.
http://doi.org/10.1002/cnm.1630010503

[120] Wriggers, P., Van, T. V., Stein, E. (1990). Finite element formulation of large deformation impact-contact problems with friction. Computers and Structures, 37(3), 319-331.
http://doi.org/10.1016/0045-7949(90)90324-U

[121] Wriggers, P., Zavarise, G. (2004). Computational contact mechanics. Encyclopedia of computational mechanics.

[122] Yastrebov, V. A., Anciaux, G., Molinari, J. F. (2014). The contact of elastic regular wavy surfaces revisited. Tribology Letters, 56(1), 171-183.
https://doi.org/10.1007/s11249-014-0395-z

[123] Zavarise, G., De Lorenzis, L. (2009). A modified node-to-segment algorithm passing the contact patch test. International journal for numerical methods in engineering, 79(4), 379-416.
http://doi.org/10.1002/nme.2559

[124] Zavarise, G., De Lorenzis, L. (2009). The node-to-segment algorithm for 2D frictionless contact: classical formulation and special cases. Computer Methods in Applied Mechanics and Engineering, 198(41-44), 3428-3451.
http://doi.org/10.1016/j.cma.2009.06.022

[125] Zavarise, G., Wriggers, P. (1998). A segment-to-segment contact strategy. Mathematical and Computer Modelling, 28(4-8), 497-515.
http://doi.org/10.1016/S0895-7177(98)00138-1

[126] Zeng, H. (2013). Polymer adhesion, friction, and lubrication. John Wiley and Sons.

[127] Zienkiewicz, O. C., Taylor, R. L. (2005). The finite element method for solid and structural mechanics. Elsevier.

# Curriculum vitae

Name: Ahmad Al-Qudsi

Date of Birth: 29. June 1986

Place of Birth: Kuwait

Nationality: Jordanian

Marital status: married, one child

## Education

| | |
|---|---|
| 10.2003 - 09.2008 | B. Sc. Aeronautical Engineering (5 years degree), University of Aleppo, Syria. |
| 10.2009 - 05.2012 | M. Sc. Computational Sciences in Engineering, Braunschweig University of Technology, Germany. |

## Occupation

| | |
|---|---|
| 06.2012 - 05.2013 | Research assistant at the Institute of Metal Forming, Leibniz University Hanover. |
| 06.2013 - 08.2017 | Research assistant at the Institute of Applied Mechanics, Braunschweig University of Technology. |
| since 11.2017 | Research assistant at the Institute of Pavement Engineering, Braunschweig University of Technology. |

## Awards

| | |
|---|---|
| 2011 | Award for academic excellence in WS 2010/11 and SS 2011, Braunschweig University of Technology. |